Measurement of the ^{1}H(^{7}Be,^{8}B)γ cross section

by
Ryan P. Fitzgerald

A dissertation submitted to the faculty of the University of North Carolina at Chapel Hill in partial fulfillment of the requirements for the degree of Doctor of Philosophy in the Department of Physics & Astronomy.

Chapel Hill
2005

Approved:

A. E. Champagne, Advisor

J. C. Blackmon, Reader

C. Iliadis, Reader

ABSTRACT

RYAN P. FITZGERALD: Measurement of the ^{1}H(^{7}Be,^{8} B)γ cross section
(Under the Direction of A. E. Champagne)

The fusion of protons with radioactive nuclei plays an important role in a wide variety of astrophysical scenarios ranging from high-temperature environments like novae and X-ray bursts to the production of neutrinos in the sun. For example, the ^{8}B neutrino flux measured in neutrino detectors on earth is directly proportional to the cross section for the fusion of protons with radioactive ^{7}Be.

An experimental program has been established to study proton-fusion experiments in inverse kinematics at the Holifield Radioactive Ion Beam Facility (HRIBF) at Oak Ridge National Laboratory (ORNL) using a windowless gas target and the Daresbury Recoil Separator (DRS). The performance of the target and separator have been well characterized using a variety of experiments with stable beams including ^{12}C, ^{19}F, and ^{24}Mg. For instance, the areal density of hydrogen in the target was determined to 3% accuracy. This well-characterized system was used to measure accurate stopping powers for many elements in hydrogen gas for the first time.

The first measurement of a proton-fusion cross section with a radioactive ion beam at ORNL, the fusion of protons with ^{7}Be, was performed using the hydrogen gas target and the DRS. The ^{7}Be was produced at the Triangle Universities Nuclear Laboratory (TUNL) and chemically isolated at ORNL. An average ^{7}Be beam current of 2.5 ppA bombarded the windowless gas target for a period of 3 days. Recoiling B-8 nuclei were efficiently collected using the DRS and were clearly identified in a gas-filled ion detector. The cross section at a center-of-mass energy of 1.502 MeV was determined to be 1.12 μb with 24% uncertainty. The zero-energy S-factor was determined to be 26.8 eV-b with 25% uncertainty. The technique has been clearly demonstrated, and a precise measurement of the fusion cross section will be possible with the development of a somewhat more intense ^{7}Be radioactive ion beam.

ACKNOWLEDGMENTS

Since January 2001, I have been part of an extraordinary collaboration whose work I present here. Yet even before I regenerated my first cryo-pump, this project was already being actively developed. My thesis advisor Art Champagne successfully pitched the proposal for this measurement to the Oak Ridge PAC in 1999. Meanwhile, Jeff Blackmon, Michael Smith and Dan Bardayan were rebuilding the separator (with advisement from Arthur James and help from a lot of other folks) and Uwe Greife was designing the gas target. Then, during the first few years of ^{7}Be development at TUNL, Carrie Rowland, Bob Runkle and Eric Harley helped Art and I through some tough times with our friend DENIS. Throughout the sometimes perilous ^{7}Be production runs at TUNL, Chris Westerfeldt, Paul Carter, Richard O'quinn and John Dunham nourished the tandem and source, keeping us going. During the final two fortnight-production runs, Peter Bertone, Chris Fox, Joe Newton and Tim Daniels made essential contributions and Jeff Blackmon, Dale Visser and Jake Livesay were kind enough to drive across the mountain to lend a hand.

Meanwhile back in Oak Ridge, a crack team gathered to assemble, align, chastise, forgive and then nurture the gas target. Jake Livesay finally turned the choose-your-own-adventure target stand into a reality and Jeff Thomas subtly dedicated himself to contributing to every gas-target project by nesting in the DRS counting room. Likewise, Ray Kozub was always willing to make a trip (twice as long as it was far) to contribute to these here-reported experiments. Other folks like Dale Visser, Zhanwen Ma, Micah Johnson, Kate Jones, Latife Sahin, Steve Pain, Caroline Nesaraja and Andy Chae arrived in Oak Ridge and immediately started to contribute to experiments. Carlo Domizioli spent a summer working on the gas target characterization, and I like Brian

Moazen. Dan Stracener joined Jeff Blackmon during the arduous ^{7}Be chemistry sessions. Furthermore, Dan's tireless work with the ion source has earned him a second sentence. Mike Dinehart's expertise was critical during the final measurement.

During my time in graduate school, I have personally enjoyed working with all the people whose work I acknowledge above as well as my other fellow UNC students; João, Andy, Geoff, Mitzi, Brian, Doug, Rich and Eliza. I am particularly thankful to Art Champagne for letting me make mistakes and for not letting me make mistakes, as needed. Also, I am especially grateful to Jeff Blackmon for his dedication, concern, humor, and trust. I also thank Christian Iliadis for valuable conversations and advice.

This period in my life has been enriched by many friendships in Chapel Hill and Oak Ridge, especially those with my apartment-mates, my Saturday-dinner-and-beyond friends (Obrigado), and my comrades in Oak Ridge.

I thank my parents and the rest of my family for their support during these past six years. I am very lucky to be able to count on them. I thank my wife Carrie for her encouragement and companionship; without which I would likely be living in a van, by the river.

Ultimately, I am grateful to the taxpayers of the Town of Tonawanda, New York State, North Carolina and the United States of America. Thank you for financially supporting my education.

Ryan Fitzgerald

Chapel Hill 2005

CONTENTS

LIST OF FIGURES

LIST OF TABLES

Chapter 1

Motivation and background

1.1 Introduction to solar astrophysics

Radiation from the sun sustains life on earth. This energy feeds plants and animals and warms the ground and air, setting all these things in motion (e.g. potholes). The quest to understand our sun has led to advances in nuclear physics, a theory of the origin of the elements, and the discovery of the properties of neutrinos.

A typical main-sequence star, the sun is a $2.0{\cdot}10^{30}$-kg ball of plasma measuring $1.4{\cdot}10^{7}$ km across that shines at $L_{\odot} = 3.8{\cdot}10^{26}$ Watts ($2.4{\cdot}10^{39}$ MeV/s) [Roh94]. It is composed of 74% hydrogen, 26% helium (by mass) with traces of heavier elements [Bad05]. The energy production and elemental synthesis proceed by nuclear reactions in the the solar core. The gravitational pull of the solar matter is balanced by outward pressure provided by these nuclear reactions, and the result is a state of hydrostatic equilibrium within the sun. Most of the energy released by the sun comes from the burning of four protons to form ^{4}He in the "proton-proton" reaction chain,

$$4p \;\rightarrow\; {}^4\mathrm{He} \;+\; 2e^{+} \;+\; 2\nu_e. \tag{1.1}$$

The energy released (Q) by this conversion of H to He is calculated using Einstein's formula,

$$E \;=\; mc^2, \tag{1.2}$$

and the definition of Q,

$$Q \;=\; T_{final} - T_{initial} \;=\; M_{initial}c^2 - M_{final}c^2, \tag{1.3}$$

Where E is total energy, T is kinetic energy, M is mass and c is the speed of light. The kinetic energy released is equal to an opposite change in the potential energy of the system (i.e. binding energy). These formulae can be used to determine the release of potential energy from any source; mechanical, gravitational, chemical, nuclear etc., but are most naturally applied to nuclear reactions since the potential energy change can be relatively large. For example, in the reaction shown in Eqn. 1.1, the potential energy released (Q) is from the change in nuclear binding energy between the initial and final states, and is equivalent to 3% of the mass of a proton. Currently, the mass of the proton and He^4 are both known to better than 2 parts in 10^9 [Aud03], so using the masses to determine the energy release is quite accurate. For comparison to a typical chemical reaction, less than 1 part in 10^{12} of the atomic mass is lost when H_2 dissociates to 2H. This above mentioned reasoning was first used by Eddington in 1920 to show (using Aston's mass measurements) that proton-proton fusion indeed could power the sun. To quote Eddington [Edd20]:

> If 5 per cent of a star's mass consists initially of hydrogen atoms, which are gradually being combined to form more complex elements, the total heat liberated will more than suffice for our demands, and we need look no further for the source of a star's energy.

The 26.7 MeV of kinetic energy released by the proton-proton chain is shared by the massive particles and photons produced during the reactions. Other reaction chains, such as the CNO chain, occur in the center of the sun where temperatures are highest, but contribute little to energy production. For higher mass stars however, they can dominate energy production [Bet39]. The p-p chain proceeds through a variety of steps and branches shown in Table 1.1.

Chain	Reaction	Branching (%)	Neutrino Energy (MeV)
	$p + p \rightarrow {}^2\mathrm{H} + e^+ + \nu_e$	99.6	0.0 to 0.4
	or		
	$p + e^- + p \rightarrow {}^2\mathrm{H} + \nu_e$	0.44	1.4
	then		
	${}^2H + p \rightarrow {}^3\mathrm{He} + \gamma$	100	–
I	${}^3He + {}^3He \rightarrow {}^4\mathrm{He} + 2\,{}^1H$	85	–
	or		
	${}^3\mathrm{He} + {}^4\mathrm{He} \rightarrow {}^7\mathrm{Be} + \gamma$	15	–
	then		
	${}^7\mathrm{Be} + e^- \rightarrow {}^7\mathrm{Li} + \nu_e$	99.86	0.86,0.38
II	${}^7Li + p \rightarrow {}^4\mathrm{He} + {}^4\mathrm{He}$	100	–
	or		
	${}^7\mathrm{Be} + p \rightarrow {}^8\mathrm{B} + \gamma$	0.02	–
III	${}^8\mathrm{B} \rightarrow {}^8\mathrm{Be} + e^+ + \nu_e$	100	0 to 15

Table 1.1: Reactions of the three branches of the p-p chain. The probabilities at each branch point are shown, and the energies of the neutrinos there produced. Adapted from [Bah01].

1.2 Solar neutrinos

One important constituent of the nuclear reactions in Table. 1.1 is the electron neutrino (ν_e). Since 2 neutrinos are emitted upon each completion of the p-p chain (Table 1.1) the solar neutrino flux is,

$$\Phi_{\nu_e} = \frac{2L_\odot}{Q_{p-p}} \;=\; 1.8 \cdot 10^{38}/s. \tag{1.4}$$

But at ≈ 0.1 MeV/ν_e this makes up only 2% of the solar luminosity. Although neutrinos do not carry away as much energy as do photons from the sun, they are the key to understanding the workings of the solar core. Unlike photons, which only travel a few centimeters in the sun before interacting, neutrinos made in the core of the sun pass through both the sun and the earth with a interaction probability of only 1 in 10^{30}. Thus, the number and energy spectra of neutrinos detected on earth are indicative of the conditions in which the neutrinos were formed. The same weak nature that provides a glimpse inside the sun, hinders neutrino detection on earth. Therefore, all solar-neutrino detectors contain very large volumes of active detector material.

Table 1.1 and Fig.1.1 show that most numerous neutrinos from the proton-proton chain come from the $p + p \;\rightarrow\; {}^2H + e^+ + \nu_e$ reaction. The cross section for that reaction is well known theoretically, but the neutrino energies are all below 0.4 MeV. Since neutrino interaction cross sections rise steeply with energy, and since many detectors have thresholds above this point (eg. 0.8 MeV for $\nu + {}^{37}$Cl), most solar neutrino experiments have focused on a tiny fraction (0.001%) of the solar neutrino flux; ^{8}B neutrinos above $\approx$ 1-5 MeV.

Solar neutrino observations began in 1968 with Davis' measurement of ^{8}B neutrinos in a chlorine detector (for which he shared the Nobel prize in 2002). Further solar neutrino flux measurements were made over the next 30 years, and the consistent finding of these experiments was that the measured flux of ^{8}B neutrinos (Φ) was consistently lower than the predictions of the Standard Solar Model (SSM) [Bah01] (most recently updates in [Bah04]). This was, during much of that period, known as the "solar neutrino problem". Since then, the discovery of mixing among the neutrino flavors, and the constraints on

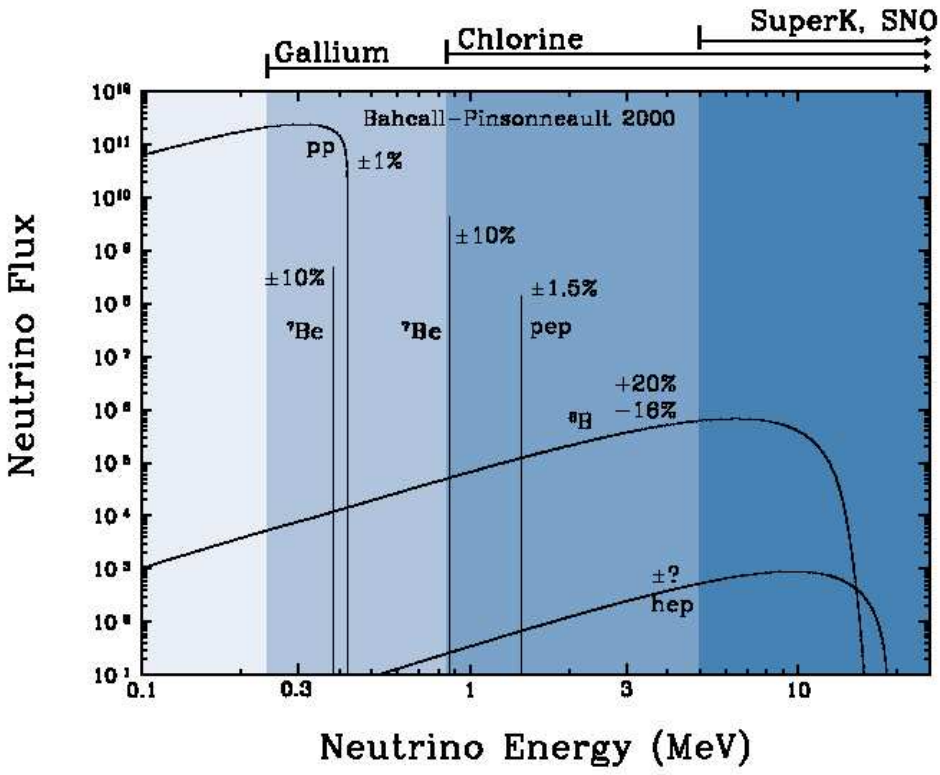

Figure 1.1: Solar neutrino spectra for all sources [Bah00].

those mixing parameters by new neutrino-detection experiments have begun to unite the data and models of neutrino parameters.

There are 3 neutrino flavors that interact via the weak force; ν_e, ν_τ and ν_μ. These three are composed of at least 3 eigenstates of the free Hamiltonian (mass eigenstates) ν_1, ν_2 and ν_3. It is also possible that sterile neutrinos exist in one or more non-interacting flavor. This fact will be ignored for now. The 3 interacting neutrino flavors ν_l are then related to the mass eigenstates ν_i by,

$$\nu_l \;=\; U_{li}\nu_i, \tag{1.5}$$

where U is a 3x3 unitary mixing matrix. For the likely case that 2 flavor solar neutrino mixing is favored, Eqn. 1.5 can be written as

$$\begin{pmatrix} \nu_e \\ \nu_a \end{pmatrix} \;=\; \begin{pmatrix} sin(\theta_{12}) & cos(\theta_{12}) \\ cos(\theta_{12}) & -sin(\theta_{12}) \end{pmatrix} \begin{pmatrix} \nu_1 \\ \nu_2 \end{pmatrix}, \tag{1.6}$$

where ν_a refers to either ν_τ or ν_μ. If $m_1 \neq m_2$ then, from the time-dependent Schrödinger equation of the free Hamiltonian (H_o),

$$H_o\Psi \;=\; i\hbar\frac{\delta}{\delta t}\Psi, \tag{1.7}$$

the phase difference between states 1 and 2 will monotonically increase. From Eqns. 1.6 and 1.7, it follows that the probability for a ν_e created in the sun to oscillate to ν_a after traveling a distance (L) at the speed of light (c) in vacuum is,

$$\left|cos\theta_{12}\ sin\theta_{12}\ (e^{-iE_1L/(\hbar c)} - e^{-iE_2L/(\hbar c)})\right|^2 \;\approx\; sin^2 2\theta_{12}\ sin^2\left(\frac{\delta m^2_{12}\ L}{4\,\hbar c E_o}\right), \tag{1.8}$$

where E_o is the eigen-energy of H_o and $\delta m^2_{12} \;=\; m^2_2 - m^2_1$. Thus, if 2-flavor mixing is occurring in the solar neutrino sector, the quantities that parameterize the neutrino mixing are θ_{12} and δm^2_{12}. In the presence of matter, electron neutrinos will experience preferential elastic scattering, which thus modifies the interaction Hamiltonian. This and other matter effects, such as resonance enhancement of mixing as neutrinos pass through varying density of matter are also considered in neutrino mixing calculations (see [Hax00] for an overview of neutrino physics). In these cases, Eqn. 1.8 must be modified to solve the full Hamiltonian and the probability for transmutation is still be expressed in terms of θ_{12} and δm^2_{12}.

1.2.1 Solar neutrino experiments

As mentioned above, the first solar neutrino measurement [Dav68] was based on interactions of neutrinos with ^{37}Cl by the reaction, $^{37}\mathrm{Cl}(\nu_e, e^-)^{37}\mathrm{Ar}$ in a tank containing 615 tons of cleaning fluid (CCl_4). The Ar atoms were flushed from the liquid and captured an electron (producing ^{37}Cl). Since ^{37}Ar had a 35 day half life, it could be isolated and counted. That set of experiments was the first to show a factor of 3 paucity in ν_e flux compared to the SSM of 1968 (which excluded mixing at that time). Other radiochemical experiments, SAGE and GALLEX, using ^{71}Ga were sensitive to pp neutrinos, confirmed this effect, and discovered evidence of its energy dependence. The following generation of

experiments at Kamiokande, and SuperK(amiokande), and eventually, SNO used water Cerenkov detectors to measure real time ν_e events from high-energy ^{8}B electron neutrinos (Fig. 1.1). The directionality of the Cerenkov light, allowed them to distinguish those rare events from background. Furthermore, the scattering reaction employed by SNO and SuperK, $\nu_x + e^- \rightarrow \nu_x + e^-$, was sensitive (in varying degrees) to all neutrino flavors, which was not the case for the Cl and Ga detectors.

One of the latest detectors, SNO, used heavy water (D_2O) and measured 2 important quantities separately. The first was the ν_e flux, using the charged-current (CC) channel, $\nu_e + d \rightarrow p + p + e^-$, from which the ν_e energy spectrum was measured. The second was the neutral-current (NC) channel, $\nu_x + d \rightarrow n + p + \nu_x$, from which the total active-neutrino flux was determined. In the absence of sterile neutrinos, the NC and CC data, combined with the solar and terrestrial densities, uniquely determined the mixing parameters δm^2 and θ_{12}. Furthermore, the NC measurement was a direct experimental determination of the total ^{8}B -neutrino flux (again, ignoring sterile neutrinos). The NC flux measured by SNO was [Ahm04],

$$\Phi_{NC} = (5.21 \pm 0.27(stat) \pm 0.38(sys)) \cdot 10^6 cm^{-2} s^{-1}. \tag{1.9}$$

Combining the reported NC and CC fluxes gave,

$$\frac{\Phi_{CC}}{\Phi_{NC}} = 0.306 \pm 0.026(stat) \pm 0.024(sys), \tag{1.10}$$

which is interpreted to support the idea that ν_e oscillates to ν_τ or ν_μ. All of the solar neutrino data have been combined to determine the neutrino oscillation parameters, within a 3σ range [Mal03],

$$\begin{aligned} 0.23 &\geq sin^2\theta_{12} \leq 0.39 \\ 5.4 \cdot 10^{-5} eV^2 &\geq \delta m^2_{12} \leq 9.4 \cdot 10^{-5}\, eV^2. \end{aligned} \tag{1.11}$$

1.2.2 Standard solar model

The standard solar model (SSM) is a model of the sun, using nuclear reaction cross sections and various solar observations (abundances, luminosity, heliosismology etc.).

year	^{3}He +^{3} He	^{3}He +^{4} He	p +^{7} Be	a	b	c	$L\odot$	Φ_ν
2001	2	8	+14/-7	8	5	4	3	$^{+20}_{-16}$
2004	2	8	4	20	5	4	3	23

Table 1.2: Uncertainties (%) in ^{8}B neutrino flux (Φ_ν) in the SSM as adopted by [Bah01] and [Bah04], where a is composition, b is opacity and c is diffusion.

As such, it makes quantitative predictions of the the solar neutrino flux and energy spectrum. Because it is always changing, we will refer to BP04 [Bah04] as the SSM, and also make comments on the older version BP01 [Bah01], and the somewhat controversial BP04+ [Bah04] versions of the model. The most recent version of the model was just released [Bah05b], and is similar to [Bah04]. Since the new paper does not enumerate all the sources of error, it is not used in the present error analysis. In light of the SNO NC data, the SSM is no longer used to determine the most accurate total ^{8}B ν flux from the sun, except in relation to sterile neutrinos. However, the model does provide the necessary density profile for mixing calculations and places limits on sterile neutrino mixing. Also, the SSM can now be compared directly to experiments (NC data). The major sources of uncertainty adopted in the SSM [Bah04] and BP01 [Bah01] are listed in Table 1.2.

The evolution of the uncertainties in Table 1.2 reflects recent nuclear physics experiments and solar observations. The reduction in the adopted ^{7}Be$(p,\gamma)^8$B cross-section uncertainty is due to the fact that the SSM uses only the most recent ^{7}Be$(p,\gamma)^8$B measurement in their analysis. That new ^{7}Be$(p,\gamma)^8$B experiment ([Jun03]) reports a higher and more precise value than the other recent measurements, as discussed in Sec. 1.4. The increase in uncertainty of the solar composition is described by the SSM authors as arising from a series of new metalicity studies over the last few years. In fact, the revised values for the solar composition in the SSM do not even include the most recent of the newest studies. Those new data imply a shallower convective zone than would agree with helioseismological data. Inclusion of the new composition data leads to the BP04+ model, which is not recommended by the SSM authors. (See [Bah05b] and [Bah05a] for

discussions of the composition literature.)

The experimental ^{8}B neutrino observations and standard solar model then lead to,

$$\frac{\Phi_{exp}}{\Phi_{SSM}} = 0.88 \pm 0.04 \pm 0.23,$$

where the first error is experimental and the second theoretical [Bah04]. This agreement implies that the sterile neutrino is ruled out at 1σ. From an experimental nuclear physics standpoint, the model's uncertainty can be improved most dramatically by measuring the ^{3}He(^{4}He, γ)^{7}Be and the ^{7}Be(p, γ)^{8}B low energy cross sections.

1.3 Reaction formalism

The notational formalism for studying these reactions in the laboratory is presented here, following the review of [Rol88] and references therein. In a laboratory experiment, the observable quantity for a beam of energy (E) and beam current (I) interacting with a target of areal density (n) is the number of reaction products (Y) produced. This yield is often expressed in terms of the reaction cross section (σ) and the stopping power of the beam in the target,

$$\epsilon \;=\; \frac{dE}{dn}. \tag{1.12}$$

The reaction yield per incident beam particle is then written,

$$Y(E) \;=\; \int_{Eo-\Delta}^{Eo} \frac{\sigma(E)}{\epsilon(E)}\, dE, \tag{1.13}$$

where the beam loses Δ energy while passing through the target. And then for a thin target, over which $\sigma(E)$ and $\epsilon(E)$ are constant,

$$Y(E) \;=\; \sigma\, n. \tag{1.14}$$

The cross section, $\sigma(E_{cm})$, for ^{7}Be$(p,\gamma)^{8}$B is shown in Fig. 1.2. Here, the energy in the center of mass frame,

$$E_{cm} \;=\; E\, \frac{M_{target}}{M_{target} + M_{beam}}, \tag{1.15}$$

is reported.

The behavior of $\sigma(E)$ for solar (p,γ) reactions at low energies is dominated by the (s-wave) Coulomb penetrability,

$$P(E) \;=\; e^{-2\pi\eta}, \tag{1.16}$$

where the Sommerfeld parameter (η) for the interaction of 2 particles is given by,

$$\eta(E) \;=\; \frac{Z_1 Z_2\, e^2}{\hbar v}. \tag{1.17}$$

The other significant energy dependence is from the quantum mechanical area scale ($\sigma_{QM} \propto E^{-1}$). Thus, the cross section is typically written as the product of these extra-nuclear effects and the astrophysical S-factor ($S(E)$), which contains the nuclear components of the cross section,

$$\sigma(E) \;=\; \frac{1}{E}\, e^{-2\pi\eta}\, S(E). \tag{1.18}$$

The probability for a reaction to occur in the sun is determined by the cross section and the Maxwell-Boltzmann velocity distribution of the ions involved. The energy corresponding to the peak in the Maxwell-Boltzmann velocity distribution is $\mathrm{E} = \mathrm{kT}$, which in the solar core corresponds to $\mathrm{E} = 1.3\,\mathrm{keV}$. However, multiplying the Maxwell-Boltzmann probability by the reaction probability ($\propto \sigma(E)$) leads to the total probability distribution. This distribution peaks at $E_{cm} = 18\,\mathrm{keV}$ for $^{7}\mathrm{Be}(p,\gamma)^{8}\mathrm{B}$ in the solar core. At these low energies, the reaction is dominated by the direct capture process, leading to a smooth S(E), as well as isolated resonances, as shown in Fig. 1.2. Therefore, it is common to express $S(E)$ in an expansion around $E = 0$ for the direct capture contribution to the cross section,

$$S(E) \;\approx\; S(0) \;+\; S'(0)E \;+\; \frac{1}{2}S''(0)\,... \tag{1.19}$$

Resonant contributions to $\sigma(E)$ are parameterized by the Breit-Wigner formula,

$$\sigma_{BW}(E) \;=\; \frac{\lambda^2}{4\pi}\frac{2J_R+1}{(2J_1+1)(2J_2+1)}\,\frac{\Gamma_i(E)\,\Gamma_x(E)}{(E_R-E)^2+\frac{\Gamma(E)^2}{4}}, \tag{1.20}$$

Where J is spin, Γ is width, λ is the de Broglie wavelength, and i, x, and R refer to the initial state, final state and resonance. The integral of the Breit-Wigner cross section, for a narrow resonance, over all energies is often expressed in terms of the resonance strength ($\omega\gamma$) as,

$$\int_{-\infty}^{\infty} \sigma_{BW}(E)\, dE \;=\; \lambda_R^2 \frac{\omega\gamma}{2}. \tag{1.21}$$

Then the peak resonant cross section can then be expressed,

$$\sigma_R \;=\; \frac{\lambda_R^2}{\pi\Gamma_R}\,\omega\gamma. \tag{1.22}$$

If a beam of energy E_o is incident on a target and loses energy Δ while passing through the target, the reaction yield per beam particle due to a resonance at E_r is then determined by integrating Eqn. 1.20 over a finite energy range,

$$Y(Eo) = \frac{\lambda^2}{2\pi}\omega\gamma\frac{M+m}{M}\frac{1}{\epsilon}\left[tan^{-1}(\frac{E_o - E_r}{\Gamma/2}) - tan^{-1}(\frac{Eo - Er - \Delta}{\Gamma/2})\right], \tag{1.23}$$

where the stopping power value is in the laboratory frame. Here, the width (Γ) is taken to be energy-independent. This is a good approximation when the energy loss of the beam in the target is much less than the width of the resonance, and the target is considered to be "thin". On the other hand, for a "thick target", in which the energy loss of the beam is much greater than the width of the resonance, the yield approaches,

$$Y(\infty) = \frac{\lambda^2}{2}\omega\gamma\frac{M+m}{M}\frac{1}{\epsilon}. \tag{1.24}$$

For a broad-resonance incident upon a thick target, the energy dependence of the widths and stopping power must be considered in the integral 1.23.

Interference effects can occur among the various direct capture and resonance contributions (of the same ℓ-value) to the S-factor. For the low energy ^{7}Be$(p,\gamma)^8$B reaction (Fig. 1.2), the s and d-wave cross sections add coherently to the resonant (p-wave) contribution. Complete references to the ^{7}Be + p structure are given in Sec. 1.4.1.

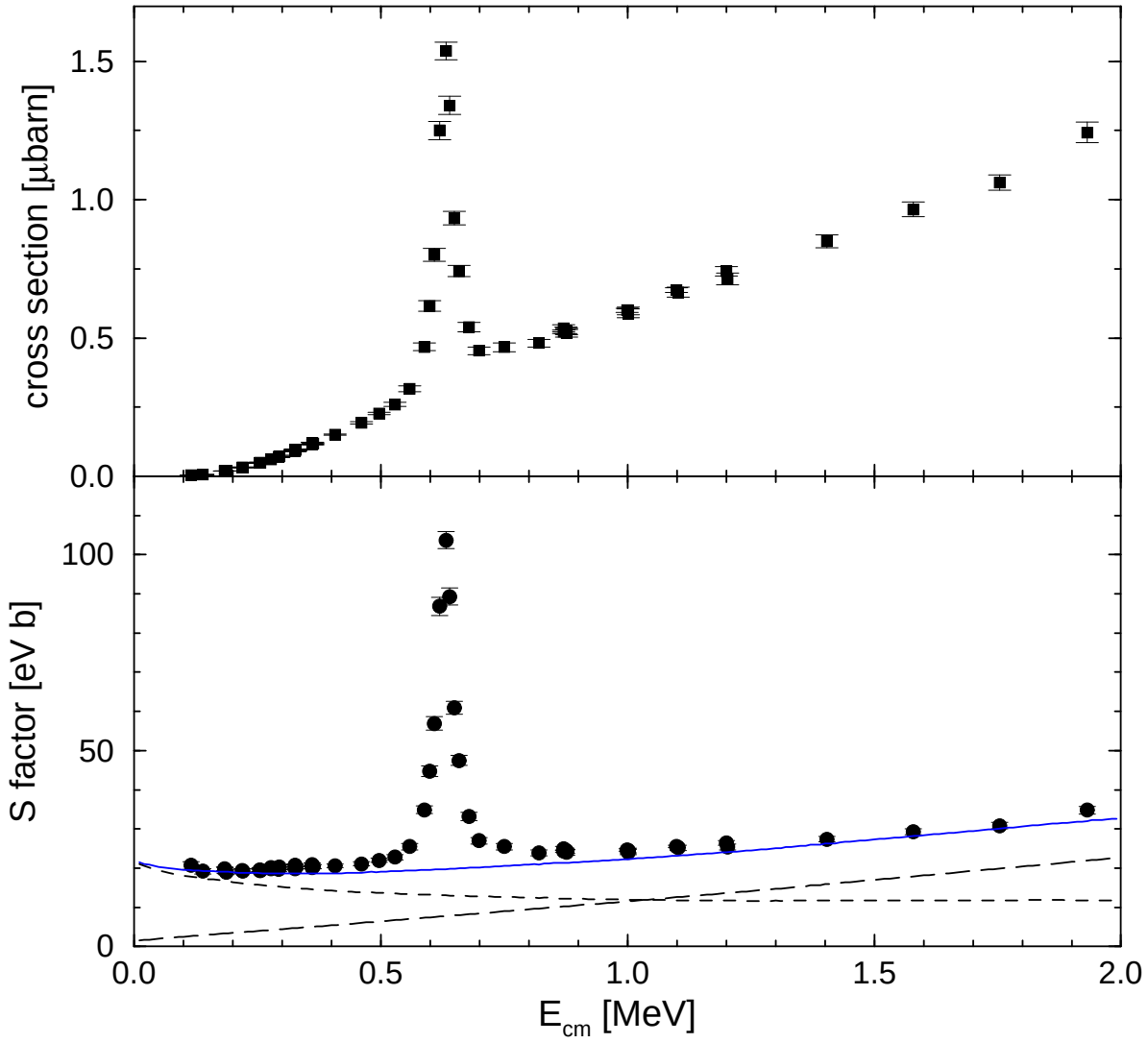

Figure 1.2: Top: ^{7}Be$(p,\gamma)^8$B cross section data of [Jun03]. Bottom: S-factor from [Jun03] shown with s-wave (dotted), d-wave (dashed) and total (solid) direct capture contributions (calculated with a potential model).

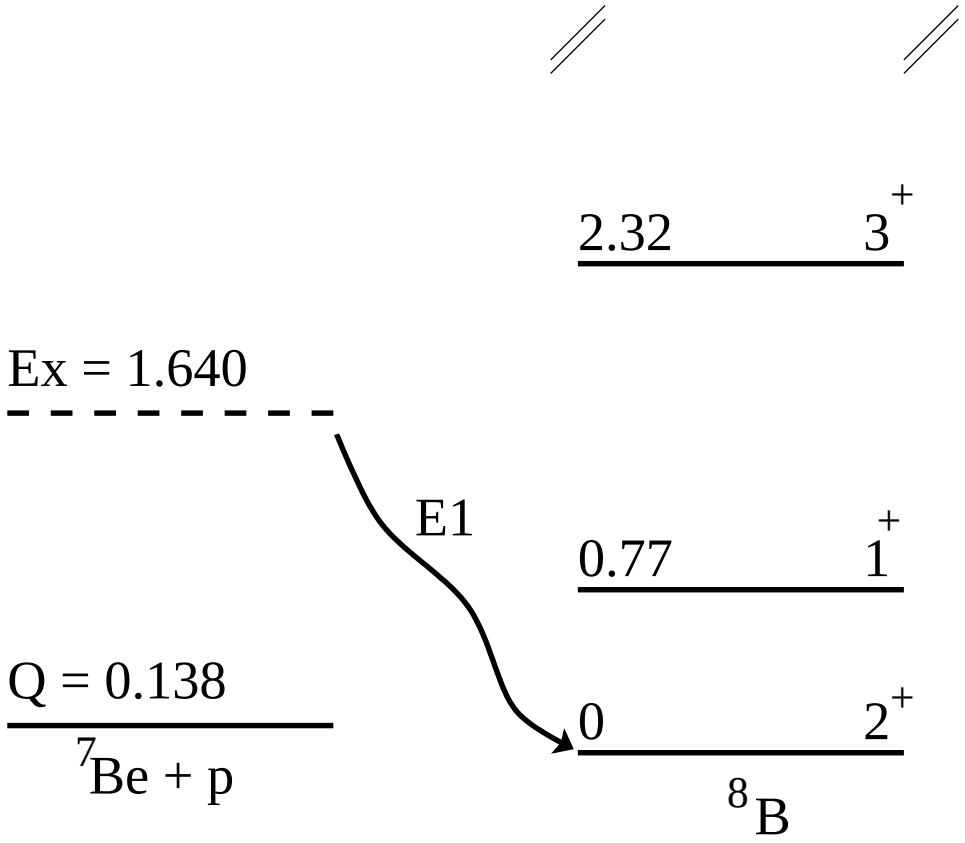

Figure 1.3: Energy level diagram for ^{8}B and showing the $^7\mathrm{Be}(p,\gamma)^8\mathrm{B}$ direct capture from $E_{cm} = 1.502\,\mathrm{MeV}$ to the ground state.

1.4 The $^7\mathrm{Be}(p,\gamma)^8\mathrm{B}$ cross section

For $E_{cm} < 2\,\mathrm{MeV}$, the $^7\mathrm{Be}(p,\gamma)^8\mathrm{B}$ reaction proceeds primarily through direct capture, as shown in Fig. 1.3. Also around $E_{cm} = 0.63\,\mathrm{MeV}$, resonant capture to the $E_x = 0.77\,\mathrm{MeV}$ state in ^{8}B contributes to the cross section as seen in Fig. 1.2. The $J^\pi = 3/2^-$ ^{7}Be ground state and $J^\pi = 1/2^+$ proton couple to form ^{8}B with channel spin $S = 1, 2$. Spectroscopic factors indicate that $S = 2$ is the dominant channel [Bar80]. Therefore, the initial state will likely interact via s-wave or d-wave and form the $J_\pi = 2^+$ ground state of ^{8}B by emitting an E1 γ-ray. As illustrated in Fig. 1.2, s-wave and d-wave both contribute, but the direct capture reaction is dominated by s-wave at low (stellar) energies. The 1^+ resonance is formed by a p-wave interaction.

1.4.1 Existing ^{7}Be$(p,\gamma)^8$B measurements

The ^{7}Be$(p,\gamma)^8$B cross section has been measured directly over a dozen times by various groups around the world [Kav60, Kav69, Par66, Vau70, Wie77, Bil83, Ham98, Has99, Ter01, Ham01, Str01, Jun03, Bab03]. The first measurement was reported by Kavanagh [Kav60] in 1960. All of the more precise measurements have used Parker's 1966 radioactive ^{7}Be target technique [Par66]. The number of fusions was determined by counting the β-delayed α emission of the ^{8}B ions implanted in the target. The early ^{7}Be$(p,\gamma)^8$B experiments were subject to similar systematic errors, including backscattering of ^{7}Be and ^{8}B from the targets. During the past 40 years, efforts have been made to improve the ^{7}Be targets and reduce the systematic errors. Recently, 2 measurements have been performed with ^{7}Be targets, leading to reported $S(0)$ values with less than 5% total uncertainty. They report values of $S(0) = 21.2 \pm 0.7$ eV·b [Bab03] and $S(0) = 22.83 \pm 0.4\,(\mathrm{exp}) \pm 0.5\,(\mathrm{theor})$ eV·b [Jun03]. These high-precision measurements have had significant impact on solar neutrino flux calculations (see Table 1.2). Fig. 1.4 shows the published results for direct measurements of ^{7}Be$(p,\gamma)^8$B. Only one, less precise direct measurement, [Ter01] was performed with a very different technique, using a ^{7}Be beam on a H_2 target (the lowest value in Fig. 1.4). The earliest measurements in Fig. 1.4, [Kav60], [Par66] and [Vau70], were re-analyzed by [Ham01] to account for an updated ^{7}Li$(d,p)^7$Li normalization cross section and the value reported by [Bil83] was re-analyzed by [Dav01].

Indirect measurements of the ^{7}Be$(p,\gamma)^8$B cross section have also been made in recent years [Kik98, Azh99a, Azh99b, Iwa99, Wan99, Dav01, Dav02, Oga03, Sch03, Tra03]. Coulomb dissociation (CD) of ^{8}B is the inverse process to ^{7}Be$(p,\gamma)^8$B and provides information about the cross section for the latter. However, due to the higher energies involved, questions remain about the extent to which higher order transitions contribute to the process. Recent CD experiments report S(0) = 17.8±1.8 eV·b [Dav02] and S(0) = 18.6±1.6 eV·b [Sch03]. Also, asymptotic normalization coefficients (ANC's) from transfer reactions have been used to determine the ^{7}Be$(p,\gamma)^8$B cross section. The most recent ANC measurement leads to, S(0) = 17.6±1.7 eV·b [Tra03].

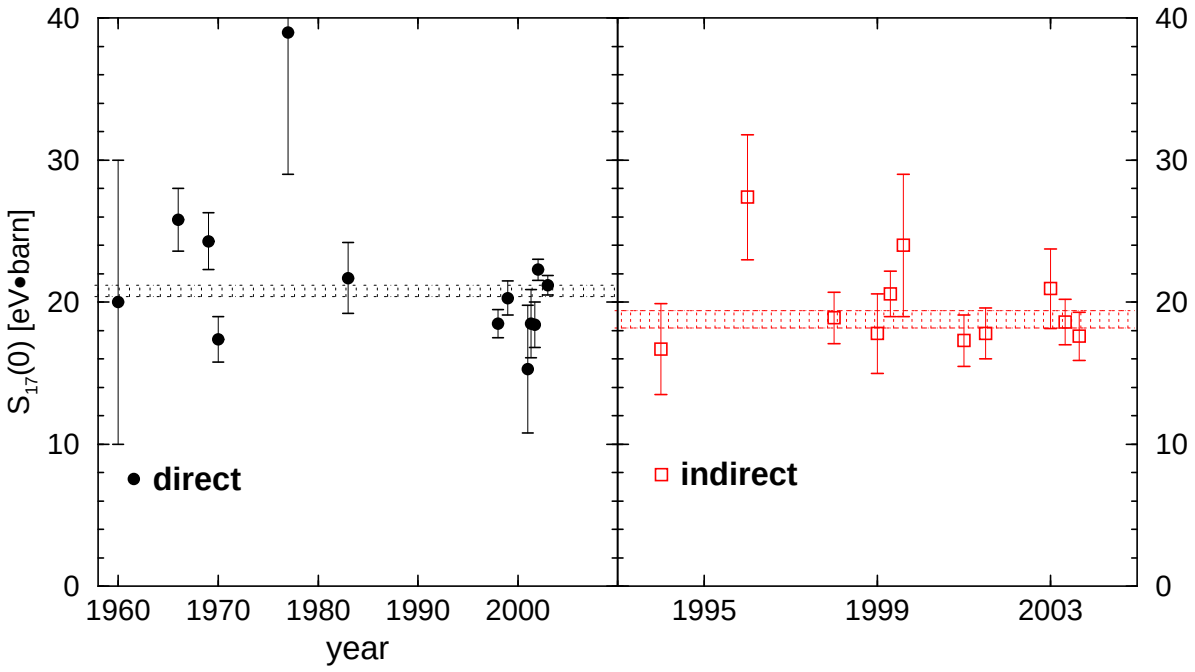

Figure 1.4: Literature values for the ^{7}Be$(p,\gamma)^8$B S-factor. The bands show the weighted mean and standard deviation for direct (left) and indirect (right) measurements. See text for literature references.

All of the reported $S(0)$ values are shown in Fig. 1.4, divided into direct and indirect measurements. The error-weighted means and standard deviations of those means are shown by the bands. The weighted mean of the direct measurements is $\mathrm{S}(0) = 20.8 \pm 0.4$ with $\chi^2/\nu = 31/12$ and for the indirect measurements is $\mathrm{S}(0) = 18.8 \pm 0.6$ with $\chi^2/\nu = 9/10$. Combining all of the direct and indirect measurements gives $\mathrm{S}(0) = 20.3 \pm 0.3$ with $\chi^2/\nu. = 46/23$. All the measurements are shown together in Fig. 1.5, with the indirect measurement separated by method (ANC and CD).

All the determinations of the ^{7}Be$(p,\gamma)^8$B S-factors have been extrapolated to $E = 0$ using theoretical models [Tom65, Bar80, Wil81, Bar95, Des88, Des93, Dav03]. The most widely used is the microscopic model of [Des88, Des93] (DB). On the other hand, [Dav03] used a potential model to extrapolate the S-factor. In a recent review [Cyb04], the DB model was shown to give a 5% higher $S(0)$ value than the potential model for the combination of all the ^{7}Be$(p,\gamma)^8$B data below $E_{cm} = 425\,\mathrm{keV}$.

Given that the above mentioned experiments use some of the same techniques and the same two models for extrapolation, the weighted means listed are not the best

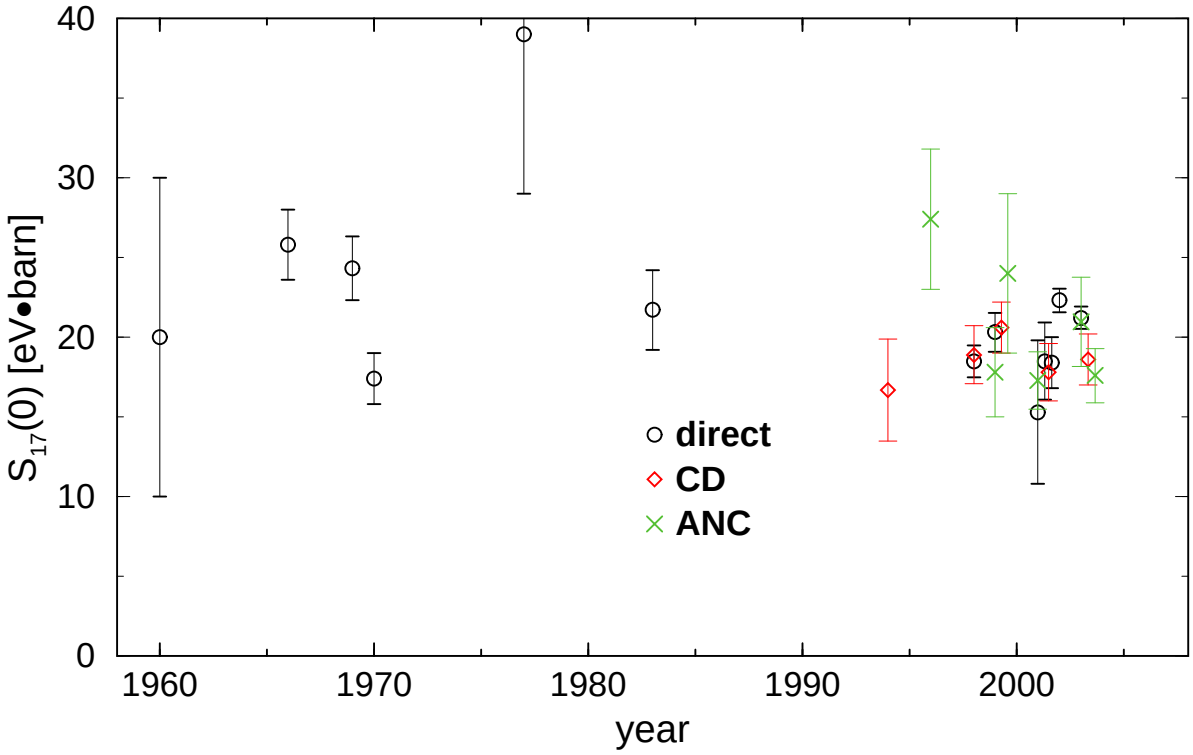

Figure 1.5: Literature values for the ^{7}Be$(p,\gamma)^8$B S-factor. See text for references.

estimate of $S(0)$. Although $S(0)$ is sometimes calculated in this way [Bab03], the model dependence and systematic correlations have been explored by various other authors [Jen98, Sch03, Dav03, Sno04, Cyb04]. For instance, Fig. 1.6 shows model calculations for the E1 ^{7}Be$(p,\gamma)^8$B cross section, normalized to $S(0)$. For low energy data ($E < 0.5$ MeV), the two cluster models agree well. However, the cluster and potential models are shown to disagree, especially at higher energies. Higher energy ^{7}Be$(p,\gamma)^8$B data then, would help to clear up the model dependence. Also, [Cyb04] analyze the ^{7}Be$(p,\gamma)^8$B literature data assuming both independent and correlated non-statistical errors for each experiment. They report values of $S(0) = 20.7 \pm 0.6 \pm 1.0$ eV·b and $S(0) = 21.4 \pm 0.5 \pm 1.4$ eV·b for each case respectively. The results of [Cyb04] are summarized in Table 1.3 and Fig. 1.7, where the grey band represents the average of the two above values. The [Jun03] measurement dominates the mean value for $S(0)$ and the discrepancy between the (p,γ) value and the CD value. Also, the error assigned to the ^{7}Be$(p,\gamma)^8$B cross section in the SSM is represented by the orange band in Fig. 1.7, and is outside the error bars of the non-Seattle

capture results, and the indirect measurements.

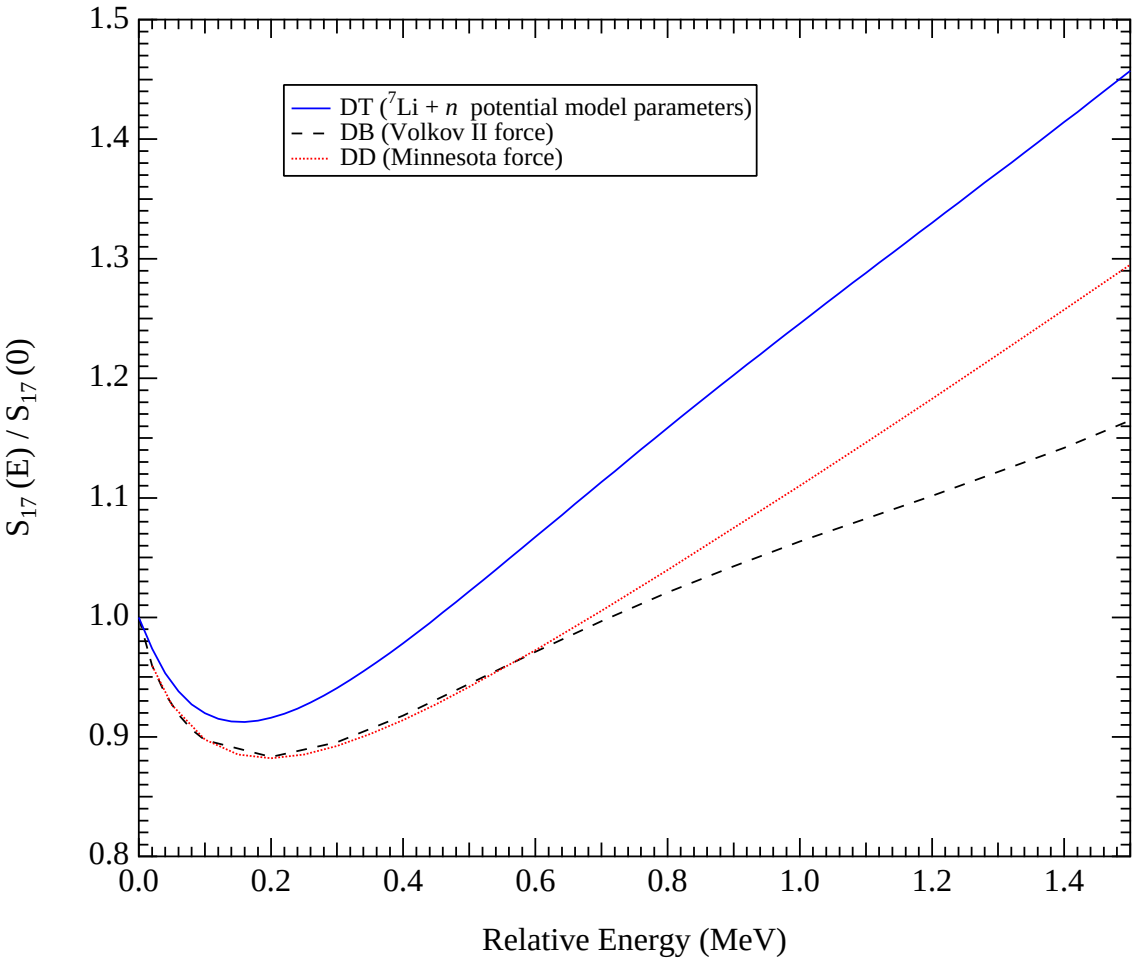

Figure 1.6: Model calculations reported in [Cyb04]. The top line (DT) is from a potential model and the other two result from cluster models. Lines are normalized to $S(0)$ from each model.

$S(0)$ (ev·b)	data set
20.7±1.2	all (p,γ)
21.4±3	[Jun03] only
16.3±2.4	all (p,γ) except [Jun03]
17.5±2.5	CD
17.8±1.0	ANC
21.4±0.8	SSM

Table 1.3: Summary of the $S(0)$ analysis from [Cyb04] (first 5 values), and the SSM adopted value. Only the results of the analysis assuming uncorrelated errors are shown here (black circles in Fig. 1.7. The ANC value is the weighted mean of the three measurements reported by [Cyb04]. The SSM value is that adopted by [Bah04].

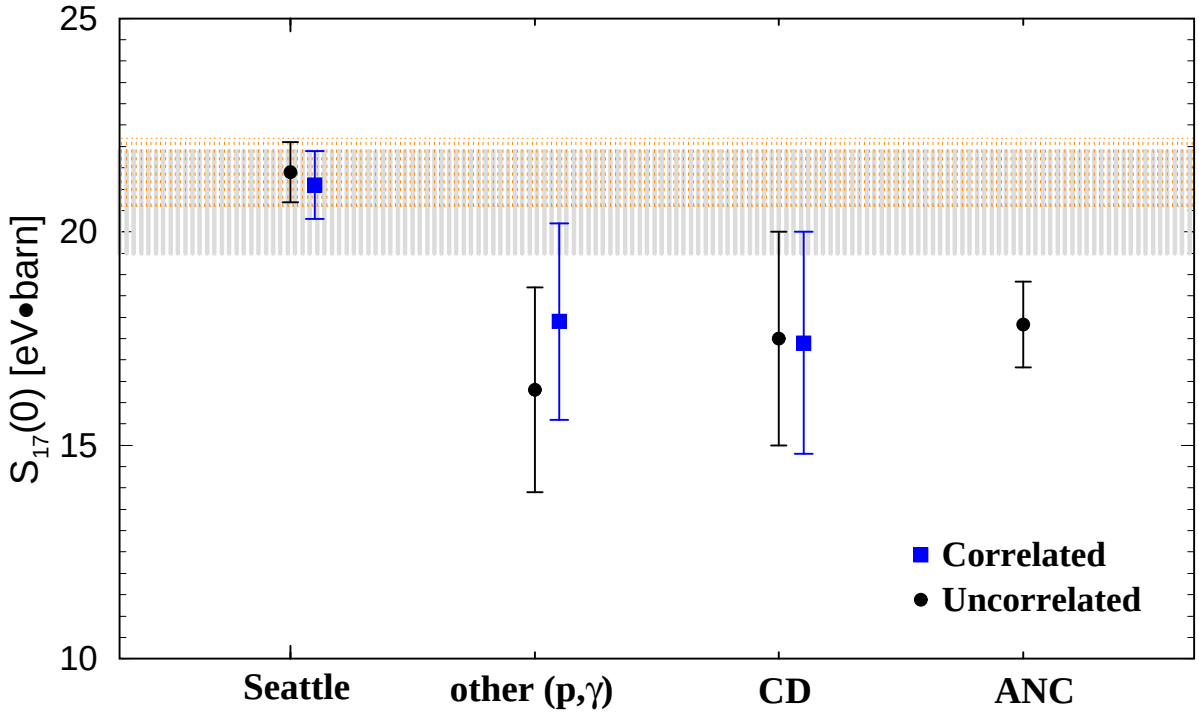

Figure 1.7: Summary of $S(0)$ analysis from [Cyb04] for correlated and uncorrelated errors, showing the Seattle result, other direct measurement results, CD and ANC results. The large grey band is the average of all the direct measurement results (see text). The orange band represents the assigned error band from the SSM [Bah04].

1.4.2 Present work

The present work focuses on the development of a new approach for the measurement of ^{7}Be$(p,\gamma)^8$B , using a ^{7}Be beam and a hydrogen gas target at Oak Ridge National Laboratory (ORNL). This use of a heavy beam on a light target is referred to as "inverse kinematics", i.e. ^{1}H$(^7$Be$,\gamma)^8$B. The cross section measured is identical to that measured in "normal kinematics" for the same energy in the center of mass system. The possible systematic errors for this measurement are different from those from the normal-kinematics ^{7}Be$(p,\gamma)^8$B measurements. In the ORNL experiment, the target is known to be pure H_2 and to be of intransigent composition and thickness. Also, since a transmission target and heavy ion beam are used, the beam normalization method differs from normal-kinematics measurements. Furthermore, the transmission target allows the recoils to be detected directly, and the systematic error in the number of fusions is decreased in the ^{1}H$(^7$Be$,\gamma)^8$B measurement, due to high recoil-detection efficiency and low background. However, low ^{7}Be beam current limits the statistical precision of the measurement. The goal of this work then was to design an experiment to measure the ^{1}H$(^7$Be$,\gamma)^8$B cross section. Precise measurements of both the absolute normalization, and the shape of the high-energy cross section are needed. Due to the statistical limitations, our initial efforts will focus on the higher energy region of the cross section ($1\,\mathrm{MeV} < E_{cm} < 2\,\mathrm{MeV}$), where the cross section is highest and where the largest discrepancy exists among the various models (Fig. 1.6).

Chapter 2

Experimental equipment and technique

2.1 Introduction to the method

Cross section measurements of proton capture reactions involving short-lived targets require inverse kinematics, in which a beam of the radioactive isotope interacts with a proton target. These reactions often occur in explosive environments, such as X-ray bursts and novae, as well as in quiescent hydrogen burning scenarios ($^{7}\mathrm{Be}(p,\gamma)^{8}\mathrm{B}$). This approach is not limited to just these cases since it provides some advantages for long-lived or even stable nuclei.

Recent inverse kinematics (p,γ) measurements include $^{21}\mathrm{Na}(p,\gamma)^{22}\mathrm{Ne}$ at TRIUMF [D'A04, Eng03] and a measurement of $^{1}\mathrm{H}(^{7}\mathrm{Be},\gamma)^{8}\mathrm{B}$ at $E_{cm} = 1$ MeV by the NABONA collaboration [Ter01]. Some advantages of this method for $^{1}\mathrm{H}(^{7}\mathrm{Be},\gamma)^{8}\mathrm{B}$ are described in Sec. 1.4.2. For astrophysical scenarios, the total cross section, $\sigma(E)$, is of interest. In "normal" kinematics, the center-of-mass velocity is low so that reaction products and γ-rays are are emitted in all directions, and thus the differential cross section is measured over an incomplete range of angles. Then, $\sigma(E)$ is inferred from the differential cross section. On the other hand, in an inverse kinematics reaction, the center of mass moves at a high velocity and therefore the recoil nuclei are focused into a forward-focused cone in the laboratory frame. For some reactions, the complete angular range of recoils can

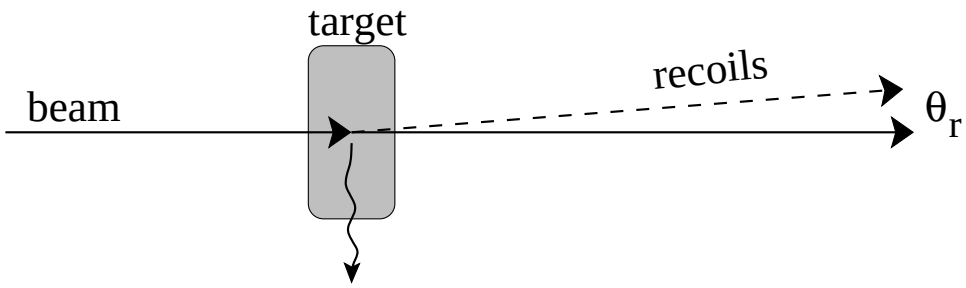

Figure 2.1: Inverse kinematics schematic showing maximum recoil scattering angle, θ_r.

be detected and the total cross section measured directly. This occurs for reactions in which the maximum lab angle between the recoils and the beam, θ_r, which is usually less than 1° for low energy (p,γ) reactions, is within the angular acceptance of the detection system. A recoil scatters at θ_r when the reaction γ-ray is emitted at 90° in the laboratory. From Fig. 2.1 and applying conservation of momentum, it can be seen that θ_r is determined by the momenta of the recoil and γ-ray,

$$\theta_r \;=\; sin^{-1}\left(\frac{p_\gamma}{p_{recoil}}\right), \tag{2.1}$$

where p_γ and p_{recoil} are determined from the conservation of momentum and energy. Thus, for (p,γ) reactions with low Q-values, measured at the low energies relevant to astrophysics, the capture γ-rays tend be low energy ground state transitions and thus recoil trajectories have small scattering angles (θ_r). In these cases, the recoils and beam have nearly identical momenta, and Eqn. 2.1 can be expressed as,

$$\theta_r \;\approx\; sin^{-1}\left(\frac{E_{cm}+Q}{p_{beam}\;c}\right), \tag{2.2}$$

where c is the speed of light. In the case of ^{1}H(^{7}Be,γ)^{8}B at $E_{cm}=1.0$ MeV, a 90° γ-ray has $p_\gamma=1.142$ MeV/c, and the corresponding ^{8}B recoils at $\theta_r=0.202°$. This angle is similar to the divergence of the ion beam itself, and is small enough to pass through the target and recoil separator. See Sec. 2.4 for an in-depth analysis of the recoil transmission.

The experimental setup for the ^{1}H(^{7}Be,γ)^{8}B cross section measurement at The Holifield Radioactive Ion Beam facility (HRIBF) at Oak Ridge National Laboratory

(ORNL) is described briefly in [Fit05] and is shown in Fig. 2.2. The first element in the setup is a multi-sample sputter source, which produces a low energy beam of $^{7}BeO^{-}$ (see Sec. 2.2.3). This beam is accelerated to the terminal of the NEC folded tandem Van DeGraff accelerator (25 MV maximum potential). There, it is broken up by a gas stripper, $^{7}Be^{1+}$ is mass analyzed and accelerated down the tandem. The specific charge state is selected for its intensity and tuning efficiency for a given final beam energy. One advantage of the ORNL system over that used by NABONA is the ability to run the terminal at potentials higher than 3 MV, and thus accelerating an initial $^{7}Be^{1+}$ beam to more than 9 MeV if desired. The tandem transmission increases with terminal potential, and using sub-equilibrium gas stripping at the terminal, a large fraction of the initial beam exits the terminal as $^{7}Be^{1+}$. Therefore, the ability to run higher terminal potentials increases the total ^{7}Be beam on target. Also, the sputter cathode contains similar amounts of ^{7}Be and ^{7}Li. To eliminate the presence of ^{7}Li , the beam can be post-stripped to $^{7}Be^{4+}$. The pure $^{7}Be^{4+}$ beam is then steered to the windowless gas target (WGT) (Sec. 2.3) at $6{\cdot}10^{19}$H atoms/cm^2. Mounted within the gas target are Si surface barrier detectors at a forward angles of $\pm 45^{\circ}$ for monitoring the beam current. The fusion recoils continue forward through the Daresbury Recoil Separator (DRS) (Sec. 2.4), where they are separated from the bulk of the ^{7}Be beam, and are finally detected and identified in the gas filled ion counter (IC) (Sec. 2.4.2).

Using this method, the total cross section in units of cm^2 is determined by,

$$\sigma(E) \;=\; \frac{N_B \; R}{N_{mon} \; \Phi_{5+} \; n \; \epsilon_{DRS}}, \tag{2.3}$$

where N_B is the number of ^{8}B recoils detected at the focal plane, N_{mon} is the number of elastically scattered protons in the monitor detectors, n is the areal target density in atoms/cm^2, , Φ_{5+} is the fraction of ^{8}B recoils in atomic charge state 5+ and ϵ_{DRS} is the DRS transmission. R is the ratio of monitor counts to ^{7}Be beam particles, and was measured as described in Sec. 4.4.

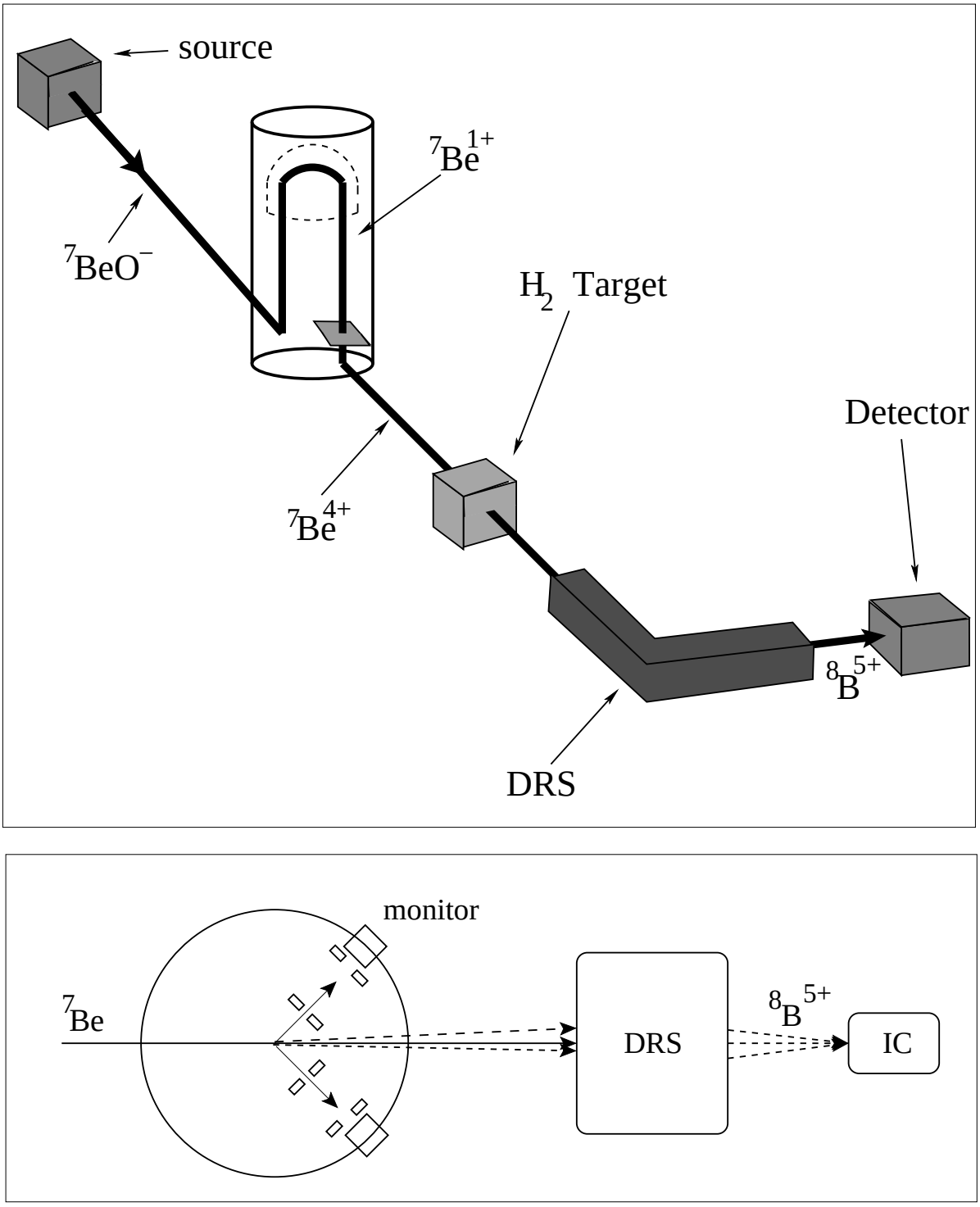

Figure 2.2: Top: Experimental layout at HRIBF. Bottom: DRS end-station showing target, 45° monitor detectors and gas filled ion counter at the focal plane of the DRS.

2.2 ^{7}Be beam

The first step in producing a beam of ^{7}Be was to produce the ^{7}Be at the Triangle Universities Nuclear Laboratory (TUNL) using the ^{7}Li$(p,n)^7$Be reaction. Next the ^{7}Be impregnated ^{7}Li ingot was shipped to ORNL, and Be^{7}O was chemically isolated. Finally, the Be^{7}O was mixed in a powder matrix and pressed into a pellet for use in a sputter ion source. As of April 2005, ^{7}Be beams made in this way were used for ^{1}H$(^7\mathrm{Be},\gamma)^8$B, ^{1}H$(^7$Be,^{7}Be$)^1$H, ^{1}H$(^7$Be,^{7}Be$^*)^1$H$'$ and ^{2}H$(^7\mathrm{Be},t)^6$Be experiments at ORNL's Holifield Radioactive Ion Beam Facility (HRIBF).

2.2.1 ^{7}Be production at TUNL

The ^{7}Li$(p,n)^7$Be reaction used for ^{7}Be production has been well studied [Lis75, Abr84] and the cross section is shown in Fig 2.3 (top). This reaction has been used in the past to produce material for ion-source cathodes and targets [Par66, Ter01, Gia02, Jun03]. A 3 mm ^{7}Li target thickness was selected to maximize the ^{7}Be yield, while keeping the amount of Li to a minimum. The later requirement is dictated by the fact that any ^{7}Li in the ion source will emerge as a ^{7}Li beam and will be transported along with the ^{7}Be. Thus, the yield was calculated for various target thicknesses and beam energies using a modified version of Eqn. 1.13,

$$Y(E_o) = \int_{E_{th}}^{E_o} \frac{\sigma(E)}{\epsilon(E)} dE, \tag{2.4}$$

where $\sigma(E)$ is the ^{7}Li$(p,n)^7$Be cross section and ϵ is the stopping power taken from the SRIM program [Bie95]. The reaction threshold is $E_{th} = 1.880$ MeV, and the thick target yield is dominated by resonances at $E_p = 2.25$ MeV and $E_p = 4.9$ MeV (Fig. 2.3). Thus a target needs to be thick enough for the beam to cover this energy range. Fig. 2.3 shows that the yield increases 25% between 1.5 mm and 3.0 mm of Li. It only increases about 10% more at 4.5 mm. Thus, 3.0 mm was chosen as a compromise between increased yield and superfluous Li metal. Furthermore, Fig. 2.3 shows that at higher energies, the beam will not lose enough energy to reach the low energy resonance. Also, a possible

hindrance to ^{7}Be production is oxidation of the Li target. Li metal has a stopping power of $\epsilon = 0.44$ eV$\times$cm$^2/10^{15}$ atoms whereas Li_2O, which is the most common oxide of Li, has an effective stopping power of $\epsilon = 0.97$ eV$\times$cm$^2/10^{15}$. According to Eqn. 2.4, solid Li_2O has a lower ^{7}Be yield. Furthermore, a surface oxide layer on the ingot would cause faster energy loss (and poorer heat conduction). Thus, data were taken with a 3.0 mm target to determine the best beam energy more precisely. As shown in Fig 2.4, the ideal beam energy on target is 0.7 MeV higher than predicted for a pure Li metal target, and as expected the energy dependence of the yield is not very strong. In most cases, beam energies between 10.5 and 11.5 MeV were used with 3.0 mm Li targets.

The ^{7}Be was produced using the FN tandem facility at TUNL. The TUNL floor plan is show in Fig 2.5. The Direct Extraction Negative Ion Source (DENIS) produced up to 25 μA of H^- which was extracted by a 75 kV electrode. The proton beam was accelerated by the FN tandem accelerator, which has a maximum terminal potential of 10 MV. For the present work, the terminal was set between 4 and 5.5 MV. Up to 20 μA of proton beam passed through the tandem, emerging at up to 11.0 MeV. The current was typically kept at 10-15 μA. This was done firstly to protect the target from overheating, secondly to limit the neutron radiation in the control room, and thirdly to protect the tandem from surges in column current and γ-ray flux. Typical FN column currents during operation were $\approx 20\,\mu$A. If a 20 μA proton beam is suddenly stopped on the low-energy end of the accelerator, the column current and terminal potential will temporarily spike, while the upcharge is recovering. This effect can cause sparking or column damage.

An end station was constructed directly after the 0° exit port of the 20-70 switching magnet. This site was selected so that the high-energy beam would travel a short, straight line from the tandem to the target, minimizing beam loss. This design was crucial to achieve high beam current on target required while minimizing the radiation produced by interactions between the beam and other materials (eg. slits or beampipe). Also, as seen in Fig 2.5 the target location was shielded by 1 m of concrete, and the side of the target facing the control room was shielded by 1 m of water as well as a 1 m concrete wall. Furthermore, ≈ 1 m of paraffin wax was stacked immediately surrounding

the target, only leaving a hole for the upstream beam pipe. Unfortunately, the close proximity of the target to the metal door leading to the control room resulted in considerable neutron radiation in the control room during bombardment. The neutrons came both from the target (1 per ^{7}Be) as well as from the unshielded slits upstream of the target. During operation, the neutron radiation was typically 0.3-2 R/hr at a distance of 5 m from the target, 0.5-3 mR/hr immediately inside the control room door, and 0.1-0.5 mR/hr in the center of the control room. The target beamline (Fig 2.6) consists of a magnetic quadrapole doublet directly after the tandem and a set of x and y magnetic steerers followed by a set of x-y slits. These elements were used to center the beam for passage through the 20-70 switching magnet, which was not used for 0° operation. The 20-70 magnet was deGaussed using a 5 V bi-polar power supply. Although the beam energy was un-analyzed, the calibrated GVM was used to stabilize the tandem. Directly upstream of the target are a beam profile monitor (BPO) and a 1.9 cm diameter water cooled Ta aperture. The aperture was located 30 cm upstream of the target.

The targets consist of a 2.0 cm diameter by 3 mm thick natural Li (92.5% ^{7}Li [Tul95]) disc pressed into a Cu mold. Al and Cu molds were both tested. The beam activation of Al lead to shorter-lived isotopes than the Cu, and was thus safer to handle after the 12-24 hour cooling period. However, Cu has better thermal conductivity and behaved much better during the chemical separation of the ^{7}Be from the Li/Cu metal. The Li pellet + Cu mold is hereafter referred to as "the ingot". The target was assembled in an Ar filled glove box. First, two 1.5-mm-thick × 20 mm diameter discs were punched out of a roll of Li metal with a custom stainless steel punch. The Li discs were stacked in the the 4 mm deep blind hole in the Cu mold. This was topped with an Al rod and pressed in a hand vice at ≈100 psi. The surface of the Li was usually partially darkened by this point as some surface oxidation occurred. The ingot was then loaded into the target body and the cap screwed on. The cap had a 1" hole in the center in which is mounted a 0.002" Al foil. This foil was used to contain any back-scattered ^{7}Be. For the first 2 years of operation the ingots were mounted in an Al target body, as shown in Fig. 2.7. The target body was water-cooled by an isolated supply of distilled water, which was passed through a heat exchanger kept at 52°. The target assembly was sealed in a plastic bag

or desiccator and carried $\approx$ 30 m to the end station. The target body was mounted in a standard 4" Dependex tee at the end of the beamline. The beamline was filled with Ar before the target was inserted, then quickly pumped down to $\approx 1\times 10^{-6}$ Torr. The target body was electrically isolated by a plastic centering ring so that the approximate beam current could be read directly off of the top of the target body. The target body rested, unclamped, on the tee with only atmospheric pressure (≈ 2000 N) to maintain the o-ring seal.

During initial tests of this system, the ^{7}Be yield was below expectations and a small ($\approx$ 1 mm) beam spot could be seen on the surface of the Li targets. In some cases, the beam bored through the target over a 24 hour period of running. To address this problem, a beam profile monitor (BPO) was installed so that the beam could be reliably enlarged to cover the whole Li target, thereby reducing the power density, with $\approx$ 10% of the beam on the aperture. The target holder described above was used for two years and the ^{7}Be produced was used to develop the chemical processing procedure and to make beams for ^{1}H(^{7}Be,^{7} Be)^{1}H and $^2H(^7\mathrm{Be},^3 H)^6$Be measurements at ORNL. However, the overheating problems were not completely solved despite the attention paid to beam spot size. This may have been due to the doubly-indirect water cooling design. It is not possible to directly cool the Li pellet with water, as Li is highly reactive. Furthermore, after repeated assemblies, the Cu disks may not have been seating properly in the cooled Al backing. Thus, in December 2004, a second target assembly was designed. As shown in Fig. 2.8, the new design features more direct cooling. Also, the water reservoir was reduced in size and the feeds were designed to reduce the formation of dead-spaces. Another change was the removal of any Al from the target because it was found interfere with the ^{7}Be chemistry. To this end, the front piece was still made of Cu, but the back was changed to stainless steel to reduce binding with the Cu ingot. Also, a second x-y steerer was added between the 20-70 magnet and the BPO. The power supplies for this steerer were driven by function generators in order to raster the beam across the target. The result of these changes was a significant reduction in the heat damage to the targets.

Initial test runs were 2-3 days in duration, after which, the target body was removed

date	activity (mCi)	motivation	beam current (pps)
Aug 2001	2	radiation test	—
Oct 2001	38	production test	—
Aug 2002	14	chemistry test	—
Jan 2003	25	source test	—
Jun 2003	35	source test	—
Sep 2003	30	source test	—
Oct 2003	35	(p,p)	$2 \cdot 10^6$
Sep 2004	125	(d,t) and (p,γ)	$2 \cdot 10^6$
Jan 2005	240	source test, (p,γ), (p,p) and (p,p')	$1.5 \cdot 10^7$

Table 2.1: The history of ^{7}Be production at TUNL. Column 1 is the production date, column 2 is the total activity made and column 3 states the motivation for the production. Beam intensities are pps on target. In Sep 2004, the beam intensity was too low to measure ^{1}H(^{7}Be,γ)^{8}B as planned.

from the beamline using a 50 cm long handle and placed in a 5-sided, 5 cm thick Pb cradle. The ingot was placed in a 0.13 mm plastic sleeve, heat sealed and deposited in a Pb pig. The pig was a 30 cm diameter $\times$ 30 cm long cylinder and was designed to reduce 1 Cu of ^{7}Be activity to than 5 mRem/hr at the surface. The pig was shipped to ORNL in a large metal can. The ^{7}Be activity was measured using HPGe detectors at TUNL and/or ORNL. The HPGe used at TUNL had an absolute-peak efficiency $(9.4 \pm 1.0) \cdot 10^{-6}$ at 478 keV. During the final production, 10 μA of 8-11 MeV proton beam bombarded 3 mm thick targets for up to 48 hours per target. 24 hours of runtime at 10 MeV yielded 35 mCi and 48 hours or runtime at 8 MeV yielded 60 mCi. The process lasted 12 days, with 7.6 days of beam-on-target. A total of 240 mCi ^{7}Be was produced, and shared by five ingots. The complete history of ^{7}Be production runs at TUNL is shown in Table 2.1.

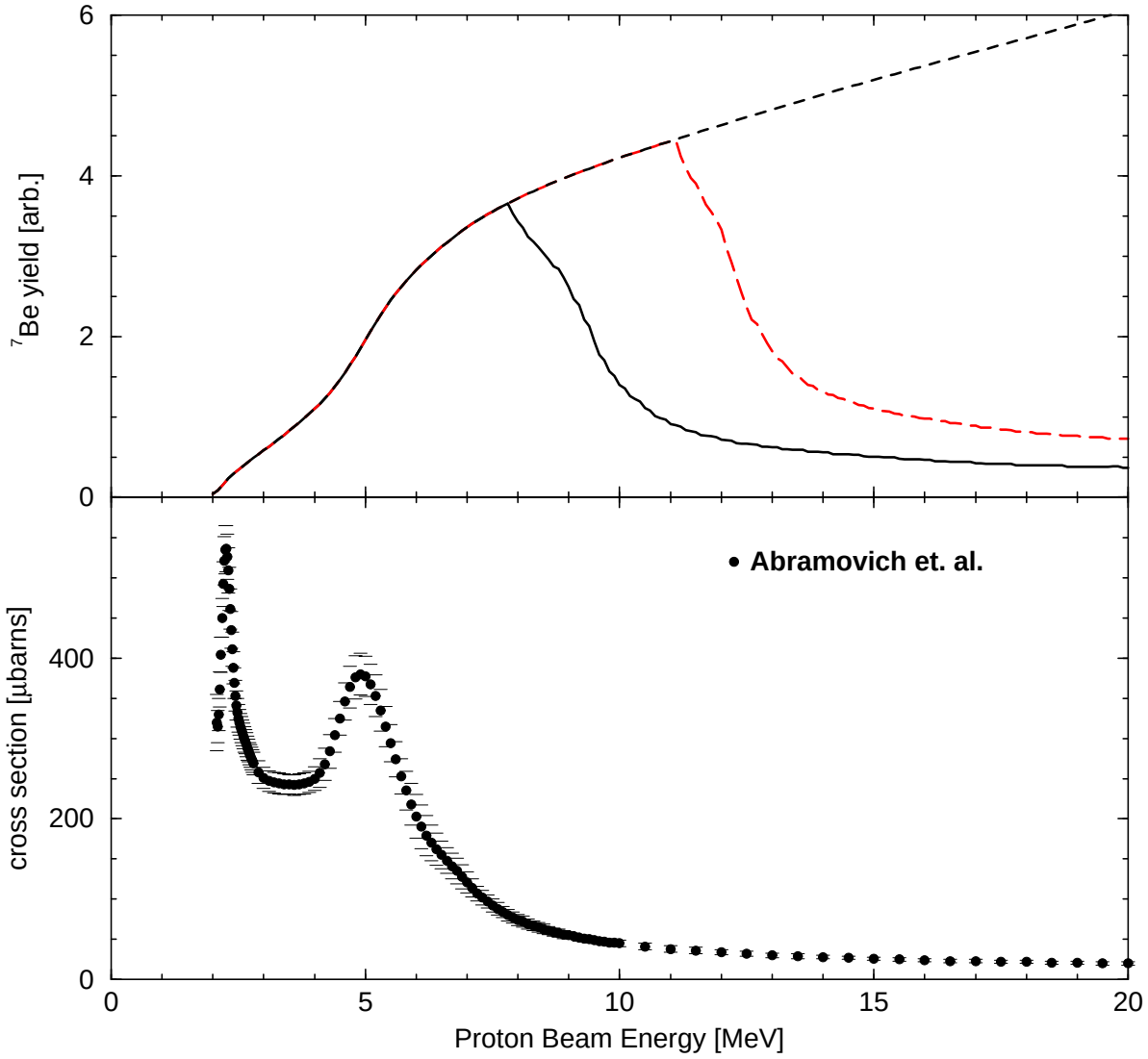

Figure 2.3: Top: calculated yield for a 1.5 mm (solid), 3.0 mm (dashed) and ∞ (short-dash) thick Li target using Eqn. 2.4. Bottom: The ^{7}Li$(p,n)^7$Be cross section data from [Abr84].

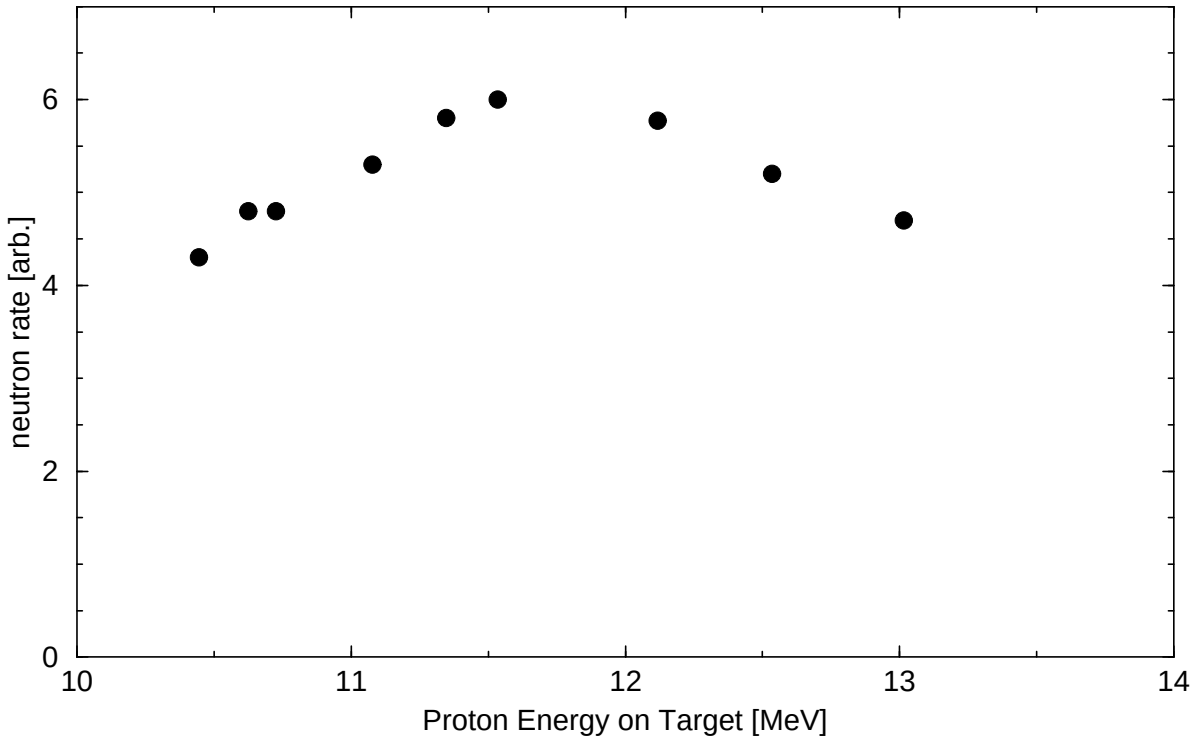

Figure 2.4: Neutron yield vs. proton energy on target for a 3.0 mm Li target. The peak at is at 11.7 MeV and was expected to be 11.0 MeV.

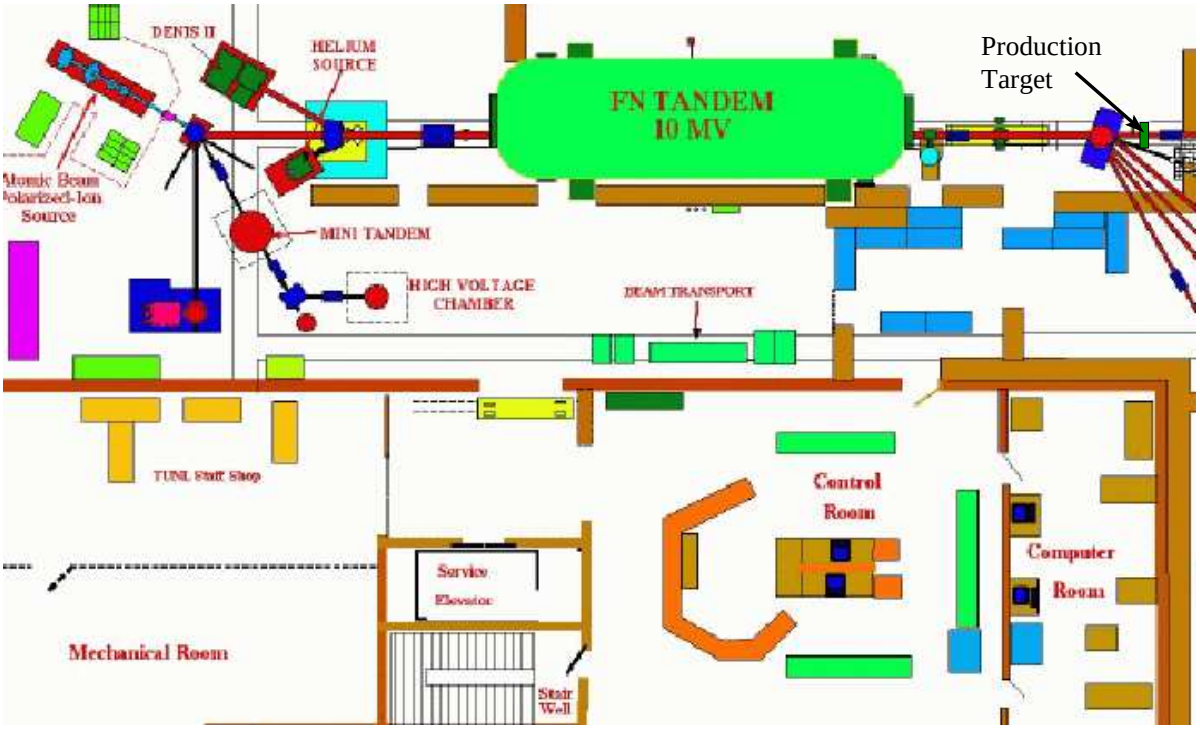

Figure 2.5: TUNL floorplan showing FN tandem and 0°beamline.

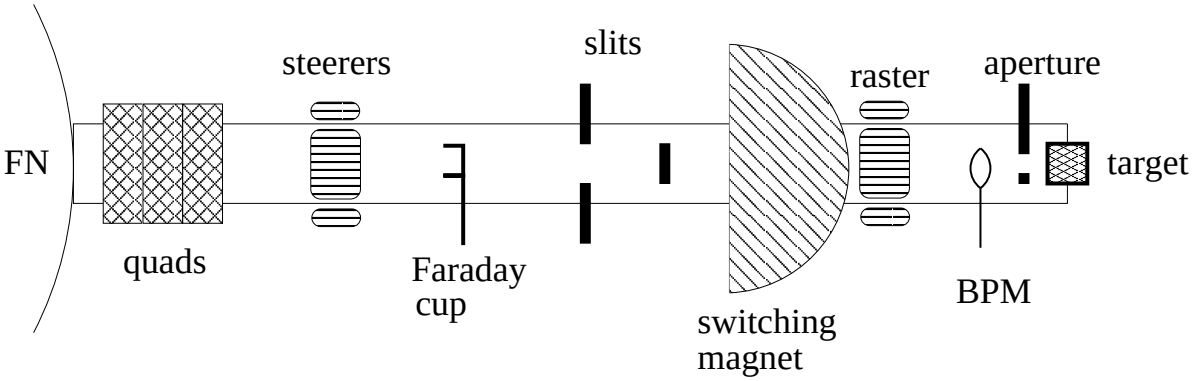

Figure 2.6: The ^{7}Be production target chamber. The paraffin shielding surrounding the target is not shown.

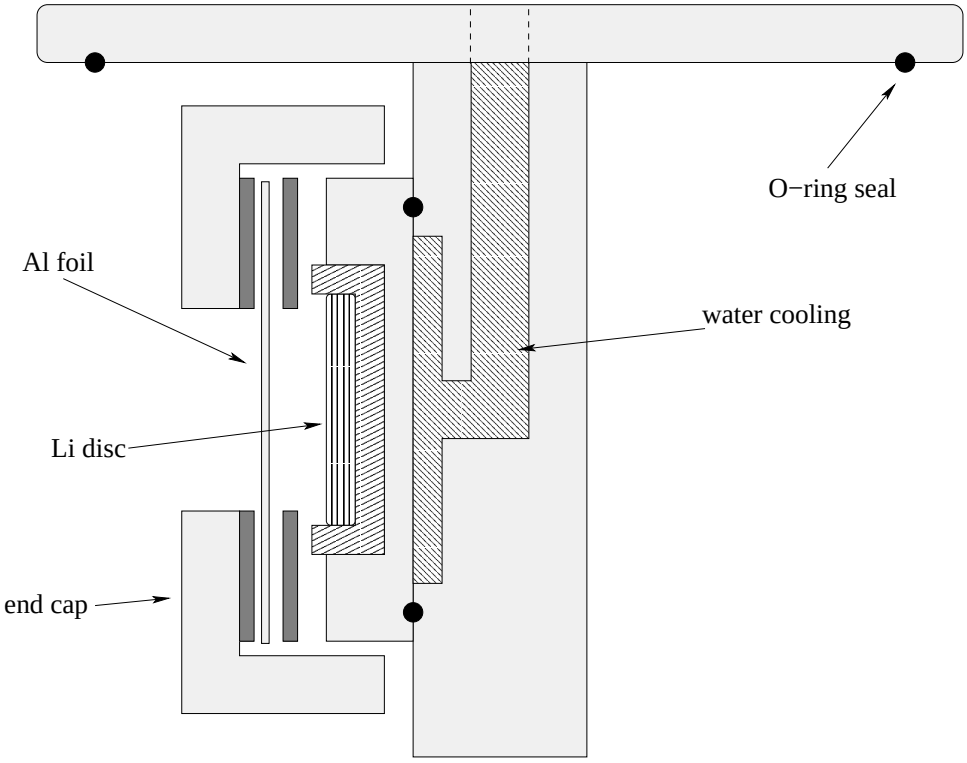

Figure 2.7: Cross section view of the first ^{7}Be production target (drawn roughly to scale). The O-ring seal is on a 4" diameter.

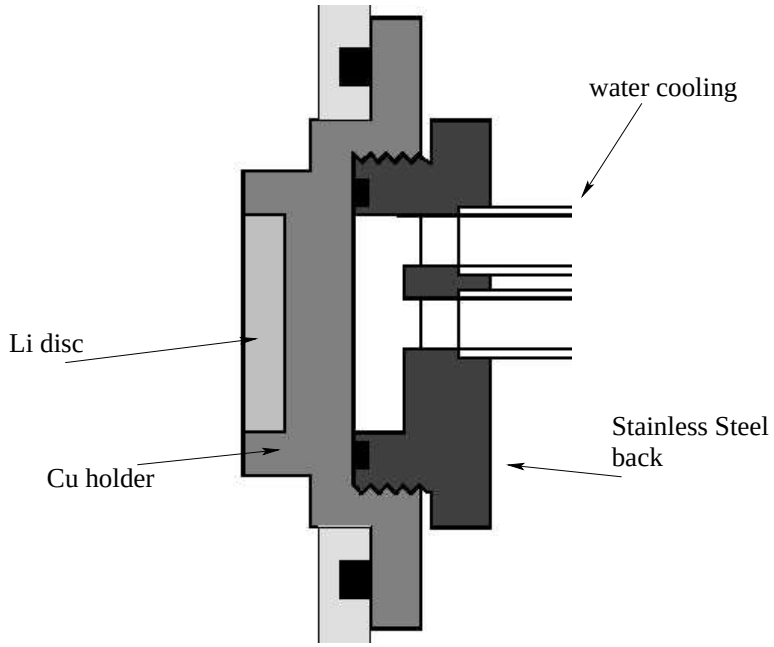

Figure 2.8: Cross-section view of the second ^{7}Be production target (drawn to scale). Target features better water cooling, and less Al metal.

2.2.2 ^{7}Be cathode production at ORNL

The ^{7}Be was chemically isolated from the Li and other ingot contaminant elements at a radioactive chemistry laboratory that was setup at ORNL. General radiochemical procedures for ^{7}Be have been documented by Fairhall [Fai60]. The procedure used at ORNL is nearly identical to that developed by [Gia02], which was based on the procedure used by [Kav60]. All the chemistry was done in a negative pressure fume hood, shown schematically in Fig 2.9.

It should be noted that Be is a toxic substance and even small amounts of Be inhaled in the lungs can lead to Chronic Beryllium Disease (CBD), which causes painful scarring of lung tissue and possibly death. The OSHA limit for Be exposure is 2 μg/m^2 over an 8 hour shift. It is well known, and acknowledged by OSHA that this limit is inadequate to prevent CBD [Sob01]. Thus, DOE has enacted an "action level" of 0.2 μg/m^2 exposure to further reduce the risk of illness. The limiting quantity of Be processed in this hood was 300 mCi = 0.87 μg. So even if all the Be became airborne in the hood, normal airflow would prevent concentrations from reaching the action level. The airflow in the hood was continuously monitored and air samples periodically taken. The air samples were tested for ^{7}Be (the only isotope of Be present) and did not show a trace of activity. The air samples were sensitive to less than a 2 nCi of ^{7}Be. Due to the above concerns and bureaucratic limitations, only ORNL employees were allowed to handle the ^{7}Be during the chemical preparation.

The necessary equipment for the ^{7}Be chemistry consists of 3 pipettors (clean acid, clean base, sample), 25 mL and 10 mL pipettes, 2 small beakers, 10 mL Teflon test tubes, heater block, oven, centrifuge, press, compressed nitrogen, long handled test tube tongs, personal protective equipment, silica wool, Dowex 1-X8 anion-exchange resin, column for resin, distilled water, 10 N HCl, NH_4OH, $FeCl_2$, 150 mesh Cu (or other suitable) powder, Cu cathode molds and a die and rod for pressing (made of tool steel). During the process, the ^{7}Be was monitored by placing a hand-held meter to the outside glass of the fume hood. An outline of the procedure for isolating the Be is as follows:

1. Preparation: Fill column with 1 cm of silica wool followed by 3 cm of resin. Flush

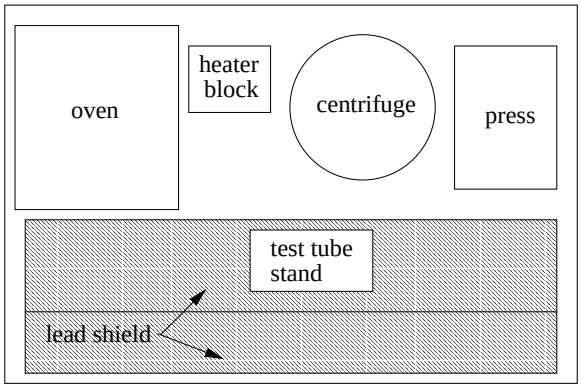

Figure 2.9: ^{7}Be chemistry fume hood setup.

column 3 times with water. Keep resin covered with water until ready to use. When ready, drain water and flush at least 3 times with 10 Normal HCl, to prime the resin. Fill cathode molds with Cu powder, leaving 0.5 mm head space.

2. Dissolve Li/Be: Place ingot in a beaker. Add $\geq$ 100 mL water and cover with an inverted funnel to prevent ^{7}Be from escaping, while allowing CO_2 to escape. Allow the Li/Be to dissolve. Remove the Cu disk and check it for activity.

3. Prepare Ph: Transfer the solution to a large test tube appropriate for the centrifuge and add a small amount of $FeCl_2$ to the liquid. This iron powder will act as a carrier and tracer for the Be during the purification process. Add HCl and stir until all $FeCl_2$ is dissolved; pH should be ≈ 1. Add base until $Fe(OH)_2$ precipitates out of solution.

4. Centrifuge: Place solution filled test tube in centrifuge, along with a ballast tube filled with slightly more water. Centrifuge until $Fe(OH)_2$ collects at the bottom of the tube (along with the invisible $Be(OH)_2$), and the liquid above is clear. If this does not happen, add more NH_4OH. Draw off Li laden liquid into a waste container. Monitor the activity in the waste container to insure that ^{7}Be is not drawn off. Usually 0.5 to 1% of the activity is lost during this step. Wash tube, centrifuge and draw off liquid. Add HCL to fully dissolve the $FeCl_2$, transfer to a smaller centrifuge tube and repeat step 4. The goal is to remove as much liquid and Li as possible without removing ^{7}Be.

5. Wash: Add water to to test tube and stir contents. Centrifuge and then draw off the clear liquid on top. Repeat this procedure.

6. Dry in heating block at 80°C, under air flow. Dissolve the Be/Fe residue in a small amount of HCl and add to the column. Flush this solution through the column with as little HCL as possible, into a small teflon test tube. The resin will become discolored as the Fe lodges in the column. When the drops of liquid exiting the column contain minimal activity, stop the flow. Place a waste container under the column and discharge the column by flushing it with water.

7. Dry ^{7}Be : Place test tube in heating block. Set the heater block to 80°C and flow just enough Nitrogen gas over the surface of the liquid to disturb the meniscus. After the liquid has evaporated, wash the sides of the test tube by rolling a few drops of HCL down the wall of the tube and dissolving the ^{7}Be.

8. Make Cathode: Dissolve ^{7}Be in a few drops of HCL and transfer those drops 1 at a time onto the cathode mold. If liquid had filled the mold, dry cathode in a 70°C oven, until liquid evaporates. Once all drops are in cathode, dry for 24 hours at 200°C to fully oxidize the ^{7}Be. After allowing to cool, sprinkle a small amount of Cu (or other) powder in mold and press at 100 N.

2.2.3 ^{7}Be ion source

A multi-sample Cs sputter source was designed by ORNL's source development team. It is similar in design to the "batch mode" sputter source that was already in use at the HRIBF [Alt93, Alt94], and is shown in Fig. 2.10. In the source, an oven first vaporizes a reservoir of Cs metal. That Cs vapor is positively ionized by the hot ionizer, and the ions are accelerated by a 4.5 kV potential to the cathode. Negative atomic and molecular ions are sputtered from the surface of the cathode and accelerated by an extractor electrode out of the source. As shown in Fig. 2.10 (left), the source can hold up to 8 sputter cathodes. However, if more than 4 are loaded at a time, the ion optics are changed, and the source performance is degraded. Therefore, a maximum of 4 cathodes were

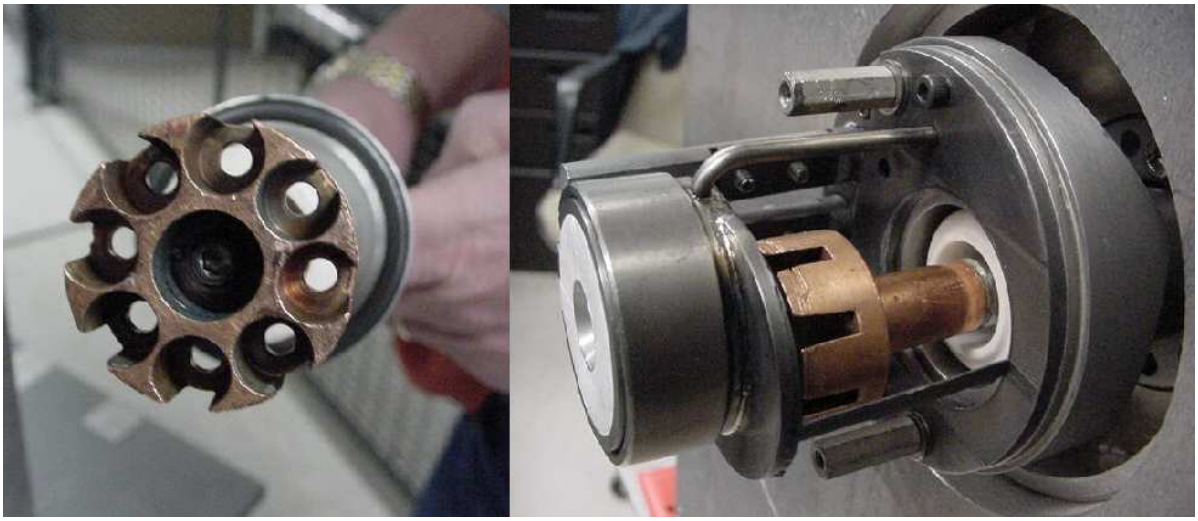

Figure 2.10: Picture of the ^{7}Be multi-sample Cs sputter source. The 8-sample target wheel is shown on the left. The right photo shows the wheel assembled. The conical ionizer is behind the ceramic insulator in front.

loaded at a given time. The source also features a conical ionizer which is typically run at current of 27 A. The target wheel bias supply has a 5 kV maximum voltage. The source output was found to increase with wheel bias up to the 5 kV limit, and thus was usually run between 4 and 5 kV. The source parameters for normal operation are listed in Table 2.2. Although the ionizer and wheel voltage are generally left constant, the Cs oven temperature was be adjusted to optimize the source output. If the temperature is too low, then the Cs sputter current will decrease, as will the surface layer of Cs on the sputter cathode. However, if the oven is left on too long, Cs will build up on cool surfaces in the source housing, and can cause electrical shorts across isolators. Also, if the Cs density is low, the wheel voltage, and thus Cs current, can be lowered to recover some of the lost beam current while the density is being increased.

The ^{7}Be sputter source was tested with Ag, Cu, Nb and W powders as the matrix into which the ^{7}Be was mixed. Cathodes containing ^{7}Be and each powder were mounted in the source and tested at ORNL's offline testing facility (OLTF). There was no significant difference in the sputtering rate among the Cu, Nb and W. Initial tests showed a factor of 4 higher total sputter rate for Ag than the other powders. However, a subsequent test showed that Cu and Ag cathodes sputter at the same rate. Since Ag never performed worse than Cu, it was used for the final ^{7}Be cathode for $^1\mathrm{H}(^7\mathrm{Be},\gamma)^8\mathrm{B}$.

parameter	value
Wheel Bias	4.5 kV (0.3-0.6 mA)
Cs oven	160° C
Ionizer	27 Amps
Extractor	14 kV
Acceleration	40 kV

Table 2.2: Typical operating parameters for the ^{7}Be sputter source.

The cathode wheel from the March 2005 ^{1}H(^{7}Be, γ)^{8}B experiment is shown in Fig. 2.11 (right). The 126 mCi ^{7}Be cathode was mounted in the upper-left position. During a portion of the run, the cathode was rotated off axis to sputter fresh material, so an elongated sputter pattern is visible. After 11 days of sputtering on that cathode (5 of which were for the ^{1}H(^{7}Be, γ)^{8}B measurement), 50% of the ^{7}Be remained in the source, around the edges of the cathode. Either recycling the extra material, or further decreasing the diameter of the ^{7}Be region to match the sputter pattern would increase the total source output in the future.

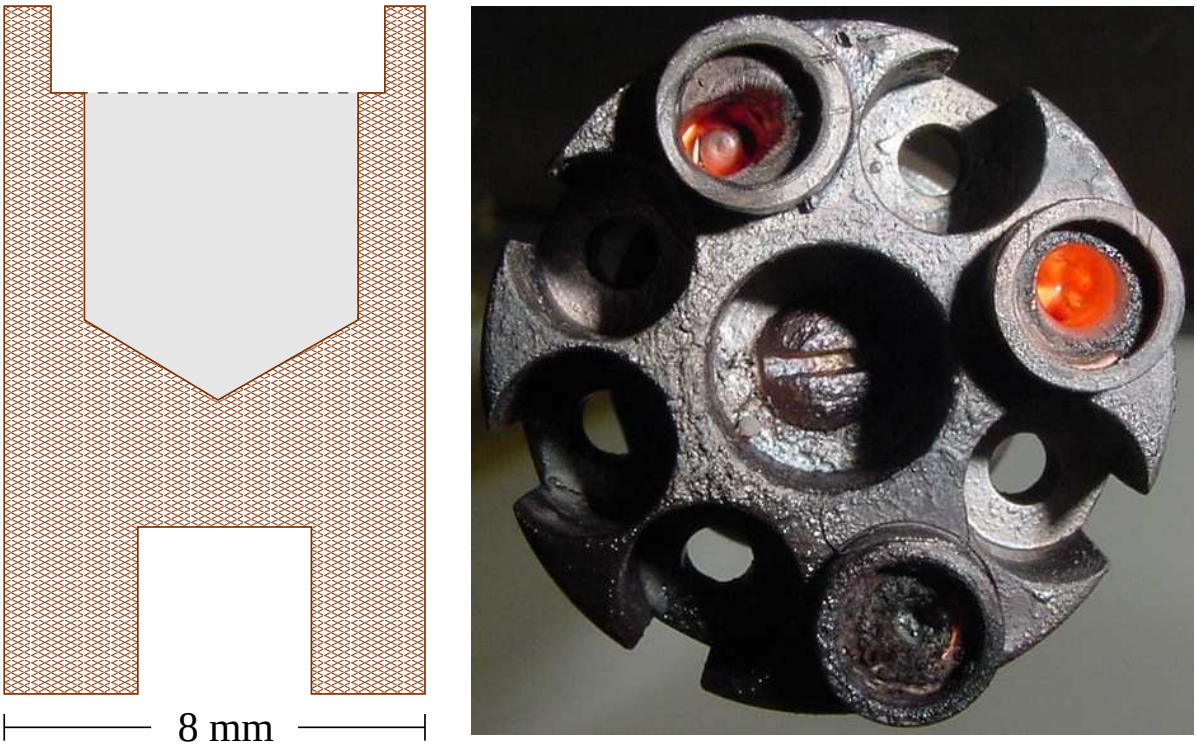

Figure 2.11: Scale cross-sectional view of a ^{7}Be cathode (left). The Cu mold (brown) and Ag+Be matrix (grey) are shown. The bottom hole is for mounting in the target wheel. Photograph of the sputtered cathodes (right). The top left position held a ^{7}Be cathode (see text).

2.3 Windowless hydrogen gas target

2.3.1 Target description

A differentially pumped windowless gas target (WGT) was designed for use in proton capture experiments at ORNL. It is similar in design to the one used by the NABONA collaboration [Str96]. The present version is more compact and runs at a higher central pressure than the NABONA target [Ter01]. The windowless design reduces the beam and recoil straggling as well as the possibility of γ-ray background contamination caused by foil windows. Furthermore, the circulating gas maintains a constant target density and composition. This is in contrast to plastic or metal targets that can have uncertain stoichiometries and thicknesses, which can change during the course of an experiment. The target was designed to allow maximum pressure in the central target area (5-6 Torr) while maintaining high vacuum on either end of the the target, as required by the accelerator and the DRS. High vacuum downstream is also important to preserve the charge-state distribution of the recoils from the exit of the gas target to the focal plane detector. The resulting pressure drop amounts to a factor of 10^5 over a distance of 0.5 meters. The center of the target consists of a 14 cm long disk-shaped chamber (Fig. 2.12). The disk-shaped geometry of this chamber allows for the use of highly collimated Si monitor detectors at $\pm 30°$, $\pm 45°$, $+60°$, and $-75°$, where "$\pm$" refers to top and bottom forward angles (see Fig. 2.12) . Also, ports are available at back angles for the gas input and pressure and temperature diagnostics. The flat sides of the disk were designed to allow close coupling of γ-ray detectors to the target. There is no pumping directly on the central disk, but it is coupled to a series of pumping stages by 5 cm long brass apertures. As shown in Fig. 2.15, each cubical pumping station is bisected, such that there are 4 pumping stages upstream and 4 downstream of the disk. The necessary pressure gradients are established by choosing appropriate diameters for the apertures between the stages. Most of the gas is pumped away by the 2 pairs of roots blowers abutting the upstream and downstream ends of the target, pumping stages 1u and 1d respectively. Then high vacuum is achieved through the later turbopump stages. The

4u	3u	2u	1u	0	1d	2d	3d	4d
$1{\cdot}10^{-6}$	$1{\cdot}10^{-6}$	$2{\cdot}10^{-6}$	$5{\cdot}10^{-6}$	$< 4 \cdot 10^{-4}$	$1{\cdot}10^{-5}$	$5{\cdot}10^{-6}$	$1{\cdot}10^{-6}$	$1{\cdot}10^{-6}$
$6{\cdot}10^{-6}$	$1{\cdot}10^{-5}$	$3{\cdot}10^{-5}$	$8{\cdot}10^{-5}$	5.00	$3{\cdot}10^{-1}$	$1{\cdot}10^{-2}$	$4{\cdot}10^{-4}$	$2{\cdot}10^{-4}$

Table 2.3: Typical operational pressures (Torr) for the gas target.

first downstream aperture, A_{1d}, has to be larger than its upstream counterpart, A_{1u}, in order to accept the cone of recoils. Thus, there must be more pumping downstream, and the limiting factor for the pressure P_o is the load on the turbopump on chamber 2d. That turbo was backed by an upstream roots blower stack. All of the backing pumps were vented to an exhaust line which terminated with a blower to the outdoors. The WGT was run with 99.99% pure H_2 gas. Typical operational pressures are listed in Table 2.3.

Many factors were considered when designing the aperture diameters and shapes. In general, they should be as constrictive as possible to allow a steep pressure gradient at each pumping stage. An upper limit for the flow through an aperture of inner radius, r, and length, L, caused by a pressure change ΔP is given in the laminar flow limit [Fab95], by

$$Flow \ \propto \ \frac{\Delta P \, r^4}{L}. \tag{2.5}$$

Thus, small reductions in the aperture diameters drastically reduce the flow, and thus increase the pressure gradient across the aperture. Maximizing the pressure gradient then maximizes the P_o that can be run without overloading the pumping system, which directly increases the (p, γ) count rate during an experiment. Also, a sharp pressure gradient localizes the target, and thus the source of recoils, in space. This feature is a factor in the transmission efficiency of the recoils through the DRS. The longer the target, the bigger the range of focal lengths that the separator has to transmit to and focus at the focal plane. In practice, θ_r is so small, that the DRS transmission and focusing are not major issues. However, if a significant amount of gas is upstream of A_{1u}, then recoils made there could be lost in aperture A_{1d}. A Monte-Carlo simulation

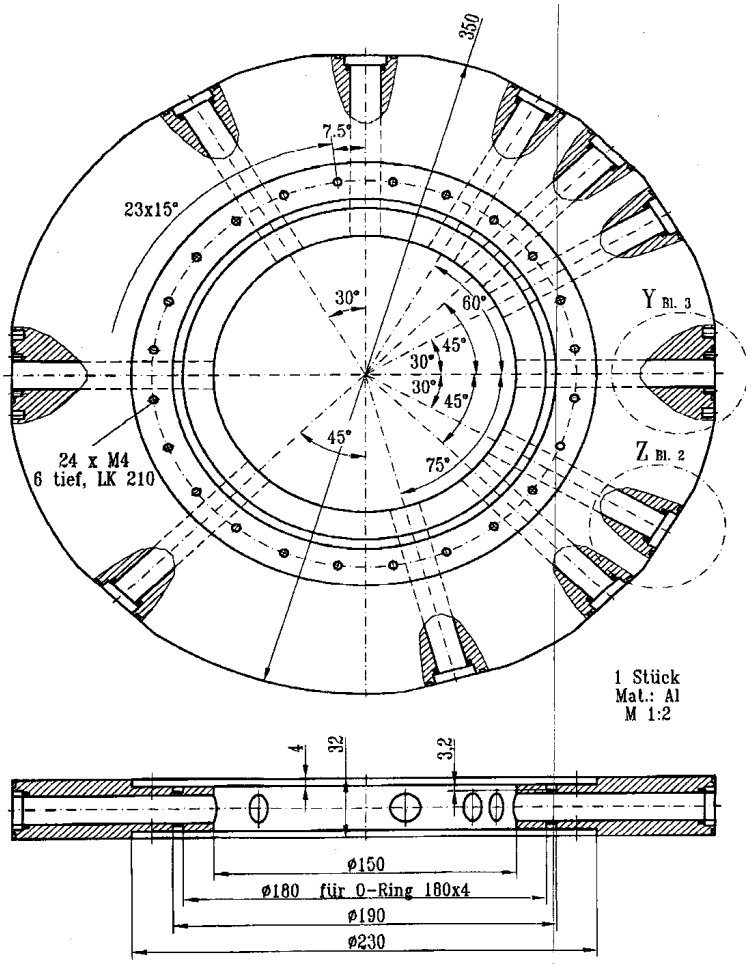

Figure 2.12: Central disk of the WGT. Beam enters from left.

of this effect has shown that <0.1% of the ^{8}B recoils are lost in this way (see Sec. 2.3.5).

Also, the inner diameter of A_{1u} needs to be big enough to transmit the beam. Typically, the beam spot was a few mm in diameter and for $A_{1u} = 3$ mm, the beam transmission through the WGT was 80-90%. In order to ensure precise alignment, the aperture A_{1u} was made to have a diameter of 3 mm for the first 6.4 mm of length and then enlarged to 5 mm for the remaining 45 mm (Fig. 2.14). The short, beam defining end of the aperture was aligned to 0.2 mm accuracy, but the larger end could be off-axis by < 1 mm without affecting transmission. Furthermore, this design minimized scatter from the aperture. This design also took advantage of the weak dependence of the gas flow on aperture length (as seen in Eqn. 2.5). The 5 mm diameter section was threaded to encourage turbulence, which could reduce the flow of gas through the aperture. The

Aperture	A_{5u}	A_{4u}	A_{3u}	A_{2u}	A_{1u}	A_{1d}	A_{2d}	A_{3d}	A_{4d}	A_{5u}
Diameter	5	5	5	4	3*	6*	11	13	15	17
Length	40	40	60	60	50	50	60	60	40	40
Separation	—	31	33	75	138	75	34	23	23	38

Table 2.4: Diameter, length and separation between apertures. Separation measured end-to-end, starting upstream of the WGT. All measurements in mm. *see Fig. 2.14

apertures further upstream had inner diameters greater than 3 mm, which maximized their induced pressure gradients, while ensuring that A_{1u} remained the beam-defining aperture.

Downstream of the gas target, the apertures have to be large enough to admit the recoils that scatter from any point in the target at scattering angles up to θ_r. Therefore, the beam has to be constrained such that there is θ_r clearance between the most errant beam particle within the target and the downstream apertures. To this end, a 5 mm "tuning" aperture was inserted downstream of A_{5d}. As illustrated in Fig. 2.13, the tuning aperture restricts the beam divergence and convergence to be 0.16° and 0.29° respectively. With the tuning aperture removed, the acceptance of a recoil produced at the upstream end of the gas target, on the edge of aperture A_{1u}, from maximally divergent and convergent beams, are 0.57° and 0.92° respectively. Therefore, the net angular range of acceptance for recoils produced at the upstream end of the gas target, from a maximally divergent and convergent beam is 0.41° and 0.63° respectively. The first downstream aperture, A_{1d} was 6 mm in diameter over a length of 6.4 mm length and then tapered out to 8 mm diameter. This was done again to facilitate precise alignment. The final aperture diameters and distances between them are listed in Table 2.4.

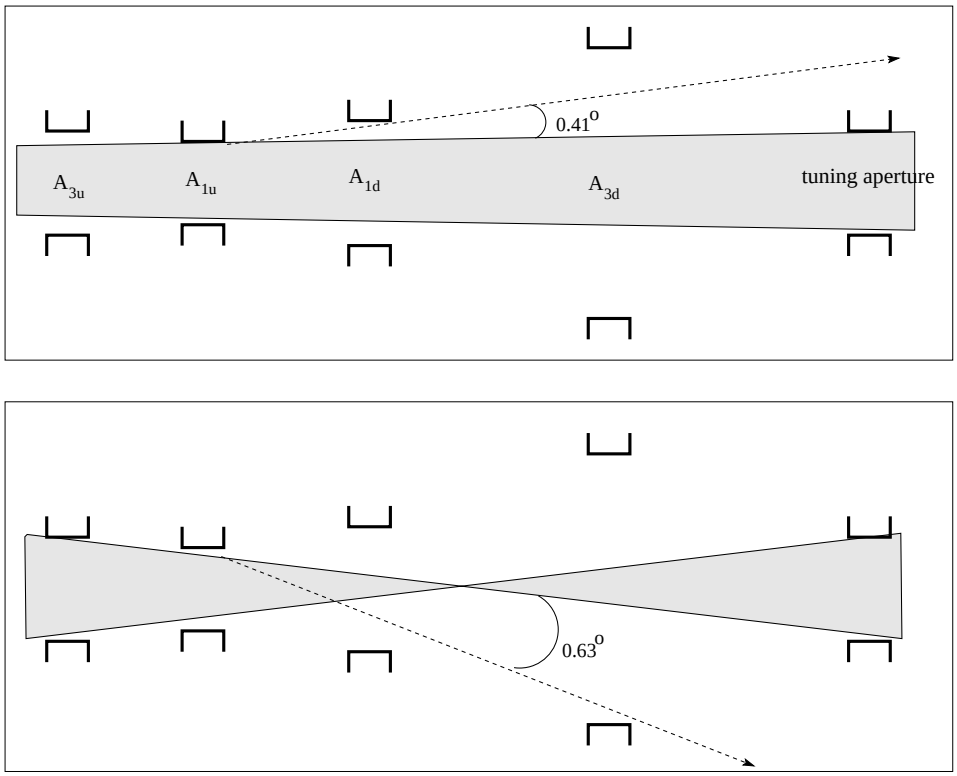

Figure 2.13: Beam optics through WGT. The optically important apertures are shown. The shaded areas represent the maximum possible divergence (Top) and convergence (Bottom) of the beam as it passes through all the apertures, including the tuning aperture. In each scenario, the maximum allowable recoil angle that will be transmitted through the gas target, with the tuning aperture removed, is shown (see text). The aspect ratio has been decreased for clarity.

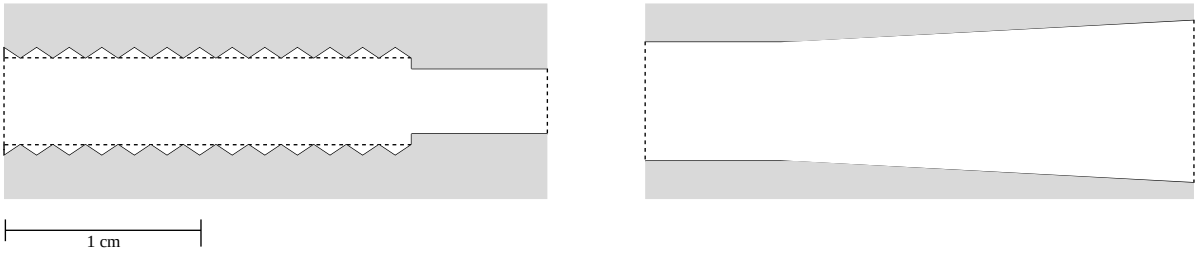

Figure 2.14: Scale drawings of A_{1u} (left) and A_{1d} (right). Beam comes from the left. A_{1u} is threaded to encourage turbulence and A_{1d} is tapered to admit recoils and facilitate alignment (see text).

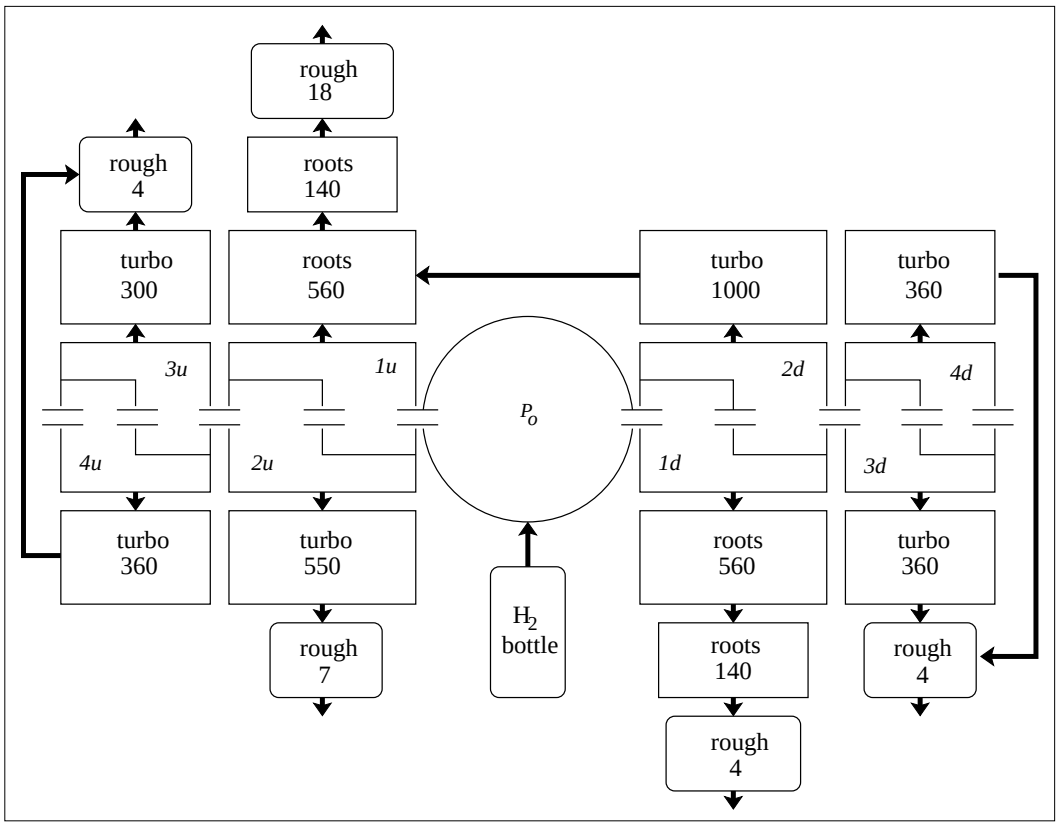

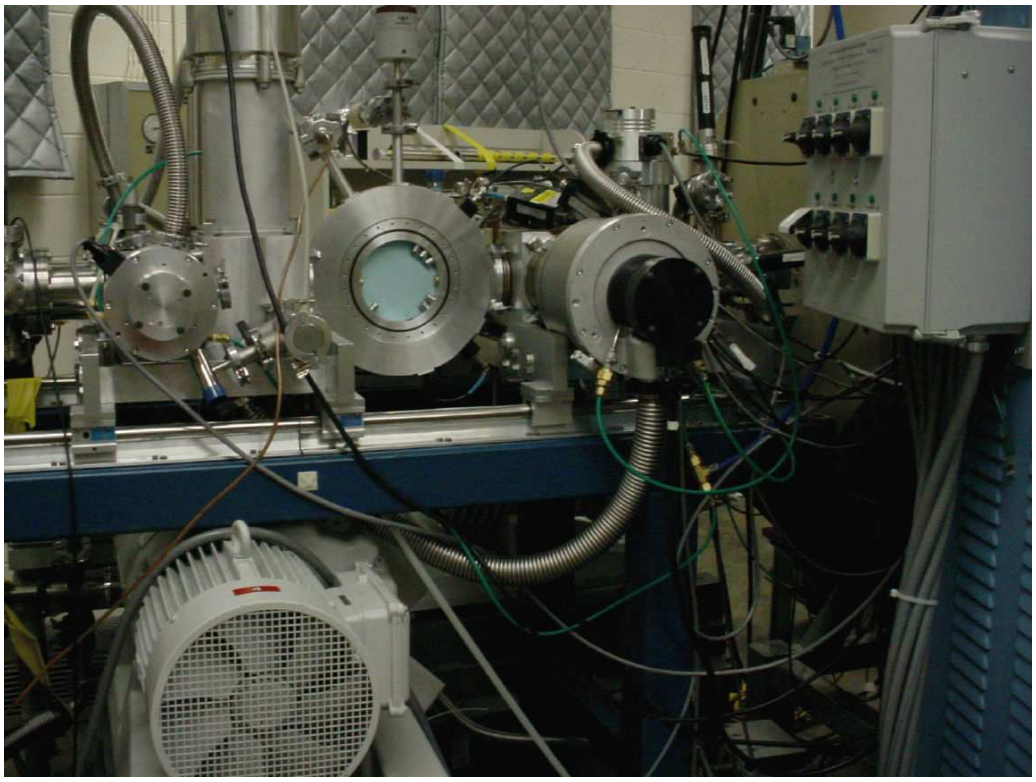

Figure 2.15: Top: Schematic of the WGT pumping, apertures labeled as Table 2.4. The pumping speeds are indicated in liters/second. Bottom: Photograph of the WGT with the front panel of the disk removed. Beam comes from the left.

2.3.2 Hydrogen safety

Hydrogen is a flammable gas and is explosive in air when mixed in concentrations between 4% and 75% at STP. A 4% concentration is thus the lower explosive limit (LEL). No concentration of hydrogen is flammable at pressures below 0.3 atm. Precautions were taken to control all of the H_2 used in the WGT and to discharge it safely. To this end, safety procedures and hardware interlocks were put in place.

The hydrogen safety interlock system is shown in Fig. 2.16. It is a multiply redundant system for ensuring the integrity of the WGT and the safety of the experimenters. The source of hydrogen to the system is the single, 7,000-L H_2 cylinder that is present in the DRS room during operation. It is fitted with a Victor VTS452 dual-stage, hydrogen/methane regulator. The regulator is equipped with a relief valve which is plumbed to the common exhaust line. If the first regulator stage fails, the relief valve will open. The regulator output is connected through Swagelok flexible tubing (limit 3,000 PSI) to a manifold block. At the manifold, it passes through a Quantum FS190SFP excess flow valve, which is a redundant safety device. If the flow exceeds 50 slpm, this valve is closed by a spring. The manifold is connected with Cu line to a Swagelok SS-4BK-TW-2M-3C normally-closed interlock valve that is opened pneumatically when all subsequent interlock conditions are met. The interlock valve is followed by a Brooks MT 3750C Ar-Mite^{TM} Low Flow Armored Flowmeter. This meter indicates the flow of H_2 to the WGT and is equipped with a mechanical, relay-activating, adjustable setpoint. This was set at 10 slpm H_2, which corresponds to about $P_o = 6.0$ Torr under normal operating conditions. For the factory-set flow calibration to be correct, the inlet pressure (second regulator stage) must be set at 10 PSI. Next in line is a flash arrester, which is designed to stop a fireball or pressure burst created downstream and traveling up toward the gas bottle. This is followed by a needle valve, which is used to control the central pressure in the gas target. For a given needle valve setting, P_o will remain constant to better than 0.002 Torr as long as the H_2 tank pressure is $\gg$ the 10 PSI in the secondary. In practice, the pressure is constant until the tank drops below about 5% of its maximum pressure. A Cu line runs from the needle valve to a port on the central disk of the gas

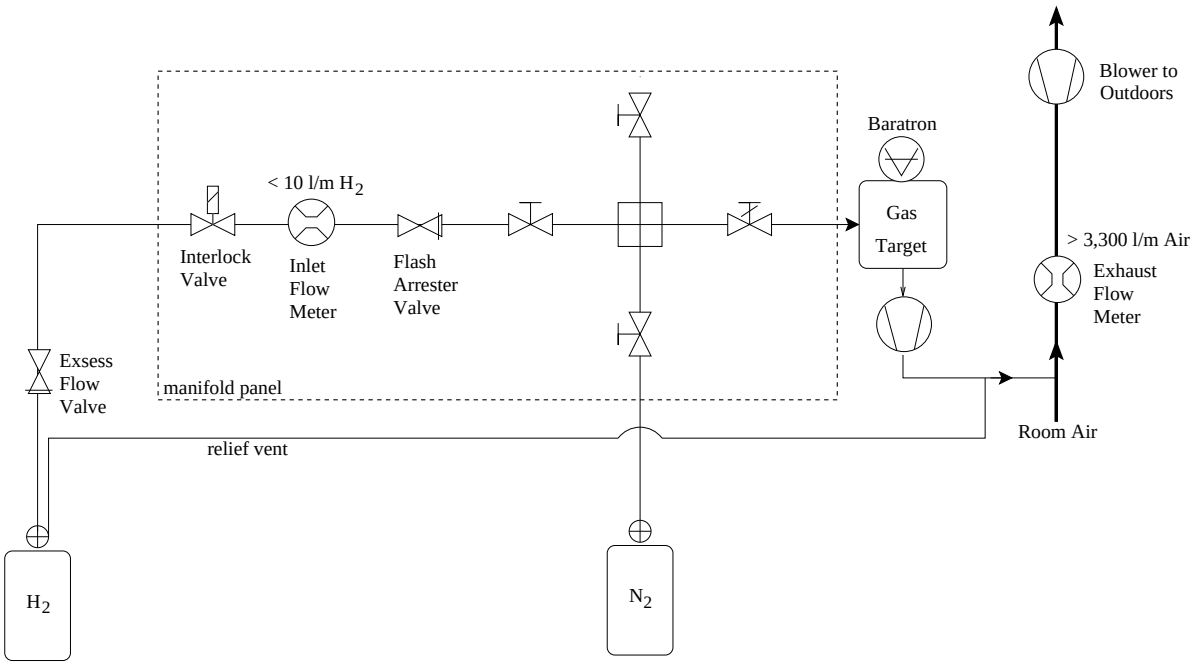

Figure 2.16: Schematic of hydrogen gas handling system at HRIBF.

target.

The exhaust from all the roughing pumps, and the regulator relief valve are teed to a QF-40 tube inserted into a single 15 cm diameter Al exhaust line and vented to the outside. This line is pulled by an exhaust pump mounted outdoors. The air flow in this line is monitored by a Flowline GT10 flow switch, armed with a relay and set at > 3.1 m/s, or 3,300 slpm. Since the H_2 flow is limited to 10 slpm, the setpoint corresponds to 13 times less than the LEL. Furthermore, the actual flow in the exhaust line was measured to be 7,500 slpm. Therefore, the exhausted H_2 passes through the explosive limit range quickly as it enters the exhaust line. Also, since the hydrogen flow into the target is limited to 10 slpm, the gas mixture in the exhaust line contains less than 0.002% hydrogen, or 0.2% of the LEL as it is ejected to the outdoors.

The pressure in the central disk of the gas target (P_o) was monitored with an MKS Absolute Capacitance Manometer baratron pressure gauge, equipped with a PDR2000 digital readout and relay. This relay was activated by a setpoint requiring $P_o < 10$ Torr. Thus, in the event of a vacuum breach in the chamber, the flow of hydrogen would be stopped.

To provide further redundancy, a Bacharach EIT Gas Sentinel Area Monitor with multiple relays was installed directly overhead of the gas target. This would detect a leak in the system and was wired to the interlock valve as well as two separate alarms. The first setpoint was set at 5% LEL and was used to close the interlock valve and to sound a buzzer in the counting room and control room. A second setpoint was set at 50% LEL and designed to sound another alarm and activate an evacuation beacon. However, if a leak developed in the gas target, air would be drawn in to the system. Therefore, the overhead monitor would be most likely to detect a leak from the cylinder or exhaust system.

An interlock box was constructed to incorporate the relays from the flow meter, baratron, exhaust flow switch, and room H_2 monitor. These were connected in series to the NC interlock valve solenoid. The interlock is latching, and must be manually reset in the event of a trip. Also, the box is fitted with red and green LED's to indicate the status of the valve and relays.

Finally, procedures were put in place to prevent accidents and respond to alarms and interlock trips. A training module was designed and administered by the gas target custodian, and an instruction manual was written outlining operation of the gas target and response to alarms. One of the most important procedures, is to use a hand-held flammable gas detector to check the initial connections when changing H_2 bottles, as leaks would be most likely to develop during cylinder changes. The most significant procedural information concerns responses to alarms. If the 5% LEL buzzer sounds, the operator should manually close the valve on the hydrogen cylinder, and monitor the H_2 level from the remote readout, outside the room. If the 50% LEL alarm sounds, all present should evacuate the building.

2.3.3 Pressure and temperature

Accurate determination of the pressure and temperature of the H_2 gas in the central chamber of the gas target is necessary to determine the areal target density and thus the overall normalization for proton capture experiments. As mentioned above, the pressure

was measured with a MKS 10 Torr full-scale Absolute Capacitance Manometer, mounted on a 10 cm long tube off the 90° port of the WGT (Fig. 2.12). The gauge is rated to 1 mTorr accuracy. The zero offset was adjusted by checking that the central pressure was <0.4 mTorr with a cold cathode gauge and then adjusting the digital readout to 0.000 Torr, as instructed by the manual. As an absolute pressure check, a Varian Ceramicel 100 Torr full-scale pressure gauge was mounted on the chamber, simultaneously with the MKS gauge. The Varian gauge was rated to better than 1% at 10 Torr, but only read out to 2 decimal places. Both gauges scaled the same with increased pressure and agreed to the accuracy displayed at 5.00 Torr. Due to the limited precision of the Varian output, this set a limit of 0.1% on the accuracy of the pressure reading. The pressure was also checked closer to the location where the beam interacts with the gas. A hole was drilled in the center of the flat plate on the side of the WGT. The Varian gauge was mounted there, and the gas target was run at various pressures. Again, the Varian gauge reading agreed with that of the baratron, mounted on the 90° port [Bla04, Dom04].

The temperature was measured using a thermocouple pressed against the central disk. The accuracy of this reading depends, firstly, on whether or not the temperature of the gas comes into equilibrium with the walls of the target disk. In fact, the gas does reach equilibrium owing to the slow flow of gas and slim design of the the central disk, which has a high surface-to-volume ratio (see Fig. 2.12). Quantitatively, the mean speed of an H_2 molecule in the target can be estimated by the Maxwell distribution as [Roh94],

$$\langle v \rangle \;=\; \sqrt{\frac{8\,k\,T}{\pi\,m}} \;=\; 1,780\,m/s, \tag{2.6}$$

where the Boltzmann constant is $\mathrm{k} = 1.38{\cdot}10^{-23}$ kg·m^2/s^2, the H_2 mass is $\mathrm{m} = 3.34{\cdot}10^{-27}$ kg and the temperature is $T = 301\,\mathrm{K}$ (21 °C). The path length of an H_2 molecule in the central chamber of the WGT is given by [Roh94],

$$\lambda \;\approx\; \frac{k\,T}{\sqrt{2}\,\pi\,d^2\,P_o} \;=\; 2.5\cdot 10^{-5}\;m, \tag{2.7}$$

where d is the size of the H_2 molecule (taken to be $2.35\cdot 10^{-10}$ m) and P is the pressure in Pa (5.00 Torr = 666 Pa). Thus, the mean time between collisions is given by,

$$\tau \;=\; \frac{\lambda}{\langle v \rangle} \;=\; 1.4 \cdot 10^{-8}\; sec, \tag{2.8}$$

Now consider that the volume of the disk is $3.5 \cdot 10^{-4}$ m^3, which at 5.0 Torr (666 Pa) is equivalent to $2.3 \cdot 10^{-6}$ scm (standard cubic meters) of gas. Furthermore, the typical flow rate of H_2 through the system is at most 10 slm = $1.6 \cdot 10^{-4}$ scms (standard cubic meters per second). Therefore, the lifetime of the gas in the disk is approximated by,

$$\tau_{disk} \;=\; \frac{disk\ volume}{flow\ rate} \;=\; 1.4 \cdot 10^{-3}\, sec \;=\; 14\ ms. \tag{2.9}$$

That is, a typical molecule spends 14 ms in the disk, during which time it undergoes 10^5 collisions and travels 2.5 m around in the small volume of the central disk. Therefore it is reasonable to conclude that the gas reaches thermal equilibrium with the walls of the chamber.

Another possible cause for a difference between the temperature of the disk and that of the target gas could be heating of the gas by the ion beam. The magnitude of this heating effect depends on both amount of beam energy lost in the target (ΔE) and the beam current. For ^{1}H(^{7}Be, γ)^{8}B, $\Delta E \leq 150$ keV and the beam current was ≤ 10 ppA. Therefore the power dissipated in the target was less than 1.5 μW. However, for experiments involving stable beams, much higher currents are typically used. In the case of $^1H(^{19}F, \alpha\gamma)^{16}O$, which was used to characterize the gas target thickness (see Sec. 2.3.4), $\Delta E = 400$ keV and the maximum beam current was $\approx$ 10 pnA. This gives a maximum power delivered to the target of 4 mW, or 0.020 mW/mm along the WGT. If heating effects are present in $^1H(^{19}F, \alpha\gamma)^{16}O$ but not ^{1}H(^{7}Be, γ)^{8}B, the areal density determined from the former will not be accurate, and cannot be used for measurements of the later. So, this effect must be explored quantitatively. From the ideal gas law,

$$\rho \;=\; \frac{P_o}{R\, T_o}, \tag{2.10}$$

(where R = 0.08206 atoms/mole), the density of the gas will decrease if the average kinetic energy of the molecules is increased. To estimate the change in kinetic energy, consider the 4 mW power deposited over a beam spot of radius r = 0.15 cm for a time

span τ (Eqn. 2.8). In this case, the average kinetic energy increase per molecule will be,

$$\Delta K.E. \approx \frac{Power\,\tau}{N\,\pi\,r^2} = 2.4 \cdot 10^{-28}\,Joules, \tag{2.11}$$

where N is the areal density of H_2 molecules$\approx 3.3{\cdot}10^{18}/\mathrm{cm}^2$. However, the average kinetic energy of a room temperature H_2 molecule is,

$$K.E. \approx \frac{1}{2}\,m < v >^2 = 5.3 \cdot 10^{-21}\,Joules. \tag{2.12}$$

Therefore, the fractional change in local temperature is roughly given by ΔK.E./K.E. $= 5{\cdot}10^{-8}$. Thus from Eqn. 2.10, the change in areal density is proportionally negligible. This effect has been explored experimentally by [Gör80]. They ran 30-300 uA of proton and ^{19}F beams through a gas target similar to the ORNL WGT. The results from proton bombardment are shown in Fig. 2.17. The lowest power point (5 mW/mm) corresponds to a $\leq 3\%$ decrease in gas density. Extrapolating the linear trend in Fig. 2.17, we expect a $< 0.012\%$ effect on the density in the WGT for 0.02 mW/mm dissipated in the $^1H(^{19}F, \alpha\gamma)^{16}O$ experiment. The small magnitude of this effect was confirmed by [Gör80] for a ^{19}F beam in their gas target by a measurement of the beam energy needed to center the $E_{cm} = 323$ keV resonance in $^1H(^{19}F, \alpha\gamma)^{16}O$ within their gas target. They repeated this measurement for 4 uA and 19 uA of beam and saw a shift of ≤ 1 keV out of the $\approx$ 33 keV energy loss in their target. Therefore, there was no significant heating effect while studying any of the reactions in this work.

2.3.4 Target thickness

The areal density, n, of the gas target was determined from the ratio of the energy loss, ΔE (eV), to the stopping power, $\epsilon(E)$ (eV$\cdot$cm^2/10^{15}atoms) of ions passing through the target,

$$n = \frac{\Delta E}{\epsilon(E)}. \tag{2.13}$$

Since there is very little stopping-power data for ions other than ^{4}He in H_2 gas, n was

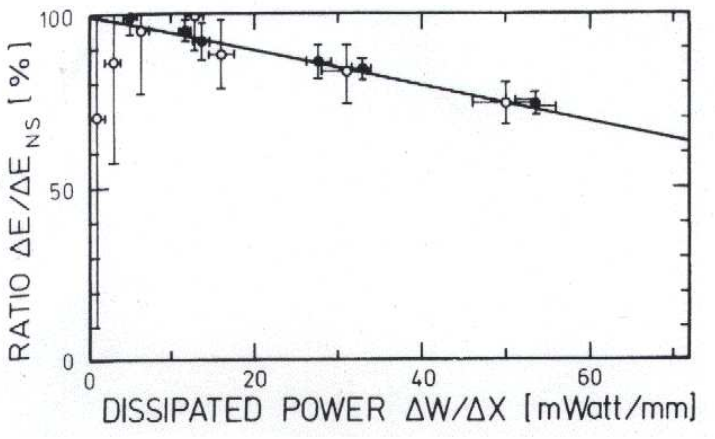

Figure 2.17: Percentage increase in energy loss due to beam heating in a gas target. Open points correspond to increasing gas pressure and closed points to increasing beam current. Plot scanned from [Gör80].

measured using ^{19}F and ^{4}He beams. Accurate measurements of the stopping power for ^{4}He in H_2 gas exist in the literature [Mar62, Rei90, Han78, Pal66]. In the case of ^{19}F, the stopping power was measured directly using the 828 keV resonance in $^{1}H(^{19}F, \alpha\gamma)^{16}O$ reaction, using a unique property of the WGT: namely, that the width of the resonance, measured as a length in the target, is much smaller than the length of the central region of the gas target (14 cm). Therefore, the position of the resonance along the central axis can be determined using a collimated γ-ray detector. The resonance parameters are listed in Table 2.5. The α_2 transition that dominates (73%) the reaction leads to a 6.13 MeV γ-ray [Til02]. The γ-rays were detected with a 7.6 cm diameter NaI detector mounted at 90° to the central disk of the WGT. The setup is shown in Fig. 2.18. The NaI was shielded with Pb and placed on an Al plate mounted on pillow-blocks. The whole setup could then be translated on rails along the beamline. The position along the axis was measured with calipers to 0.5 mm precision. A 16.6 MeV ^{19}F beam loses $\approx$400 keV in the gas target, so that the resonance width is $\Gamma \approx 1.5$ cm along the gas target. The detector was shielded by 10 cm Pb, except for a 7 mm vertical slot centered in front of the detector. The Pb was thick enough to reduce the γ-ray flux by a factor of 100. The position resolution of the collimator was measured with a small γ-ray source to be FWHM $\approx$ 1.7 cm, similar to width of the resonance in the target and three times

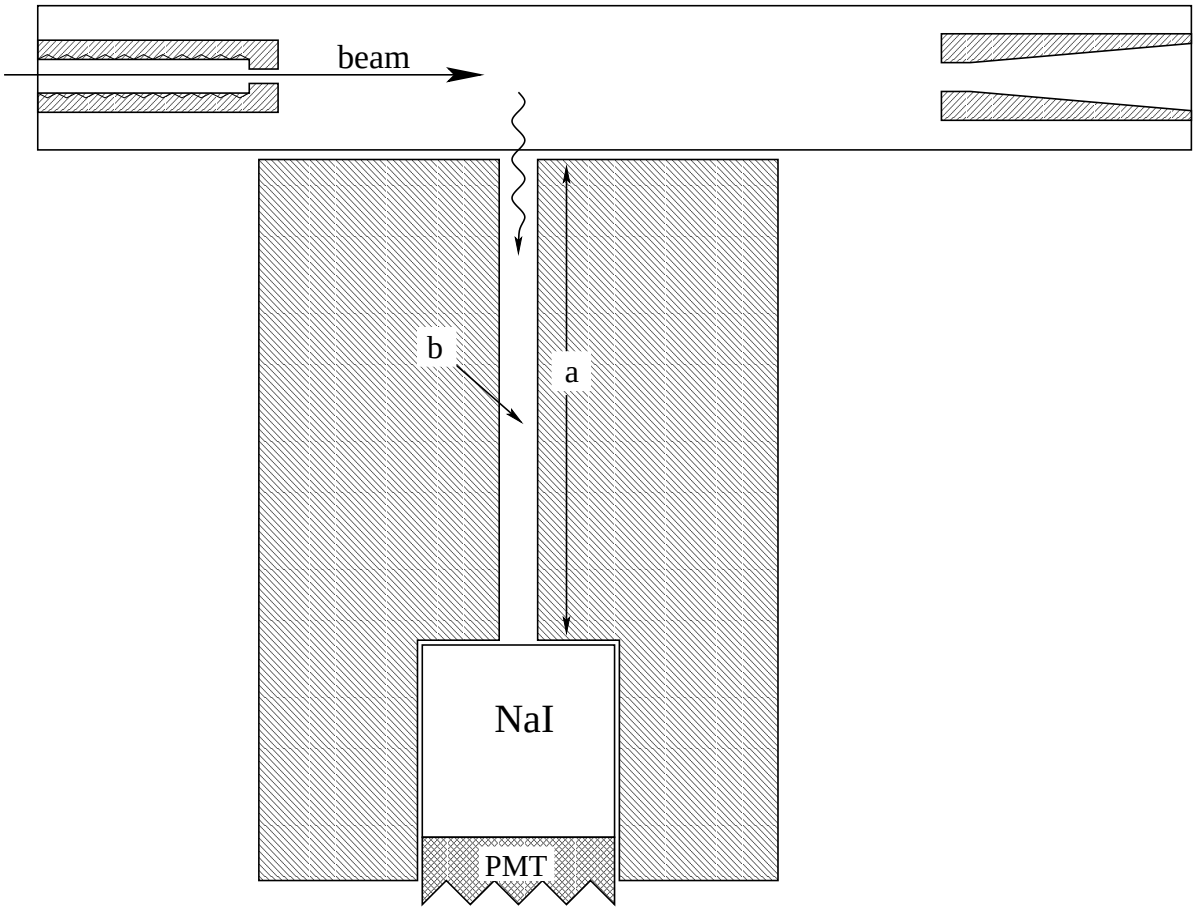

Figure 2.18: Setup for stopping power measurement. Top and bottom Pb shielding is not shown; drawn roughly to scale. a = 10 cm, b = 0.7 cm.

larger than the precision of the position measurement.

$E_{r,cm}$ (keV)	$E_{r,lab}$ (MeV)	Γ (keV)	Γ_{lab} (MeV)	ω_γ (eV)	^{16}O γ-rays (MeV)
828.2	16.6	4.3	82	785	6.13, 6.98, 7.12

Table 2.5: ^{19}F resonance parameters. α energies from [Til02], all other data from [Ang99] (see also [Spy97] for Ge spectra).

A sample NaI spectrum is shown in Fig. 2.19 along with a beam-off background run. The region of interest (ROI) was defined by a gate drawn from ≈ 3.5 - 7 MeV in the NaI spectrum. The net intensity in the ROI was determined by subtracting off a background run of equal live time taken with the beam on, but with the WGT evacuated. The beam current was monitored in two ways. First elastically-scattered protons were

counted in the 45° monitor detectors mounted in the WGT. For a given beam energy, the monitor detector rates gave accurate relative beam integration as the NaI was scanned across the target. Typically, the detector was left at a given position for 30 minutes, and then moved to a new position. However, the monitor rates cannot be used to compare yields from various beam energies, since the elastic scattering cross section varies over the energy region spanned. A rough relative measurement of the elastic scattering cross section at each beam energy was obtained in a separate measurement. Here, the beam current was integrated on an unsuppressed, retractable Al plate that was mounted directly downstream of the WGT. Simultaneously, the monitor spectra were recorded, and the ratio of the monitor detector counts to the integrated charge gave a relative measurement of the elastic scattering cross section. The relative normalization among energies does not affect the extracted value for the stopping power because only the centroid of the yield curve for each energy was required. Fig. 2.20 shows the results of this procedure for various energies at $P_o = 7.00$ Torr. These data were taken with an initial set of apertures that differed slightly from the final version. However this has no effect on the measurement of the stopping power. Each scan was fit with a curve consisting of 2 Gaussians constrained to share the same centriod. One Gaussian had a large width, to fit the γ-rays that leaked through the lead, and one with a narrow width to fit the γ-rays passing through the collimator. Each curve contained $\approx$ 10,000 counts and the fits generally had $\chi^2/\nu \approx$ 1.0. The drop in pressure at the first set of apertures can be seen in Fig. 2.20. To determine the stopping power, only data taken in the center 80% of the target were used so that the result would not be influenced by the pressure drop at the apertures. This experiment was repeated at $P_o = 5.50$ Torr with the final set of apertures. The displacement of the resonance along the central disk of the gas target for each P_o was converted to areal density using known pressure and temperature of the gas in the central disk and the ideal gas law, Eqn. 2.10.

The position vs. beam energy plot showing both the 7.00 and 5.50 Torr experiments is shown in Fig. 2.21 and its slope is adopted as the stopping power,

$$\epsilon \; = \; (56.7 \pm 2.0)\, eV \cdot cm^2/10^{15} atoms. \tag{2.14}$$

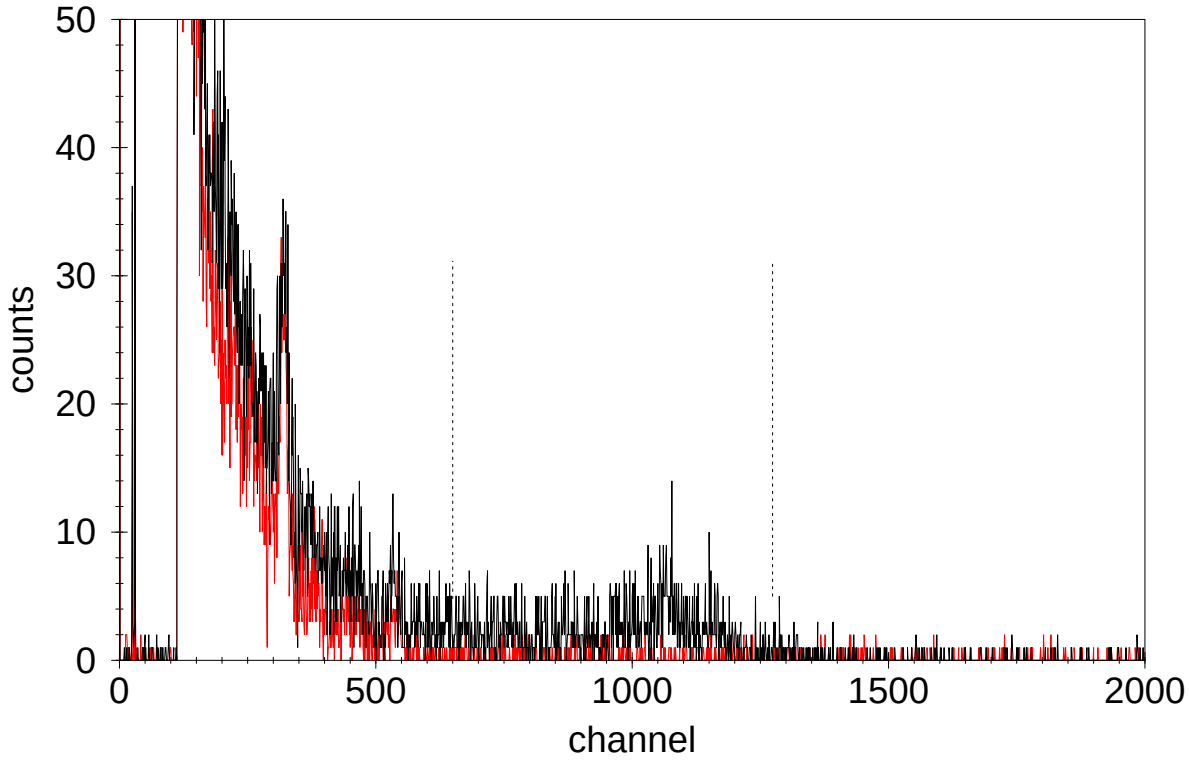

Figure 2.19: $^1H(^{19}F, \alpha\gamma)^{16}O$ spectrum (black) and background (red/grey) over a 700 second period. The gate shown by dotted line was the region of interest (ROI) for all runs.

One correction that was considered is the fact that the measured stopping power is integrated over a finite energy range. Furthermore, the slope in Fig. 2.20 averages over 0.6 MeV of beam energy. The effect of this integration was studied using stopping power models MSTAR and SRIM. The stopping power is predicted to change $< 1\%$ over an energy range from 16.4 to 17.0 MeV, so the effect is small. Also, the energy loss measurement described below is sensitive to the average stopping power in the target (average slope). Thus the effect tends to average out and the ratio in Eqn. 2.13 is insensitive to this effect to $< 0.2\%$.

Next, the total energy loss of the ^{19}F beam through the gas target was measured with a Si surface barrier detector located at $\theta_{lab} = 0°$, directly after the last pumping stage of the WGT. The beam was run into the detector while the WGT was cycled through pressures of $P_o < 0.001$ Torr, $P_o = 5.00$ Torr and $P_o = 6.00$ Torr. Since the beam energy was known to be a constant 16.45 MeV from the post-accelerator analyzing magnet,

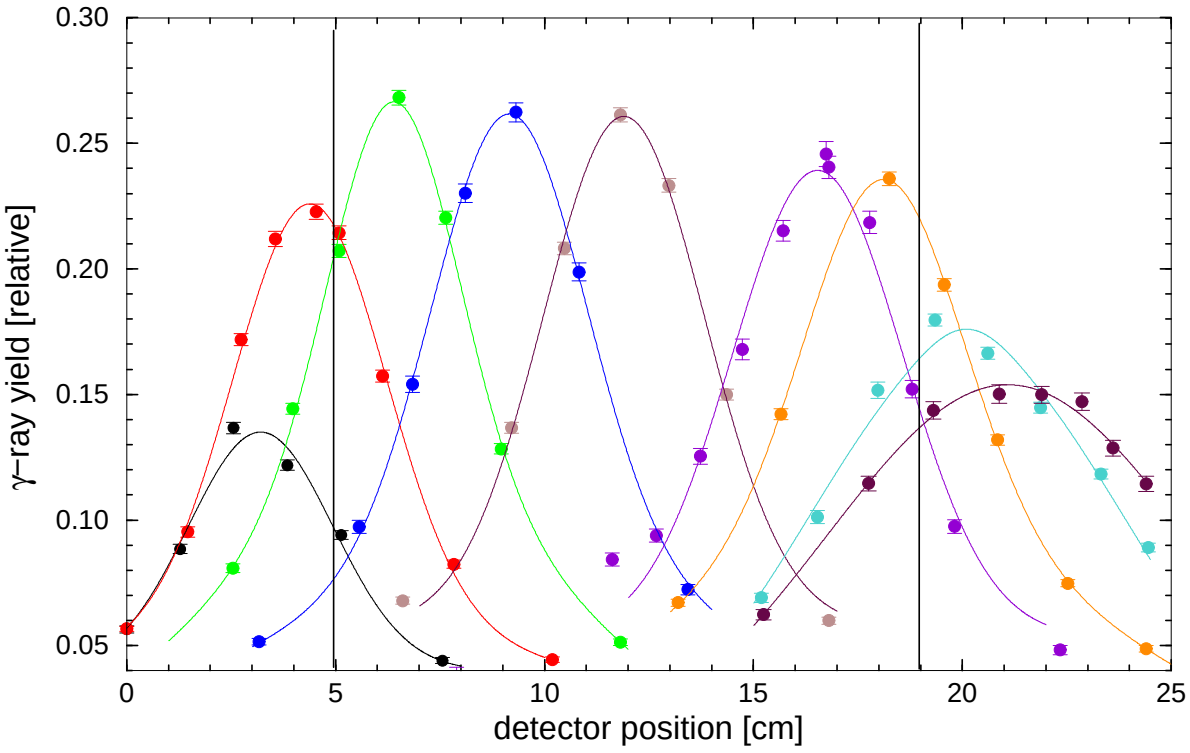

Figure 2.20: Profile of the WGT with temporary apertures. P_o = 7.00 Torr. Curves represent E = 16.45, 16.50, 16.55, 16.60, 16.70, 16.80, 16.85, 16.90 and 16.94 MeV (from left to right). Vertical lines show approximate locations of the interior ends of the innermost apertures.

the relative energy loss of the beam as it passed through the various target thicknesses could be used to determine the absolute energy loss of the beam in the gas target. Each spectrum was fit with a Gaussian curve with a low energy tail. A sample of the data is shown in Fig. 2.22, corrected only for the 13-channel ADC offset. The offset was measured by sending pulser signals of various voltages into the detector preamp. The data acquisition software output was then extrapolated to 0 volts. During the final analysis, the fractional energy loss was computed for time-adjacent gas on and gas off runs. Each cycle lasted for < 1 minute, so gain shift effects were reduced to $< 1\%$. In addition, the peaks were also analyzed by extracting their geometric centroids instead of using a fit yielding identical results to $< 0.5\%$. The energy loss in keV as a function of central pressure in Torr is given by,

$$\Delta E(P_o) \;=\; 71.65\, P_o \;-\; 0.27, \tag{2.15}$$

and is accurate to 1% over the pressure range 5-6 Torr. Therefore, using Eqn. 2.13 with

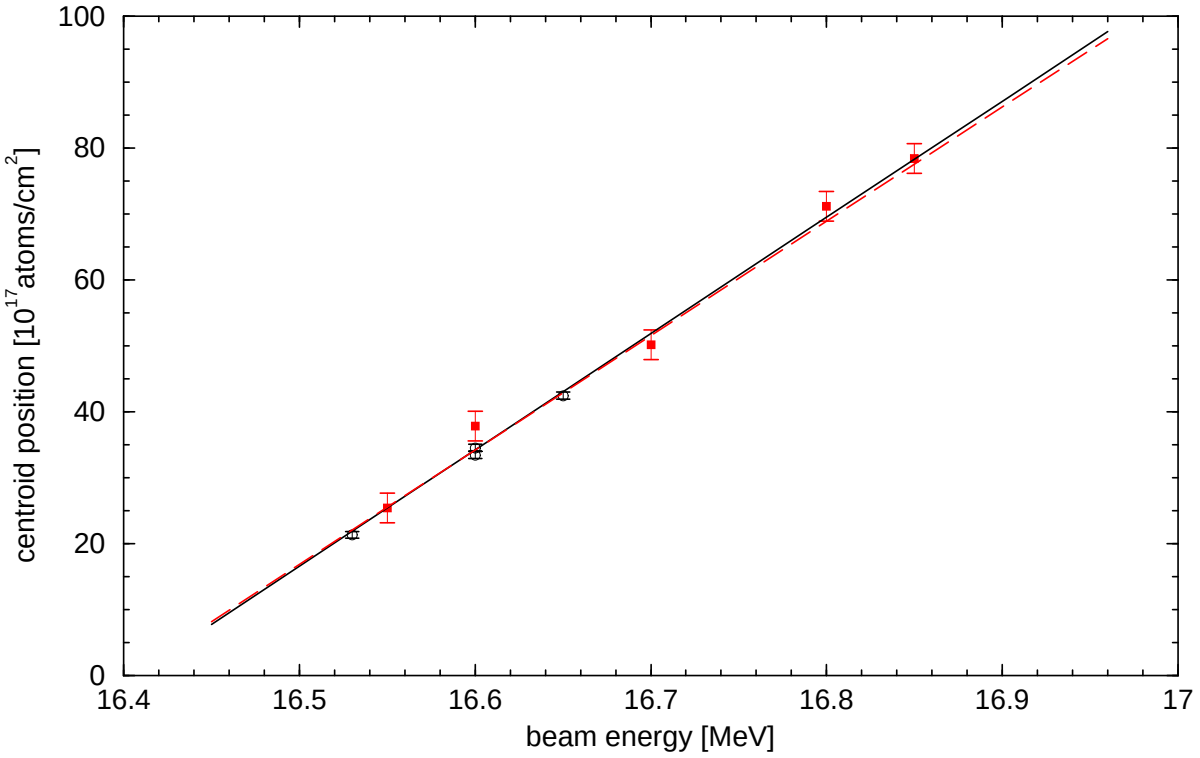

Figure 2.21: Centroid positions of $^1H(^{19}F,\alpha\gamma)^{16}O$ resonance in the WGT. Stopping power equals the slope (see text). 5.00 Torr data (open circles) give $\epsilon = (56.7 \pm 2.0)$ eV $\cdot$ cm$^2/10^{15}$atoms, and 7.00 Torr data (filled squares) give $\epsilon = (58 \pm 4)$ eV $\cdot$ cm$^2/10^{15}$atoms.

$\Delta E = 393$ keV and $\epsilon = 56.7$ eV$\cdot$cm$^2/10^{15}$, the areal density of the gas target at standard operating pressure is, $n_{5.5\,\mathrm{Torr}} = (6.93 \pm 0.25) \cdot 10^{18}$ atoms/cm^2.

A second measurement of the target thickness was made using a ^{244}Cm α-source. The source was placed in the second upstream pumping stage (2u), and a Si surface barrier detector was again placed downstream of the final gas target pumping stage. Since the pressure in section 2u of the target was only $\approx 3{\cdot}10^{-5}$ Torr, less than 0.01% of the target gas was upstream of the source. Thus, the energy loss of the alphas was due to the whole WGT. Alpha spectra were recorded with $P_o < 0.001$ Torr and $P_o = 6.00$ Torr. The gas-on/gas-off energy loss measurement process was repeated 15 times and the relative energy shift of the 5.805 MeV alpha peak determined. The uncertainty in the shift was taken to be the standard deviation of the shifts between time-adjacent gas-on/gas-off runs. The resultant energy loss for 5.805 MeV α particles passing through the

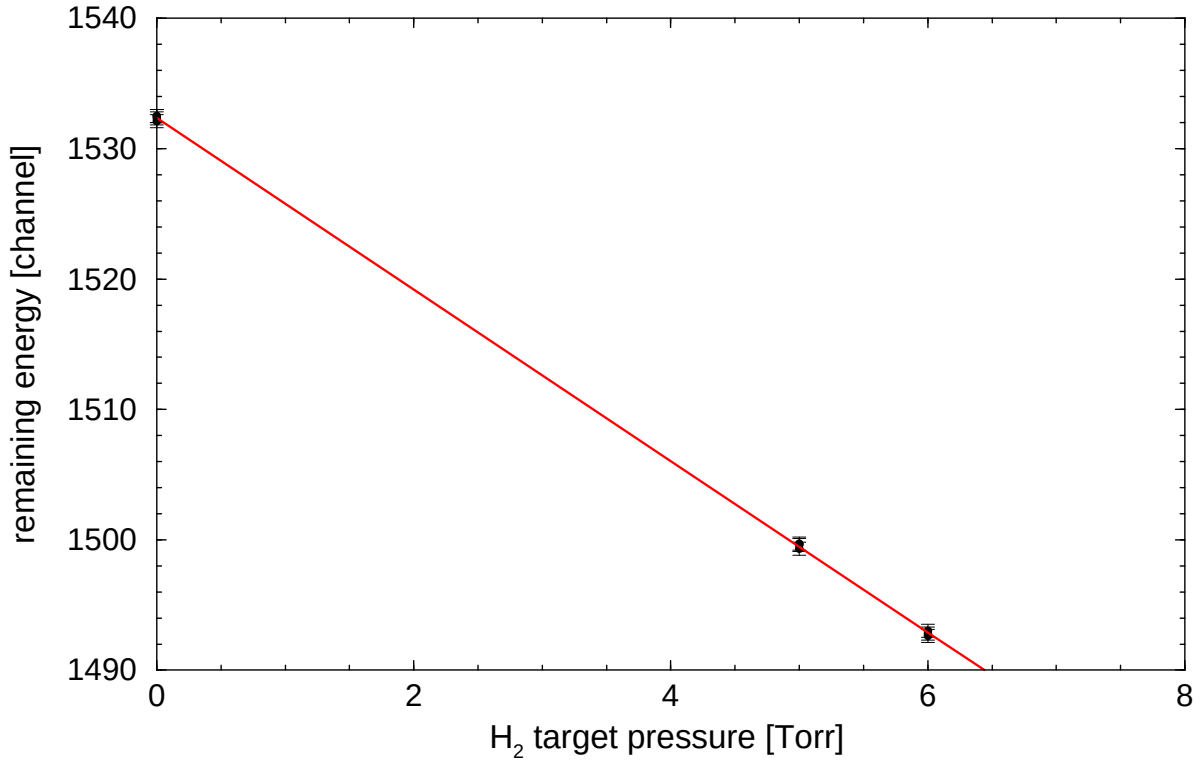

Figure 2.22: Energy loss of E = 16.65 MeV ^{19}F in the WGT. Shown are raw centroid positions corrected for ADC offset. The linear fit is channel = -6.581·P + 1532.38. This gives $\Delta E_{5.5\,\mathrm{Torr}}$ = (393± 2)keV.

gas target with $P_o = 6.00$ was (25.8 ± 0.8) keV. This scales to $\Delta E = (23.7 \pm 0.9)$ keV at 5.50 Torr. The measurement was repeated one year later using a different detector. The energy loss measured then at 5.500 Torr was $\Delta E = (22.7 \pm 1.2)$ keV, in agreement with the first measurement [Bla04, Dom04]. Thus, the weighted mean of the two measurements, $\Delta E = (22.3 \pm 0.7)$ keV was adopted. For these energy loss measurements, the centroids were typically near channel 1500, and were adjusted for a zero offset of $\approx +35$ channels. This offset was measured by feeding a variable-amplitude pulse generator into the Si detector preamp and extrapolating the signals to 0 volts in software. The uncertainty in the zero offset was about 5 channels, and thus the uncertainty in the energy loss due to the zero offset was about 0.3%.

To obtain a target thickness, this result was combined with literature values for the stopping power of alphas in H_2 (Fig.2.23). Because of the abundance of precise stopping power data for alphas on hydrogen, the stopping power codes SRIM and MSTAR are

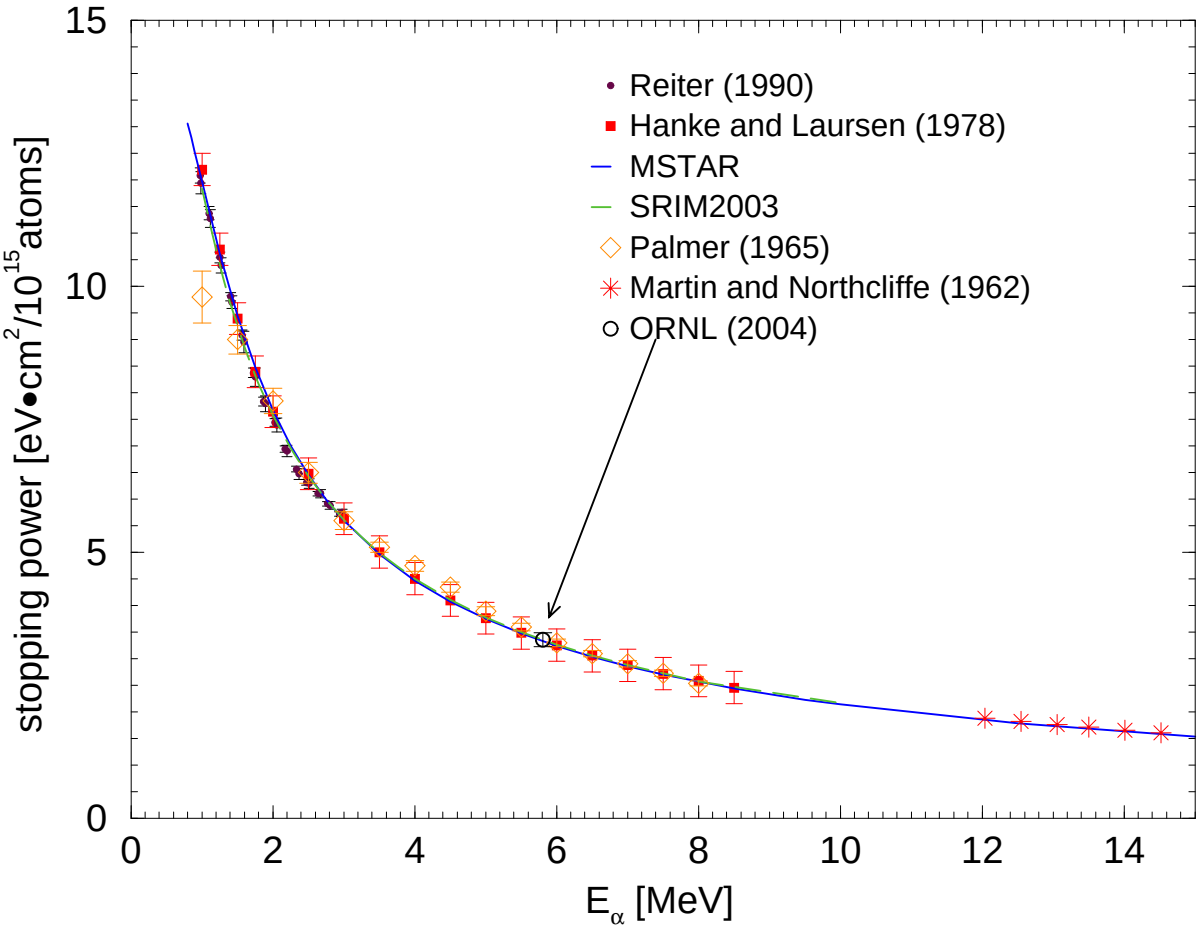

Figure 2.23: Stopping power of alphas in H_2 gas. The present datum is at 5.805 MeV. Literature values are from [Mar62, Rei90, Han78, Pal66](experiments) and [Pau02b, Bie95] (models).

well constrained in the region of interest. Also, due to the lack of data for most other ions on hydrogen, the outputs of the codes are essentially fits to the α data [Pau02a] (also see Appendix). Therefore, the uncertainty in the SRIM value for ϵ at 5.8 MeV is equivalent to the uncertainty in the literature data in that region. Thus, if the SRIM value for ϵ is used, and taking the 2% uncertainty in the data for that energy region as the uncertainty in ϵ, the gas target thickness is, $n_{5.5\,\mathrm{Torr}} = (6.9 \pm 0.3) \cdot 10^{18}\,\mathrm{atoms/cm^2}$, which is in good agreement with the ^{19}F result. Another way to look at the data is to use the alpha-energy loss measurement and the target thickness from the ^{19}F measurement to calculate the stopping power for alphas in H_2. This gives $\epsilon = (3.33 \pm 0.14) \cdot 10^{-15}\mathrm{eV{\cdot}cm^2/atom}$, which agrees within 1% with the literature value (SRIM) $\epsilon = 3.36 \cdot 10^{-15}\mathrm{eV}{\cdot}cm^2/\mathrm{atom}$, as shown in Fig. 2.23.

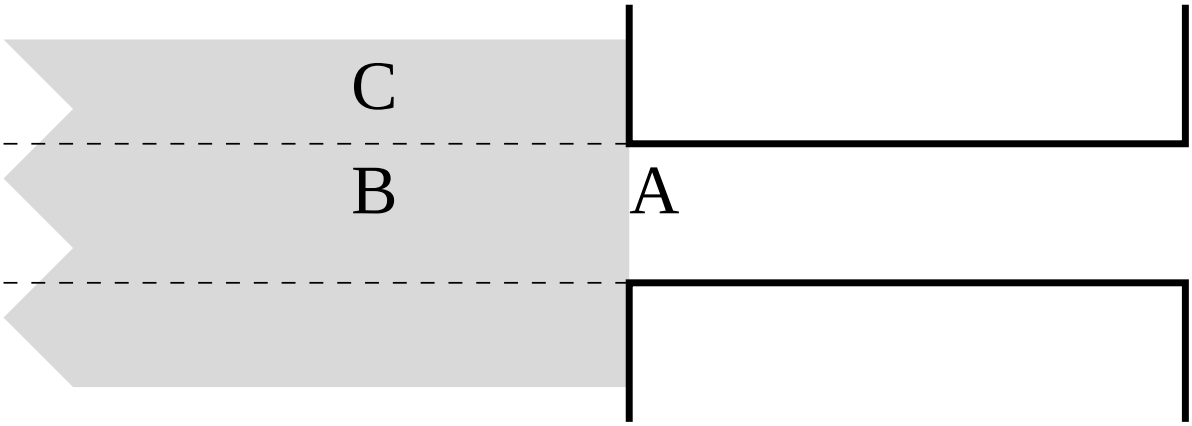

Figure 2.24: Diagram showing the 3 aperture transmission cases studied. The aperture (simplified version of A_{1u}) is 50 mm long and 3 mm in diameter. The shaded area represents the beam size. Beam direction is from left to right. See text for discussion.

Combining the results from the ^{19}F and α measurements gives a weighted mean value for the areal density of the WGT of,

$$n_{5.5\,\mathrm{Torr}} \;=\; (6.9 \pm 0.2) \cdot 10^{18}\,\mathrm{atoms/cm^2}. \tag{2.16}$$

Both of the measurements of n were sensitive to gas within the entire WGT, regardless of the pressure profile along its length. In the ^{19}F measurement, ΔE included energy lost in gas located between the analyzing magnet before the target beamline and the Si detector located downstream of the final pumping stage of the WGT. In the alpha-source measurement, ΔE included energy lost in gas located between the first pumping chamber upstream of A_{1u}, which was at $< 10^{-4}$ Torr, and the Si detector. The final value of n (Eqn. 2.3.4) is equivalent to 5.50 Torr H_2 over a length 19.5 cm. Therefore, the effective length of the WGT is,

$$L_{eff} \;=\; 19.5 \pm 0.6\,cm. \tag{2.17}$$

2.3.5 Transmission through the apertures

The areal density measurements described above account for target gas located anywhere within the length of the WGT. Therefore, during a (p, γ) measurement, recoils can

be formed anywhere within the many chambers of the target, with probabilities proportional to the pressure profile of the target. Because significant target gas is present within the first upstream and downstream apertures, A_{1u} and A_{1d} respectively, a significant flux of recoils can be made within those apertures. Calculations were performed to determine the transmission efficiency for recoils made within and beyond those apertures.

Recoils made within A_{1d} and further downstream will be transmitted through the WGT with 100% efficiency. This is simply due to the fact that all the downstream apertures are larger than the beam diameter within the target. This is described further in Sec. 2.3.1.

Of more concern are the volume of A_{1u} and its upstream chamber. Fig. 2.24 illustrates the three regions studied. Region A corresponds to recoils made by the beam at the very upstream end of the aperture. There is some probability that these recoils will collide with the wall of the aperture, and not be transmitted to the focal plane. Consider a recoil made from an axially symmetric beam, scattering at $\theta_r = 0.22°$. Only those made very close to the wall of the aperture, and scattering towards that wall will collide with it. A Monte Carlo simulation was performed for a uniform beam of parallel rays scattering at $0.22°$ at the upstream end of A_{1u} and it was found that 91% of those scattered particles passed through the aperture without colliding with its wall. More realistically, the longitudinal scattering probability distribution will increase linearly along the length of A_{1u}, due to the pressure increase. This will improve the transmission, since recoils made further downstream have less aperture to traverse. Taking the relative probability of the upstream to downstream end to be 0.2 to 1.0, the simulation yields 97% transmission of those recoils made within A_{1u}. Since less than 10% of the target gas is located within A_{1u}, the correction to the total transmission of the WGT is less than 0.3%.

A second region of interest is the pumping chamber directly upstream of A_{1u}. This region is 75 mm long. For $P_o < 6.00$ Torr, the pressure in this chamber was measured to be $P < 1 \cdot 10^{-3}$ Torr, i.e. less than 0.001% of the target gas is in this chamber. Nonetheless, there must be a pressure gradient near the face of A_{1u}. Fig. 2.24 shows two points of interest near the opening of aperture A_{1u}. As with region A, region B could also give rise to recoils lost in the aperture. Again, these would have to be created

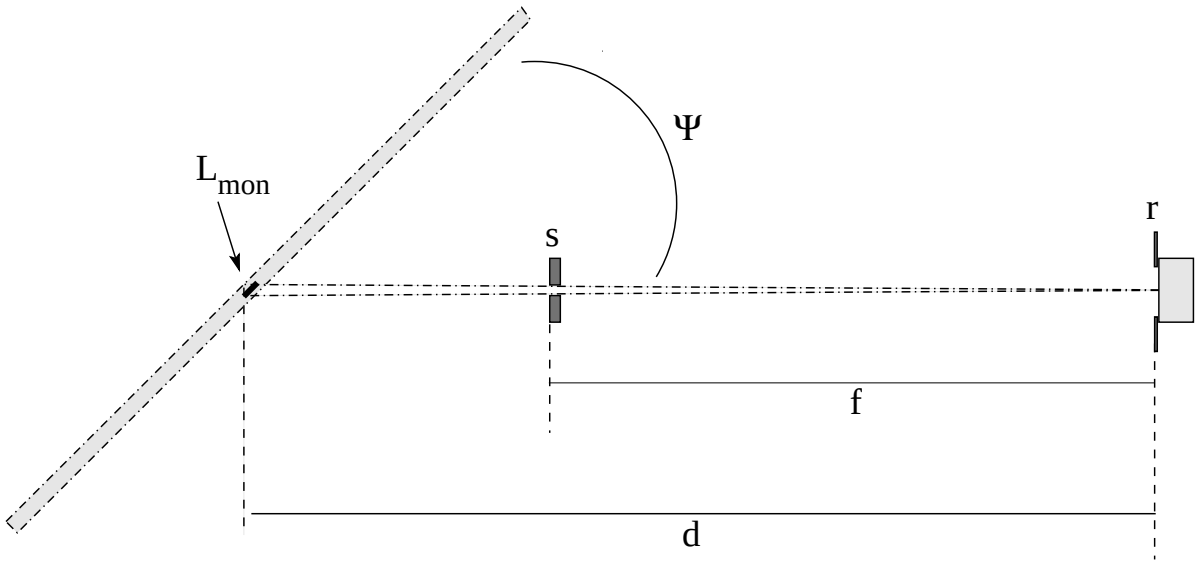

Figure 2.25: WGT double-collimated 45° monitor detector geometry. The slit width is s and the aperture radius is r.

dim	Ψ	s	f	r	d	Ω	L_{mon}
value	45.0	2.0	113	5.0	173	1.81	6.28
uncert	0.2	0.2	2	0.2	3	0.10	1.1

Table 2.6: Dimensions of the 45° monitor collimation. Ψ is in degrees, Ω in msr and all other values in mm. Ω is the solid angle for particles scattered from the center of the target, and L_{mon} is from the Monte Carlo simulation (see text).

near the circumference of A_{1u}. However, since A_{1u} is the beam-defining aperture, the beam will generally have a diameter bigger than that of A_{1u} within the region of B and C. Therefore, there could be recoils made at C, which pass through the aperture A_{1u}. These recoils would not be expected from any beam current measured downstream of the WGT, and thus would tend to inflate the transmission efficiency above 100%. Further simulations show that the losses in region B and the gains due to region C are both small ($<.5\,\%$) edge effects and cancel to first order. Therefore, 97% of the $<10\%$ of the recoils made upstream of the central disk of the gas target should successfully exit the WGT, resulting in $<0.3\%$ loss in recoil efficiency.

2.3.6 Monitor detectors

As described in 2.3.1 the WGT has ports at $\pm 45^\circ$ forward angles. On these ports are mounted collimated Si detectors. Ion-implanted Si detectors (ORTEC BU-104-150-300) with 150 mm^2 active area were used. There were no problems using these detectors in the H_2-filled WGT. The detectors were double collimated, as shown in Fig. 2.25, with dimensions shown in Table 2.6. The collimator closest to the target was an Al slit of width s, and the collimator directly in front of the detector was a 3 mm thick Al disk of inner radius r. The effective solid angle and target length seen by each detector is usually calculated following the assumptions in Rolfs and Rodney [Rol88]. We first derive that approximation, and then correct it for reality. First, the solid angle from a point source centered in the target, subtended by the circular collimator is,

$$\Omega = \int_0^{2\pi} d\phi \int_{\frac{d}{\sqrt{d^2+r^2}}}^{1} d\cos(\theta) \tag{2.18}$$

$$\Omega = 2\pi \left(1 - \frac{d^2}{\sqrt{d^2+r^2}}\right). \tag{2.19}$$

Since r$\ll$d, Eqn. 2.19 can be expanded in a MacLauren series about r/d = 0 to give

$$\Omega = \frac{\pi r^2}{d^2} \tag{2.20}$$

or

$$\Omega = \frac{A}{d^2}. \tag{2.21}$$

where A is the area of the collimator (78.5 mm^2).

However, because s/(d-f) < 2r/d, the solid angle seen by the Si detectors is partially defined by both collimators. The shadow cast by the slits can be found by projecting slits radially outward to a radius d from the center of the target. The effective aperture at the detector is shown in Fig. 2.26, where s' is the scaled slit width and t is the angle defined by the slits . Using simple geometry [Spi96], the angle t = 109.7° in Fig. 2.26 and the area seen by the detector is

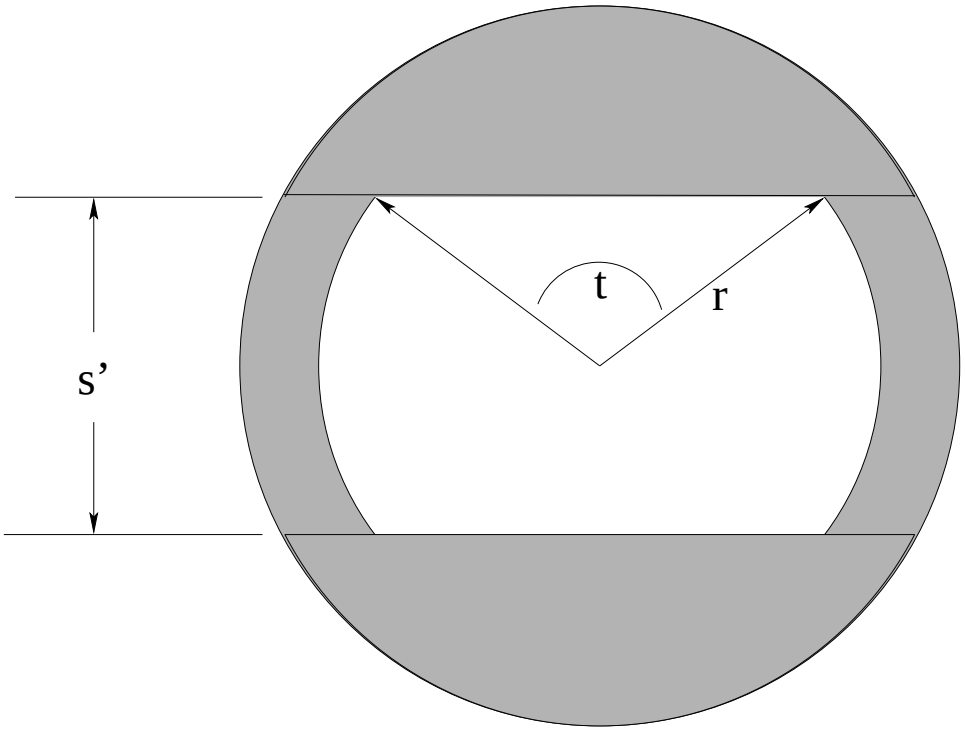

Figure 2.26: Monitor detector collimation. Shaded region shows detector area shielded by the circular and slit collimators. Dimension s' = 5.75 mm, angle t = 109.7° and r = 5.0 mm (see text).

$$A \;=\; \pi r^2 \left[\pi \;-\; t \;+\; \sin(t)\right]. \tag{2.22}$$

This gives the corrected active area of the detector to be A = 54.1 mm^2. Substituting this value for A into Eqn. 2.21 gives $\Omega = 1.806$ msr for a single 45° monitor detector (see Table 2.6). However, this solid angle is only correct for particles scattered from the center of the target. Particles scattered from a few millimeters upstream or downstream of center will see a collimator that is a skewed version of Fig. 2.26, and thus have a different Ω. A Monte Carlo simulation of the monitor detectors was run to determine the solid angle for each position along the axis of the WGT. For the central position, it gives a value of 1.805 msr, in agreement with the geometrical calculation. A plot of solid angle versus longitudinal position is shown in Fig. 2.27. This solid angle was numerically integrated over the length of the target and yielded,

$$\Omega\, L_{mon} \;=\; 11.34\, mm \cdot msr. \tag{2.23}$$

This is equivalent to the central solid angle of $\Omega = 1.81$ msr over an effective length of

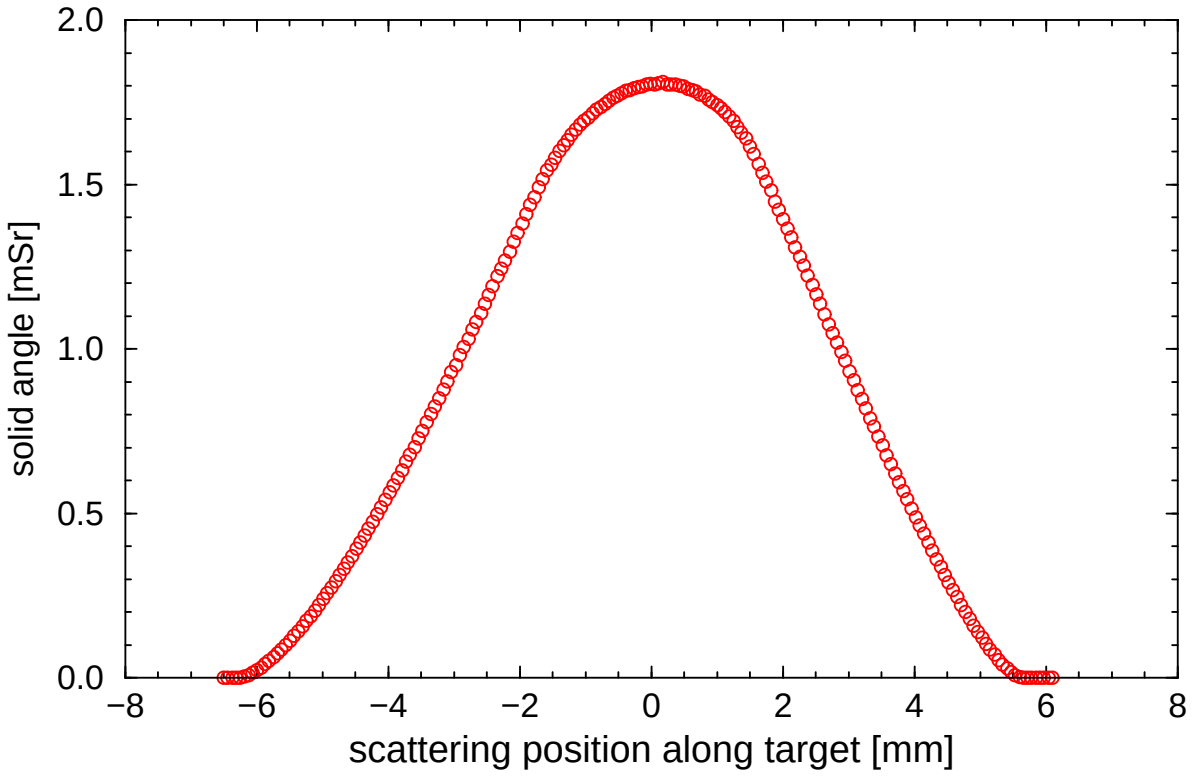

Figure 2.27: Monte Carlo simulation results for a 45° monitor detector in the gas target. The area under the curve is 11.34 mm·msr.

$L_{mon} = 6.28$ mm. The simulation also returned the scattering angle of the average particle striking the detector to be $\Theta_{eff} = 44.98°$. More importantly, the average scattering angle, weighted by the Rutherford cross section was calculated to be $\Theta_{eff} = 44.90°$. This angle should then be used to normalize reaction yields to the Rutherford law. Lastly, the simulation was run for a 3 mm diameter beam spot, corresponding to the diameter of the beam-defining aperture. This effect tends to average out and changed the solid angle by $< 0.1\%$, as expected.

The effective solid angle times target length seen by the monitor detectors was secondly determined from a Rutherford scattering experiment. A beam of 28 MeV $^{28}Si^{5+}$ bombarded the Ar filled WGT. The Coulomb barrier for the elastic scattering of the beam off the target was 47 MeV. Therefore, the elastic scattering yield in the monitor detectors should be described by the Rutherford scattering law. In that way, the solid angle times target length seen by a monitor detector,

$$\Omega\, L_{mon} \;=\; \frac{N_{mon}}{N_{beam}\,\rho\,\frac{d\sigma_r}{d\Omega}}, \tag{2.24}$$

is a function of the number of detected elastically scattered Si ions (N_{mon}), the number of beam particles incident on the target (N_{beam}), the density of the gas in the center of the target (ρ) and the laboratory Rutherford scattering differential cross section ($d\sigma_r/d\Omega$).

The beam current was measured by a Faraday cup mounted immediately downstream of the target. The cup consisted of a single-ended 10 cm long by 2 cm inner diameter Al tube, electrically isolated from the last pumping cube. The long profile of the cup was chosen to reduce the escape of secondary electrons. Permanent magnets were also mounted on opposite sides of the cup for the same reason. There was no measurable sensitivity to the presence of the magnets (within the $\approx 2\%$ limit from beam fluctuations), indicating that the geometry was sufficient to capture secondary electrons. The experiments were performed with the magnets in place. The Faraday cup leakage current was less than 1 pA. The beam current integrator (BCI) was tested with an adjustable current source, and a NIST calibrated digital picoammeter. The BCI readings were then increased 1%, in accordance with the calibrated meter.

The average charge of the beam (initially 5+) after exiting the WGT was measured as a function of pressure, with the Faraday cup. That was done by recording the BCI readings, while running the WGT at various central pressures (P_o). For each P_o, the beam current was integrated for 30 sec, followed by a second 30 sec run with no gas in the WGT. This gas-on/gas-off process was repeated multiple times for each P_o. The resulting ratio of average beam current with gas-on/gas-off was multiplied by 5.0, to give the final charge state. A plot of this average charge state versus pressure is shown in Fig 2.28. Notice that above about 2.0 Torr, the average charge state appears to drop. This is likely due to the fact that above 2.0 Torr, the beam scatters in the gas to large angles, greater than the $\approx 0.5^\circ$ acceptance of the downstream apertures. This idea was confirmed by running SRIM simulations for various pressures. Furthermore, this intense scattering reflects the large Rutherford cross section for low energy Si + Ar scattering. This effect is not present for ^{7}Be on H scattering, due to the much lower elastic scattering cross section. SRIM calculations reveal that 12 MeV ^{7}Be on the WGT

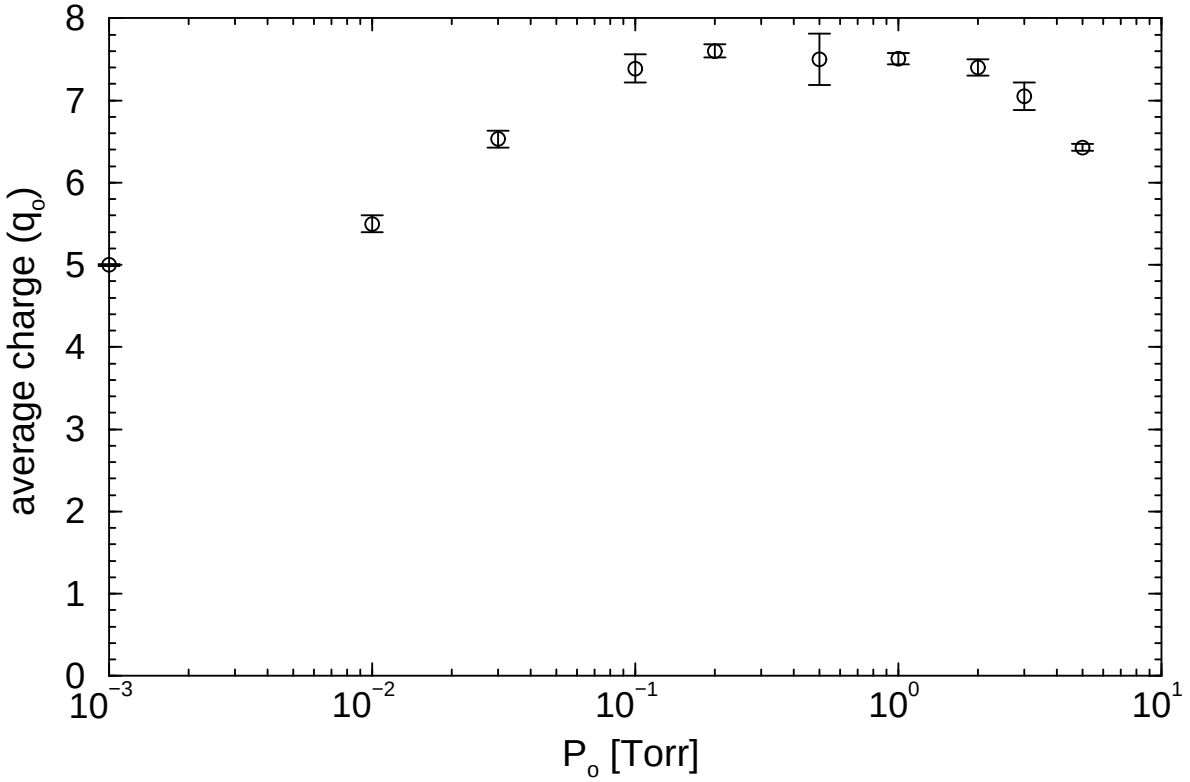

Figure 2.28: Average charge state vs.P_o for a ^{28}Si beam on the ^{40}Ar-filled WGT. The lowest pressure point is from running the WGT with no gas flow.

at $P_o = 5.50$ Torr, straggles on average only 0.007° over the length of the target. In light of this straggling issue, the $P_o = 1.0$ Torr data were used in Eqn. 2.24 to determine $\Omega \cdot L_{mon,top} = 10.2\,\text{mm} \cdot \text{msr}$ and $\Omega \cdot L_{mon,bottom} = 10.1\,\text{mm} \cdot \text{msr}$, for the top (+) and bottom (-) 45° monitor detector, respectively. These values are 11% lower than the value calculated using the Monte Carlo. Better agreement should be reached, and further measurements with Faraday cups are planned. However, the solid angle of the monitors did not factor into the $^1\text{H}(^7\text{Be},\gamma)^8\text{B}$ cross section measurement (see Eqn 4.1). Instead, a more robust method was used, as described in Sec. 4.4.

The Si + Ar scattering experiment was also used to determine the angles of the monitor detectors. The ratio of elastically scattered Si to Ar in each monitor is sensitive only to the Rutherford cross section for the center-of-mass angle involved, and the conversion of center-of-mass to laboratory solid angle. In that way, the average scattering angle into each monitor detector was found to be (45.0±0.1) degrees.

2.4 Recoil separation and detection

2.4.1 DRS specifications

The beam particles exiting the WGT during a (p,γ) experiment typically outnumber the reaction products they produce by a factor of 10^{12}. Therefore, a recoil separator is needed to guide the fledgling recoils to a detector, while rejecting the bulk of the beam particles. Because the beam and recoils from low Q-value (p,γ) reactions have nearly identical momenta, the velocity filters are key to separating the two groups (see 2.1). The Daresbury Recoil Separator (DRS) was used for the ^{1}H(^{7}Be,γ)^{8}B measurement and is shown schematically in (Fig. 2.29). The DRS was built and used at Daresbury (UK) laboratory during the 1970's and 1980's to study heavy ion reactions with recoils having $A/q \approx 5$ and $v/c \approx 5\%$ (for instance: 275 MeV ^{80}Se on ^{54}Cr) [Jam88]. The DRS was acquired by ORNL's HRIBF in the 1990's. The physical characteristics of the DRS are still similar to the 1988 characterization and are described thoroughly in [Jam88].

The DRS is a 13 m long, 90 ton electromagnetic separator, shown schematically in Fig. 2.29. The first element of the DRS is a quadrupole triplet (Q1), which is designed to accept a large angular bite (5°) of recoils exiting the target and to focus those recoils into parallel rays. The beam and recoils would then pass to the first velocity filter (VF1), which allow a beam of velocity $v_o = |\vec{E}/\vec{B}|$ to pass unabated (in the case of ^{1}H(^{7}Be,γ)^{8}B, the ^{8}B recoils have 7/8 the velocity of the ^{7}Be beam particles). The magnitude of acceleration of beam particles of mass m and velocity $v = v_o + \Delta v$ is,

$$a = \frac{q}{m}\frac{\Delta v}{v_o}|\vec{E}|. \tag{2.25}$$

Therefore, it is generally desirable to run high fields in the filters, to improve the separation between the beam and recoil groups. However, it is also important that the beam groups are stopped on the slits, following each velocity filter. So if the electric fields are run too high for a given velocity, the beam can be diverted into the high-voltage plates themselves, and lead to undesirable scattering. Therefore, for a given beam and slit position, a best velocity filter voltage should be found experimentally. Typically,

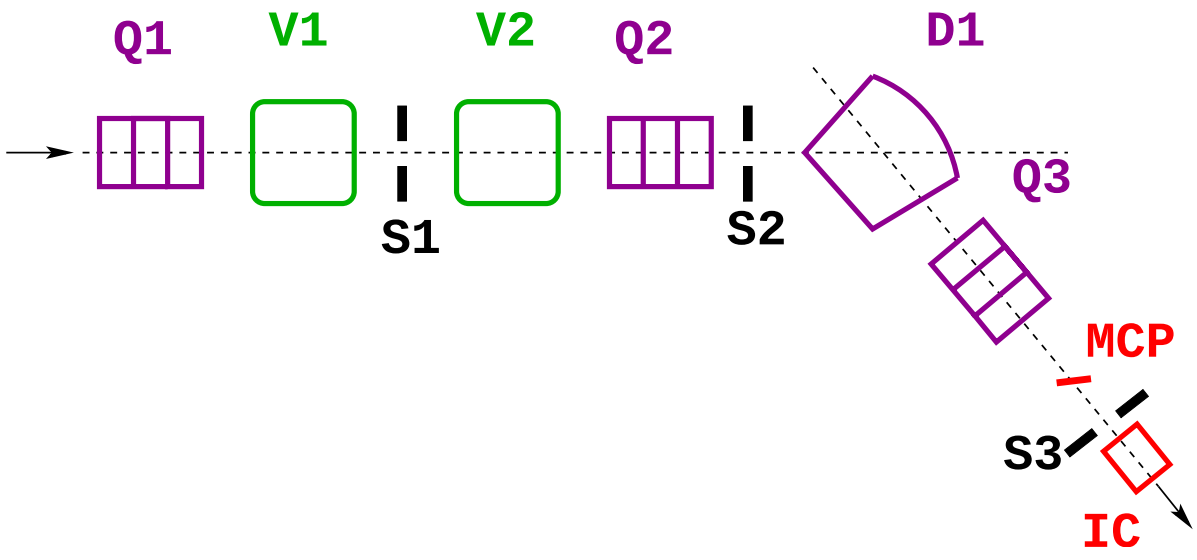

Figure 2.29: Schematic of the DRS (not to scale). Abbreviations explained in the text.

the electric field is set at 1.0-1.5 kV/mm within the cavity, which moves the beam a few centimeters off axis horizontally by the end of VF1 so it can be intercepted by a set of horizontal slits (S1). VF1 is followed by a second velocity filter (VF2) with the field directions reversed, and then another set of slits (S2). The velocity filters are followed by a second quadrupole triplet (Q2) and a pair sextupole magnets (unused). Q2 focuses the recoil group vertically for passage through the 50° dipole magnet (D1). The beam and recoils leaving VF2 are dispersed in velocity along the horizontal plane and are finally dispersed in Mv/q by the dipole magnet. The system is designed such that, for the recoil group, the velocity dispersion from the dipole matches the velocity dispersion from the velocity filters, to produce a monochromatic beam at the focal plane. This dispersion matching is completed by the third quadrupole triplet (Q3) which refocuses the rays that were made parallel by Q1. Groups differing in A/q are focused to different points at the "focal plane" of the DRS [Jam88]. Finally, a microchannel plate (MCP) and a gas filled ion counter (IC) are located 1 m upstream, and at the focal plane respectively. Mounted 5 cm directly upstream of the focal plane is a pair of horizontal slits (S3), which can be used to block out undesired beam or reaction products which are off-center at the focal plane.

2.4.2 Focal plane detectors

The gas-filled ion counter (IC), and carbon-foil microchannel plate (MCP) can be used together to identify the position, energy, and atomic species of incoming particles. The IC identifies incomming particles by atomic number and energy, and the MCP identifies the x-y postion and precise time of the arrival of an ion.

The gas-filled ionization counter (IC) is a 30-cm long particle detector with 3 anode segments and a single cathode. The front polypropylene window has a diameter of 5 cm and at 50 μg/cm^2 can hold 20 Torr of isobutane gas. A schematic of the IC is shown in Fig. 2.30. A Frisch grid ensures that the energy signals from the anodes are position independent. However, horizontal position information can be determined by measuring the time delay between the anode and cathode signals. The 3 anode (ΔE) signals are combined to give the total energy of the particle, and the particle is identified from the various grouping in ΔE vs. Energy plots (see [Jam88]). Backscattering from the window is negligible, so the efficiency of the detector is 100%. A sample ΔE vs. E IC plot is shown in Fig. 2.32.

A carbon-foil microchannel plate (MCP) is mounted about 1 m upstream of the IC [Sha00]. A schematic of the detector is shown in Fig. 2.30. The 7 cm diameter C foil is mounted at 40° with respect to the beam on an Al grid for support. The transmission through the foil and grid is 85%. The position-sensitive anode signals are processed to reproduce the position of the incident ions perpendicular to the beam axis to 1 mm resolution. Also, since the timing resolution of the detector is excellent (better than 1 ns) it can be used to tag recoils for time-of-flight or coincidence measurements. Sample MCP spectra are shown in Fig. 2.32 and described in Sec. 2.4.3.

2.4.3 DRS characterization

Previous to the work reported here, the magnets of the DRS were calibrated with NMR probes and the optics and transmission were studied using GEOS calculations and previous experience from Daresbury. Six "knobs" were setup for the DRS, each controlling a defined linear combination of magnetic elements with a specific function

knob	1	2	3	4	5	6	7	8
value	1	-2	-3.5	2.5	0	0	V1	V2

Table 2.7: Best knob settings for the DRS. Knobs 7 and 8 are set to the average plate voltages in kV for VF1 and VF2 respectively.

within the DRS system. Through various beam and source experiments, knob settings were found that optimized the transmission of recoil nuclei, rejection of beam particles, and dispersion matching at the focal plane. It was found that this single, good set of knob parameters could be scaled for various reactions. The settings are listed in Table 2.7.

Various parts of the DRS, WGT, and focal plane detector system were tested independently and together. The focal plane resolution and acceptance were assessed first with an ^{244}Cm α source mounted at the target position. The DRS was setup to transmit 2+ charged alphas, which were in turn counted at the focal plane of the DRS in a gas-filled ion chamber (IC). The fraction of the known source decay rate which was detected at the focal plane ($2.8{\cdot}10^{-4}$) indicated that the angular acceptance of the separator was 3.5 msr, or 1.9°. Next, the DRS charge state setting (q) was adjusted away from this nominal value, and the decrease in count rate at the focal plane was recorded. The results from that test are displayed in Fig. 2.31, for 3 different velocity filter settings. When the velocity filters were set at $\pm$50 kV and $\pm$100 kV, the FWHM acceptance of the detector was 4.5% and 2.7% in A/q respectively. Next, the DRS was tested with fusion-evaporation products from 50 MeV ^{16}O on a 50 μg/cm^2 carbon foil. The DRS was tuned for $^{26}Mg^{10+}$ and the Mg and other reaction products were separated from the beam in the IC, as shown in Fig. 2.32 (left). Then the MCP position spectrum was gated by the various groups in the IC. The resultant MCP spectra are shown in Fig. 2.32 (right). The $^{26}Mg^{10+}$ group is off-center on the MCP, which implies an A/q offset of 2%, and has a FWHM $\approx$ 2 cm. The two Mg groups are separated by 4 cm, which leads to a resolution of 1/50. The MCP spectra is only an approximate measure of the recoil focus at the IC, since it is located 0.7 m upstream of the IC. Thus, the final tune of the DRS was not pursued using the MCP.

Further tests of the DRS system were performed using the WGT and stable beams. The transmission of ^{7}Be , ^{10}B, ^{12}C and ^{24}Mg beams as well as recoils from both the $^{12}C(p,\gamma)^{13}N$ the and the $^{24}Mg(p,\gamma)^{25}Al$ reactions were studied (Sec. 3). For these cases, the knob parameter space was searched, leading to the values in Table 2.7. Also the q/A setting of the DRS was explored. It was found that for high q/A, the DRS needed to be set up at a value 1% higher than the actual charge state of the beam in order to center the group in the IC. For example, 12.9 MeV $^{10}B^{2+}$ was centered at the focal plane by setting the DRS at $q = 1.99$. On the other hand, 12.9 MeV $^{10}B^{5+}$ was centered by setting the DRS for $q = 5.05$. This effect is therefore at most a 1% effect, likely due to imperfection in the hall probe calibration. Also, the $^{10}B^{5+}$ beam group was found to be well focused at the focal plane with FWHM $\approx$ 5 mm. Since the recoils from $^{1}H(^{7}Be,\gamma)^{8}B$ are emitted in a cone of only 0.22° and with a small energy spread, it is expected that they will likewise be well grouped at the focal plane. With the focal plane slits open to $\pm$2.3 cm, the FWHM acceptance of $^{10}B^{5+}$ was 5% in A/q.

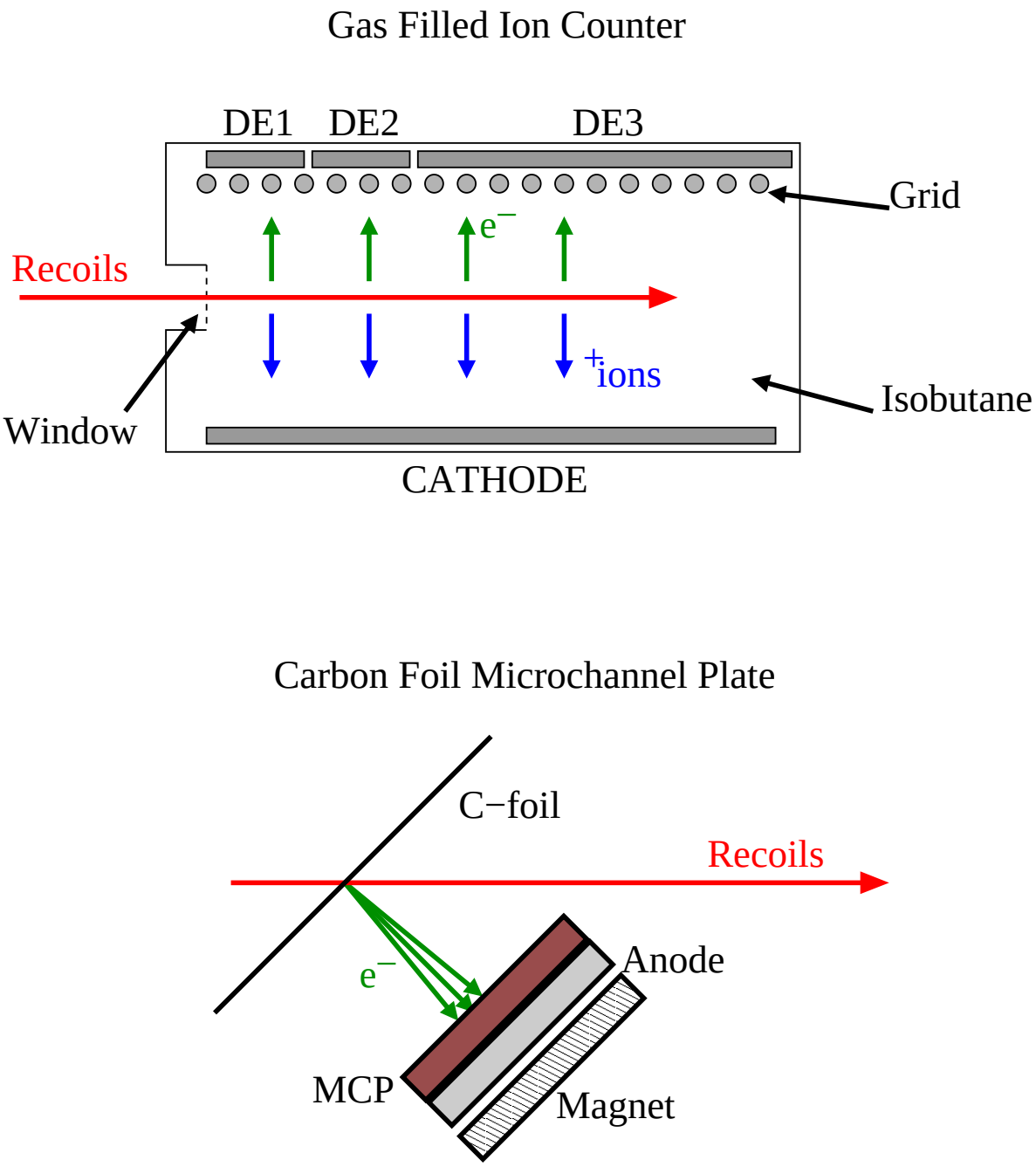

Figure 2.30: DRS focal plane detectors. The gas filled Ionization Chamber (IC) is shown on top and the carbon-foil microchannel plate (MCP) is shown on the bottom. The MCP acceleration grids are not shown.

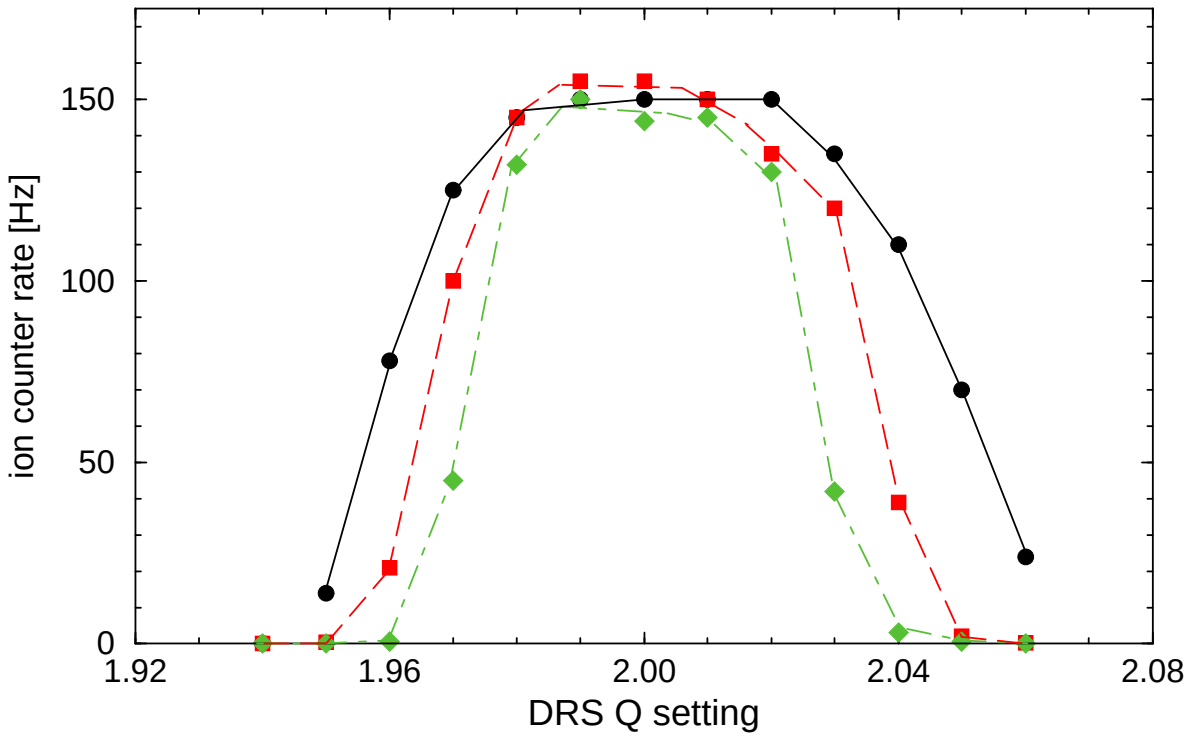

Figure 2.31: DRS transmission of 5.8 MeV alphas for velocity filter settings of ±50 kV (solid), ±75 kV (dashed) and ±100 kV (dot-dashed). The maximum of each curve indicates the angular bite of the system, and the width indicates the angular dispersion (see text).

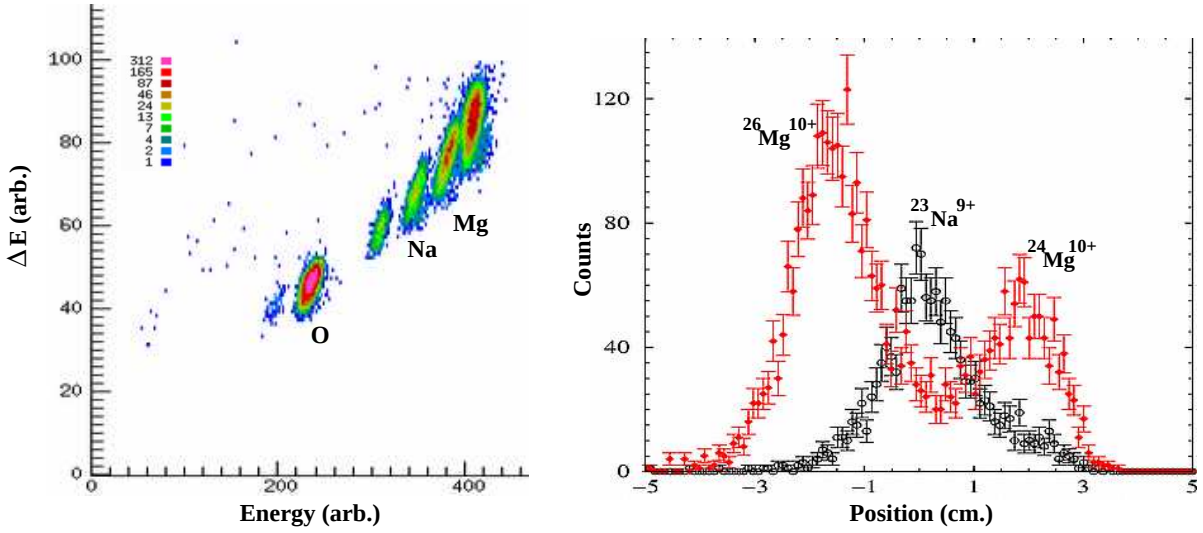

Figure 2.32: IC particle ID spectrum from 50 MeV ^{16}O on ^{12}C target (left). Beam and fusion - evaporation groups are clearly separated. Corresponding MCP horizontal position spectrum for Na and Mg IC gates is shown (right). The DRS was set for $^{26}Mg^{10+}$ (see text).

Chapter 3

Proton capture measurements using stable beams

3.1 $^1H(^{12}C,^{13}N)\gamma$

The performance of the WGT plus DRS system was studied using the $E_{r,cm} = 1.56\,\mathrm{MeV}$ resonance in the $^1H(^{12}C,^{13}N)\gamma$ reaction. The parameters for this resonance are shown in Table 3.1. The maximum angle at which recoils are emitted from this reaction is 0.33°, which is larger than the 0.2° opening angle for ^{1}H(^{7}Be, γ)^{8}B . Therefore, this reaction is a good test of the recoil angle acceptance of the gas target and DRS. As mentioned earlier, the gas target acceptance was designed to be 0.5° and the DRS acceptance to be 2°. The resonance energy and width were taken from [Kis89], which reports the most precise measurements. These agree with the values suggested in the review [Til02]. The resonance energy and width in the lab frame are $E = 20.11$ MeV and $\Gamma = 0.787$ MeV. The beam energy used was $E = 20.23$ MeV and the energy loss of th beam through the target was $\Delta = 0.120$ MeV. Therefore the resonance was broader than the target thickness, and the resonance was almost centered in the target. The literature resonance strength was determined by re-analysis of the thick target measurement data found in [Sea51]. In that paper, a thick target yield curve for 0.4-2.0 MeV protons on a graphite target were reported. Positron annihilation was measured from the bombarded targets using a NaI crystal, which had been calibrated with ^{22}Na and

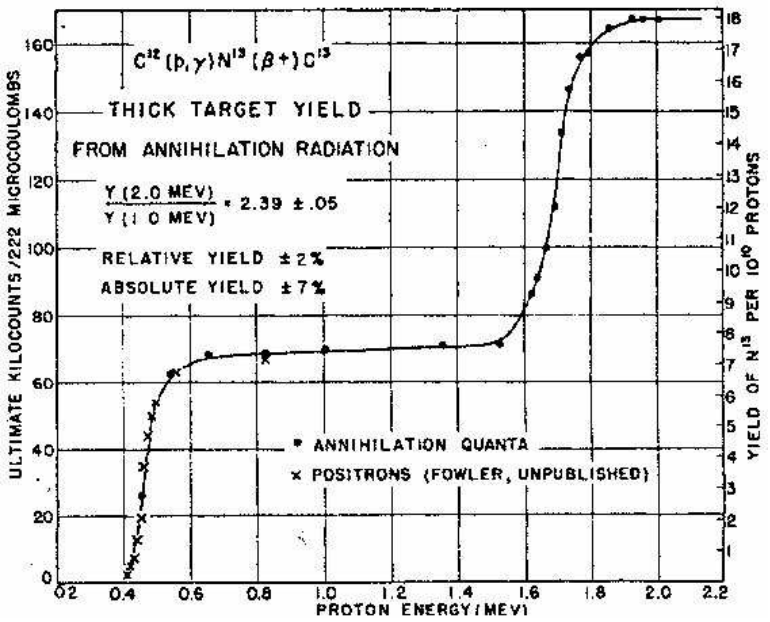

Figure 3.1: $^1H(^{12}C,^{13}N)\gamma$ yield curve from [Sea51].

^{60}Co sources (Fig. 3.1). They reported, to 2% accuracy, the ratio of the reaction yield at 2 MeV to that at 1 MeV,

$$\frac{Y(2.0)}{Y(1.0)} = 2.39 \pm 0.05. \tag{3.1}$$

They then extracted resonance strengths and peak cross sections from the yield curve. They report $\omega\gamma = 0.67$ eV for the lower energy resonance and $\omega\gamma = 1.39$ eV for the higher resonance. However the resonance energies and widths that they used for this extraction were not well known at the time. Furthermore, the stopping power values they used were not reported, and can be inferred to be inconsistent with modern values. However, a recent set of thin and thick target measurements of the lower energy resonance ($E_r = 0.42$ MeV) finds a value for that resonance strength of $\omega_\gamma = 0.53 \pm 0.05$ eV [Hin92]. The authors also re-analyze the lower energy resonance strength from [Sea51], using modern stopping power values, and find $\omega_\gamma = 0.52$ eV. Since [Sea51] quote a small uncertainty only for the relative yield of the two resonances, the most precise value for the $E_r = 1.56$ MeV resonance comes from combining the ratio Eqn. 3.1 with the strength of the $E_r = 0.42$ MeV resonance measured by [Hin92]. The width of the lower energy resonance is $\Gamma = 31.7 \pm 0.8$ keV [Til02]. Therefore, this new value for the lower energy

Q	E_x	$E_{r,cm}$	Γ_{cm}	J^π	ω_γ
1943.5	3501.3	1557.8 ± 0.7	61 ± 2	$3/2^-$	1.1 ± 0.1

Table 3.1: Literature values for $^{12}C(p,\gamma)^{13}N$ resonance parameters. See text for references and discussion. Energies in keV, strength in eV.

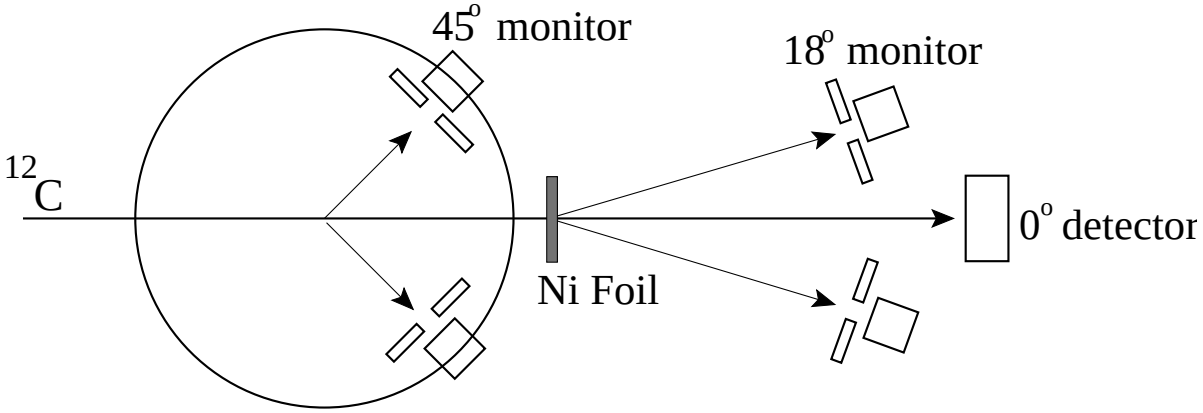

Figure 3.2: $^1H(^{12}C,^{13}N)\gamma$ normalization setup.

resonance strength, together with modern values for the energies and widths of the 2 states and the modern stopping power curve for protons on carbon [Bie95], which agrees with 3.5%-accurate data in that energy region [Gor67], were used to find an accurate value for the strength of the higher energy resonance. This re-analysis of [Sea51] gives $\omega_\gamma = 1.1 \pm 0.1$ eV and $\sigma_R = 32 \pm 3$ μbarns for the $E_r = 1.56$ MeV resonance. These values were considered "literature values" for this resonance and are listed in Table 3.1.

The ^{12}C beam current (180 nA) was monitored with the $\pm 45°$ detectors in the WGT. An absolute beam current normalization was accomplished using a two step normalization procedure. The setup is shown in Fig. 3.2. In the first step, the 0° detector was retracted from the beam path, and a beam current of $\approx$ 1 ppA passed through the gas target ($P_o = 5.00$ Torr) and then through a 450 μ g/cm^2 ^{58}Ni foil which was mounted on a 2 cm diameter target ring. The number of counts in each of the 45° detectors in the WGT and 18° detectors looking at the Ni foil were recorded. Next, two sieves were placed in the beam path more than five meters upstream of the WGT to cut the beam intensity down by a factor of 1,000. Thus, the beam intensity was cut down to about 6,000 particles per second. A final Si detector was moved into the beam path

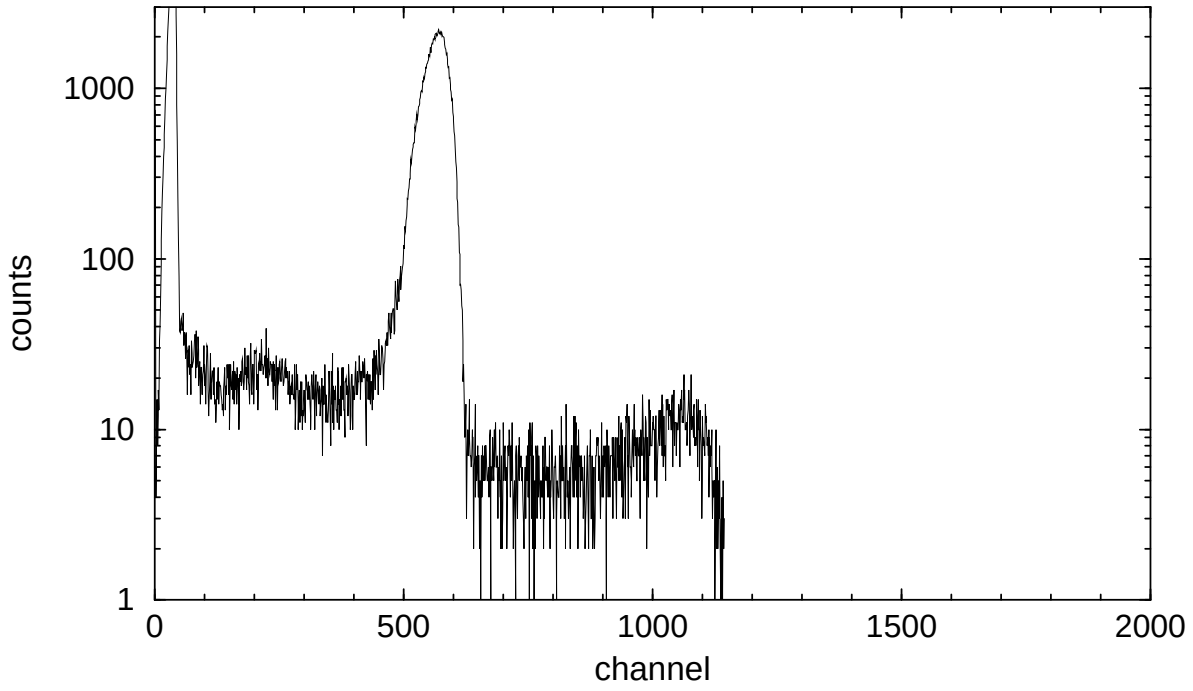

Figure 3.3: 18° Si detector Spectrum showing 20.1 MeV ^{12}C elastically scattering off ^{56}Ni (first peak). Also evident are low energy scattered beam, low energy Ni recoils and the Carbon pileup peak.

at 0° downstream of the Ni foil. In this second phase of the experiment, the counts in both 18° detectors and the 0° detector were recorded. Taking the double ratio of the counts from these two parts of the experiment gave the absolute normalization of the 45° detectors,

$$\frac{N(45^\circ)}{N(0^\circ)} = \frac{N(45^\circ)}{N(18^\circ)}\frac{N(18^\circ)}{N(0^\circ)}. \tag{3.2}$$

The use of the sieves resulted in improved reproducibility, compared to using the ion source tuning parameters to reduce the beam current for the second phase of the experiment.

The accuracy was limited by pileup in the 0° and 18° detectors during their respective high count-rate phases. The fact that the pileup effect in both the 0° and 18° detectors was about equal indicates that the foil scattering geometry was near optimal. The only way to further reduce the pileup would be to increase the solid angle of the 45° detectors in the WGT disk. However, the well constrained double-apertures of the 45° detectors were chosen to produce well-defined elastic scattering peaks for normalization and also

to facilitate geometrical definition of the the solid angle (see Sec. 2.3). The pileup was typically 10% of the full energy peak, as seen in Fig. 3.3. For $E_{lab} = 20.23$ MeV ^{12}C on the WGT at $P_o = 5.000$ Torr the double ratio gives,

$$\frac{N(45^\circ)}{N(0^\circ)} \;=\; (2.89 \pm 0.15) \cdot 10^9. \tag{3.3}$$

To obtain a resonance strength, the stopping power of ^{12}C in H_2 must also be known. This was determined using the previously measured areal density of the WGT and the energy loss of the beam in the WGT. The energy loss was measured using a Si detector at 0° using the same method described in Sec. 2.3.4. The energy loss at $P_o = 5.50$ Torr was $\Delta E = 134 \pm 1$ keV. So the stopping power for an incident beam energy of $E_{lab} = 20.23$ MeV was determined from n and ΔE to be

$$\epsilon \;=\; (1.91 \pm 0.02) \cdot 10^{-15} ev\, cm^2/atom. \tag{3.4}$$

The beam suppression of the DRS was $4 \cdot 10^{-11}$ which resulted in a 70 Hz total count rate in the IC. As a test of the recoil transmission, the slits after each velocity filter of the DRS were widened to allow a factor of 10 worse beam rejection. However, the recoil counting rate did not increase during those tests, so the slits were moved back in. Data were taken with the DRS tuned for 4+, 5+, 6+ and 7+ ^{13}N recoils at the focal plane. The resulting recoil charge-state distribution is listed in Table 3.2. Typical IC and monitor detector spectra are shown in Fig. 3.4.

The total reaction yield was measured to be $1.83 \cdot 10^{-10}$ per incident ion. The resonance strength was then determined by integrating a Breit-Wigner cross section (Eqn. 1.20) over the energy range of the beam in the target,

$$Y \;=\; \frac{\omega_\gamma\, \lambda^2}{\epsilon} \left(tan^{-1} \left(\frac{E_B - E_r}{\Gamma/2} \right) \;-\; tan^{-1} \left(\frac{E_B - E_r - \Delta}{\Gamma/2} \right) \right). \tag{3.5}$$

Since the target is much thinner than the width of the resonance, and the beam energy is near the resonance energy, Γ was taken to be Γ_R. Substituting the measured

q	%	$\pm$
4	<0.5	—
5	5.9	0.2
6	48.7	0.4
7	45.7	0.4

Table 3.2: charge-state distribution of ^{13}N recoils exiting the WGT with mean energy of 18.6 MeV. % error is statistical uncertainty only.

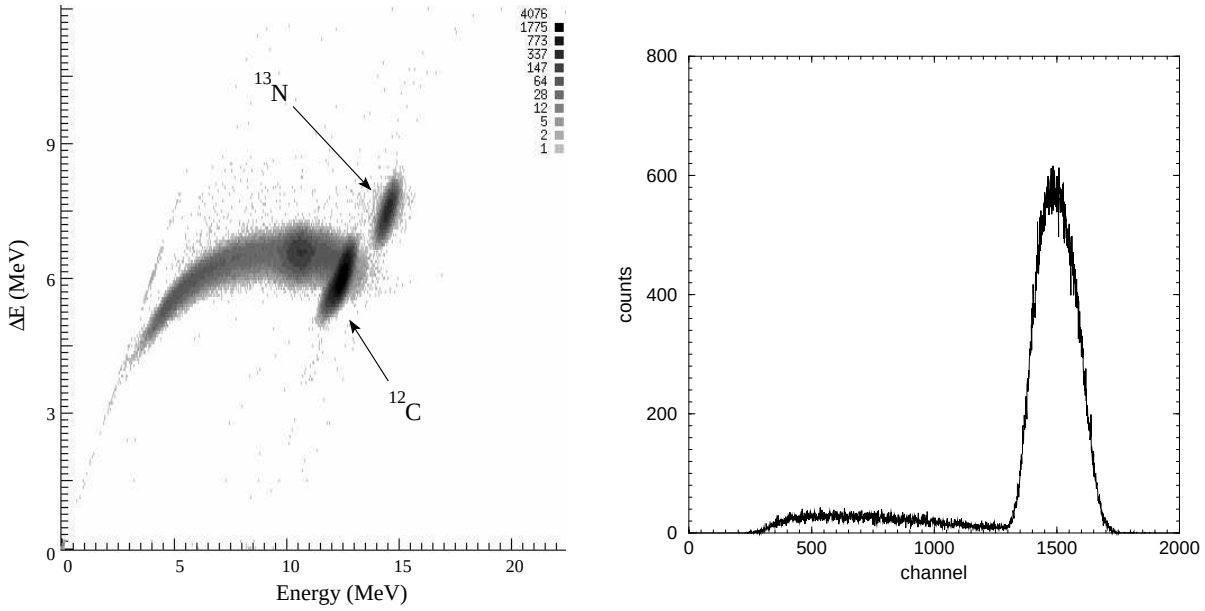

Figure 3.4: Typical IC spectrum for 6+ ^{13}N at the focal plane (left). Corresponding 45° elastic scattering spectrum (right).

variables, and solving Eqn. 3.5 for the resonance strength gives $\omega_\gamma = 0.90 \pm 0.1\,eV$. Using Eqn. 1.22, the peak cross section is then $\sigma_r = 27 \pm 3\,\mu$barns. This strength value agrees with the literature value of $\omega_\gamma = 1.10 \pm 0.1\,eV$, which is consistent with 100% transmission of ^{13}N recoils through the WGT and DRS.

As a quick check of the resonance parameters, an excitation function was performed over the resonance. To normalize the 45° monitor detectors at each energy, a run was performed in which the beam passed through the WGT and onto an Al plate mounted downstream of the last pumping stage. Thus, the ratio of monitor detector counts to integrated beam current (BCI) was recorded for each energy. The relative reaction yield

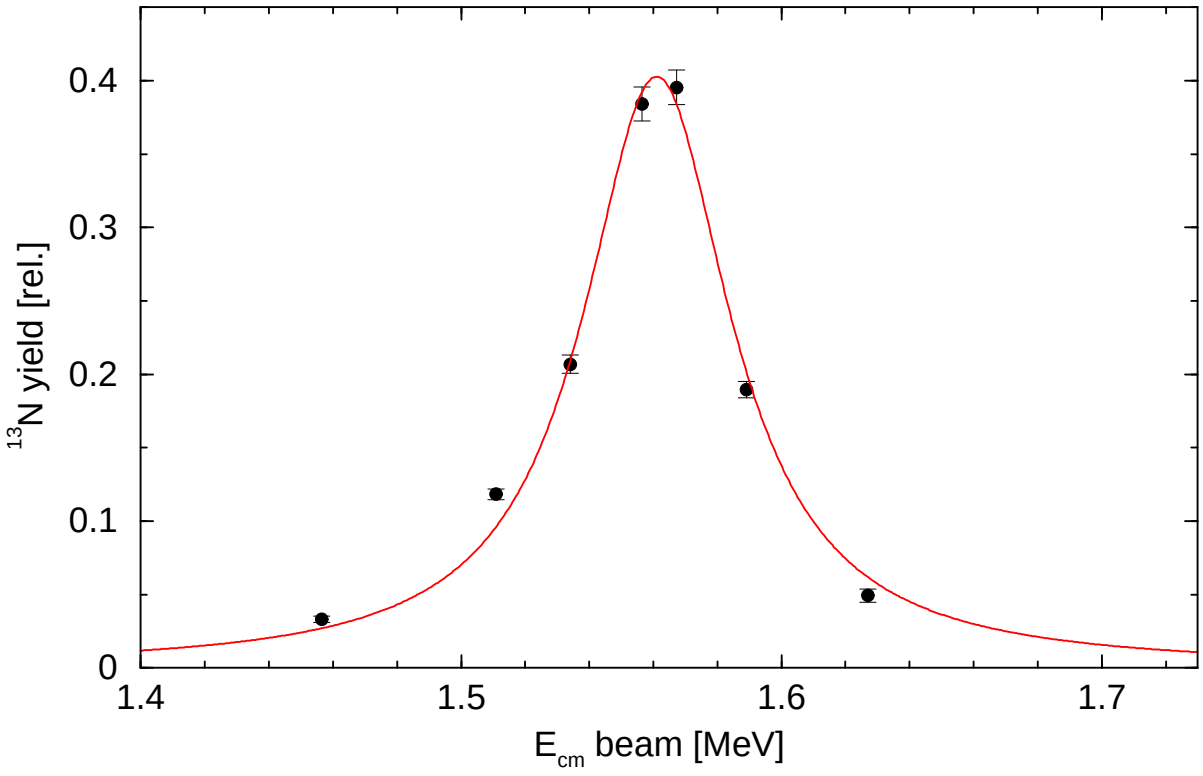

Figure 3.5: $^{1}H(^{12}C,^{13}N^{6+})\gamma$ excitation function with incident beam energy in cm units. Breit-Wigner fit with $\Gamma = 60.5$ keV and $E_{r,cm} = 1.560$ MeV (solid). This corresponds to an energy of $E_{r,cm}$ =1.560 MeV in the center of the target. The error bars are from statistics only.

was then determined by,

$$Y = \frac{^{13}\mathrm{N}}{\mathrm{monitor}} \frac{\mathrm{monitor}}{\mathrm{BCI}}. \tag{3.6}$$

The plate measurements at each energy were used to determine the relative elastic-scattering cross section for the monitor calibration. That normalization varied by a factor of 3 over the energy range of the experiment (Fig. 3.5), and included an un-quantified error from the use of the unsuppressed plate for integrating the current. However, the shape of the excitation function is roughly consistent with a Breit-Wigner shape. The resultant excitation function for $^{13}N^{6+}$ recoils is shown in Fig. 3.5 along with a Breit-Wigner fit with $\Gamma_{cm} = 60.5$ keV and a peak for the beam energy of $E_{cm} = (1561 \pm 2)$ keV. Subtracting 1/2 the energy loss of the beam through the WGT gives the experimental resonance energy at the center of the target $E_{r,cm} = (1556 \pm 3)$ keV which agrees with the literature value of $E_{r,cm} = (1557.8 \pm 0.7)$keV [Kis89].

During the above experiment, a quad-segmented "clover" Ge detector was mounted at 90° to the WGT at a distance of ≈ 20 cm from the disk. The setup is shown in Fig. 3.6. The γ-rays emitted from the $^1H(^{12}C,\gamma)^{13}N$ reaction were recorded and a time stamp was placed on all the events in the experiment. Then, coincidences between the Ge clover and the ^{13}N ions in the IC at the focal plane were identified in software. If the transmission of the DRS plus WGT is 100%, then the ratio of singles γ-rays to coincident γ-rays should be given by the charge state fraction of the recoils for which the DRS is tuned. As shown in Fig 3.6, the detector was most sensitive to γ-rays emitted at lab angles ≈ 90°. Recoils associated with those γ-rays would also be emitted at maximum laboratory angles. The Pb bricks shielded the detectors from γ-rays made furthest upstream, so the recoil-γ efficiency was also most sensitive to reactions downstream of aperture A_{1u}.

The 4 clover segments were summed together for improved efficiency. The summed raw spectrum (called addback) is shown in Fig. 3.7 along with the same spectrum gated on the ^{13}N group in the IC at the focal plane. The ground state transition ($E_\gamma = 3.50$ MeV) has a branching ratio of 92% [Til02]. Unfortunately, as can be seen in Fig. 3.7, the region of interest in the Ge spectrum is dominated by background radiation. The γ-ray background probably originates from interactions between the beam and the upstream brass apertures. Therefore, a background run was taken without gas in the WGT, and subtracted from the singles spectrum. Since the 45° monitors did not count with the gas off, the target on and target off spectra could not be normalized for beam current. Instead, they were normalized to the high energy spectrum (ch 350-400). This segment of the spectra turned out to be nearly equivalent to normalizing to live time, as the beam current was fairly constant over the ≈ 12 hours of run time. The background subtracted (net) spectrum is shown in Fig. 3.8.

The net spectrum reveals 2 characteristics that challenge the analysis. First, the peaks are significantly Doppler broadened. This broadening was due to the fact that both the target, and detectors were extended, and that the detectors were at 90° to the target. The difference in Doppler shift between the left 2 detectors and the right 2 detectors could be corrected for, however that correction is complicated by the summing among the detectors in the addback spectrum. Therefore, no Doppler correction was

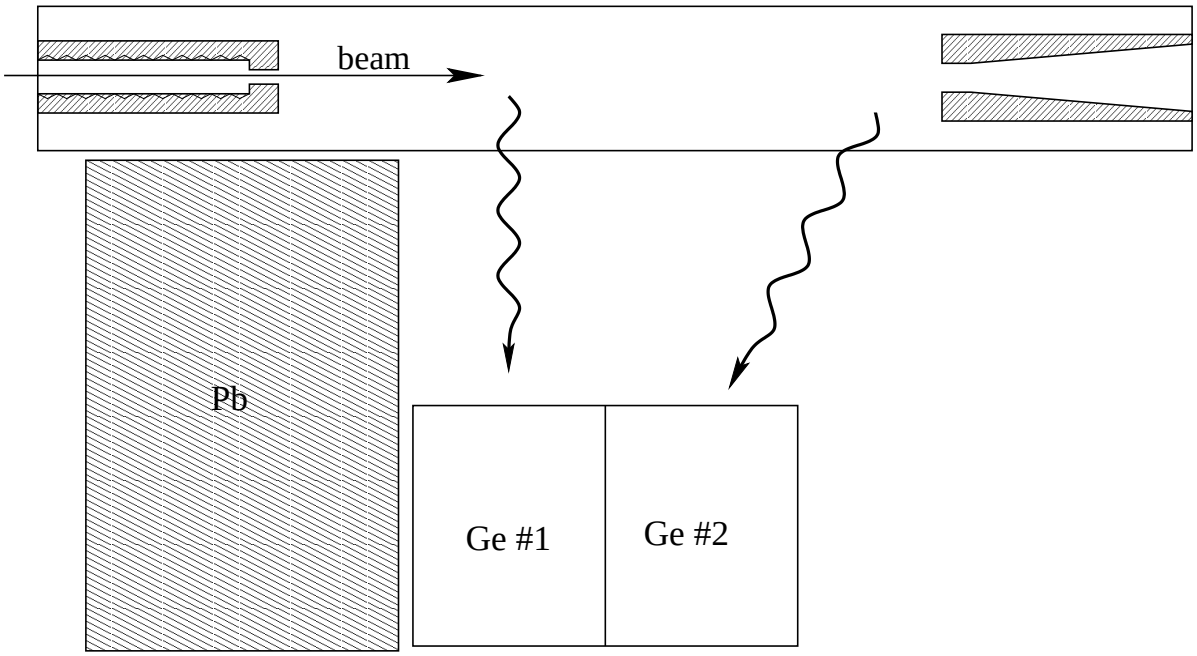

Figure 3.6: Ge clover detector setup, top view with top and bottom Pb shielding removed. Segments #3 and #4 are directly below #1 and #2.

not applied. A second difficulty in the analysis was caused by the appearance of γ-ray peaks from the de-excitation of ^{13}C. These peaks likely result from the $^{2}H(^{12}C,p)^{13}C$ reaction between the beam and the 0.015% ^{2}H [Lid90] in the WGT. Since the ^{13}N peak sits under the Compton background of the ^{13}C peaks, the Ge response functions for all 3 of the peaks need to be added together. This was done by gain shifting and scaling copies of the coincidence gamma spectrum from the ^{13}N ions to fit the higher energy ^{13}C photopeaks. This is only an approximation to the Ge spectra from those peaks, since they will have different Doppler shift from the ^{13}N peak, due to the different kinematics involved. Nonetheless, a fit to these three highest energy peaks in the addback spectrum was performed and the result is shown in Fig. 3.8. The best-fit scaling value for the ^{13}N coincidence spectrum is 2.20$\pm$0.15. The uncertainty signifies the range of best fit values, as the 3 peaks were varied by eye in different ways, to fit the region of interest. The fraction of the total recoils which make it to the focal plane is given by the inverse of the scaling factor used in the best fit, 0.455$\pm$0.030. The transmission of the DRS + WGT system is then given by the ratio of the total transmission to the 6^{+} charge-state fraction (Table 3.2,

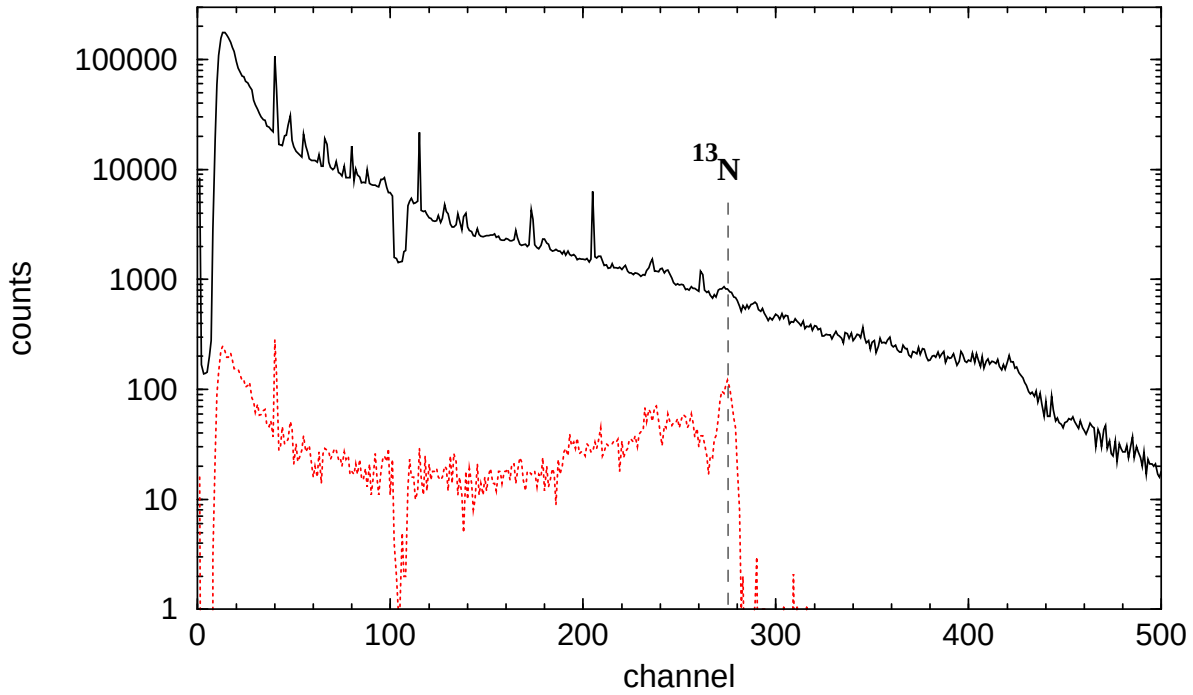

Figure 3.7: Ge clover detector addback singles spectrum (solid) and coincidence spectrum (dotted). The ^{13}N peak is at 3.50 MeV (92% branch).

$$\text{Transmission} = \frac{0.455}{0.484} = 0.94 \pm 0.06, \tag{3.7}$$

where the error bar is again an estimate based on the range of scaling parameters that would fit the Ge spectrum by eye. This does not include the uncertainty due to any varying transmission among the 3 charge states reported in Table 3.2.

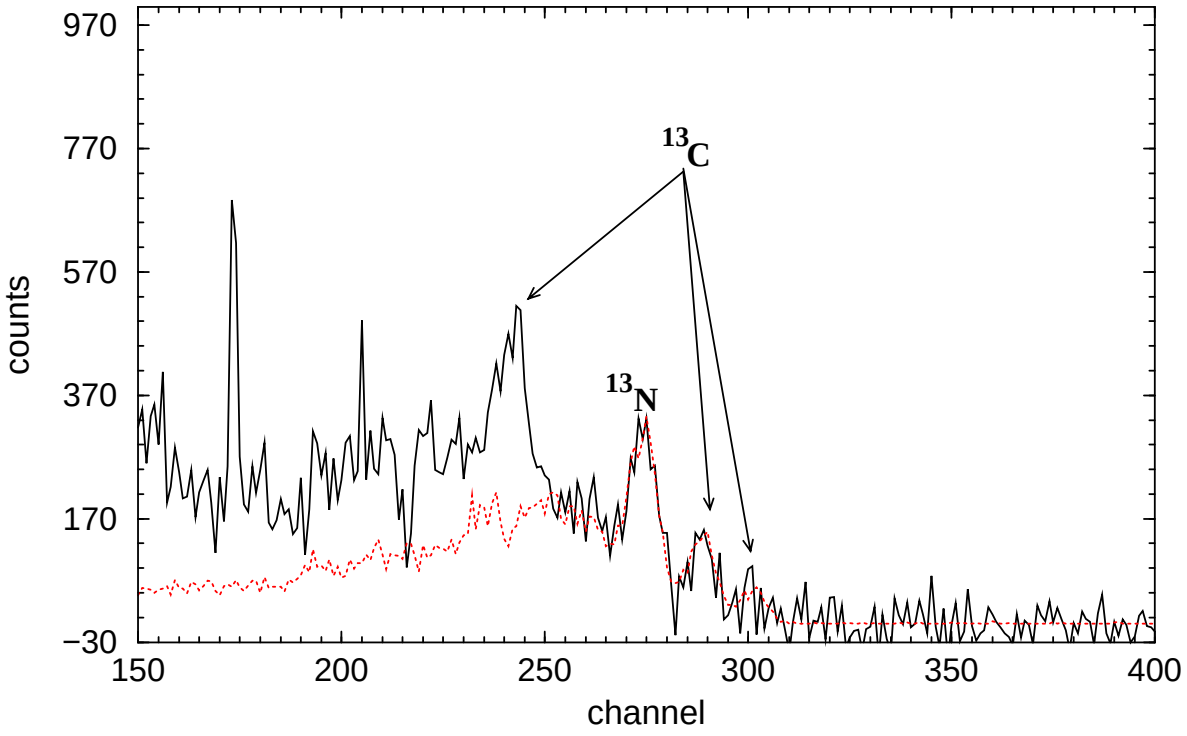

Figure 3.8: Ge clover detector addback singles spectrum with gas-off spectrum subtracted (solid). Coincidence spectrum copied and shifted to fit the ^{13}N peak and the two higher-energy ^{13}C background peaks. The ^{13}N peak is at 3.50 MeV (92% branch).

Q	E_x	$E_{r,cm}$	Γ_{cm}	J^π	ω_γ
2271.3	3061.7	790.4 ± 0.6	1.3 ± 0.4	$3/2^-$	490 ± 70

Table 3.3: Literature values for ^{24}Mg$(p,\gamma)^{25}$Al resonance parameters. Resonance energies and width from [End90]. See text for references and discussion of resonance strength. Energies are in keV, except for the resonance strength in meV.

3.2 $^1H(^{24}Mg,^{25}Al)\gamma$

To learn more about the transmission of the WGT and DRS system, the $E_{r,cm} = 0.790$ keV narrow resonance in $^1H(^{24}Mg,^{25}Al)\gamma$ was studied. The literature values for the resonance parameters are listed in Table 3.3. The goal of this study was to measure a value for the absolute resonance strength, and a high precision relative excitation function for this narrow resonance through the WGT. The thick target yield curve could reveal deviations from the expected shape given by Eqn. 1.24 by a non-unity transmission of a given charge state through the WGT and DRS. Furthermore, if some ^{25}Al recoils were not making it out of the WGT, one would expect the defect to be largest for recoils made at the very upstream regions of the WGT. Thus, if the front edge of the excitation function was not as steep as expected, it would indicate that indeed some recoils were being lost. The opening angle of the recoil cone was 0.19°, similar to the 0.22° cone from ^{1}H$(^7$Be$,\gamma)^8$B .

The resonance strength that was measured directy by [Tra75] of $\omega_\gamma = (490\pm70)$ meV is adopted here as the literature value and is listed in Table 3.3. The reaction-rate review [Ang99] includes renormalized, relative strength measurements in their recommended value of $\omega_\gamma = (532\pm41)$ meV, and was not used. Also, the value measured with a gas target at TRIUMF of $\omega_\gamma = (576\pm25(\text{stat})\pm31(\text{sys}))$ meV was not included, because the reported uncertainties appear inconsistent with the quality of the data shown in the excitation function [Eng03]. That data is being prepared for further publication [Gre05].

The $^1H(^{24}Mg,^{25}Al)\gamma$ experiment was performed with $\approx$ 1 pnA of ^{24}Mg beam on the WGT operating at $P_o = 5.00$ Torr. The DRS was tuned for the most probable charge state of Al, ^{25}Al^{9+}. The 45° monitors and IC spectra were recorded for beam energies

between 19.5 and 20.25 MeV. Also, at each energy, a short run was taken with an Al plate mounted at 0° after the WGT. This was used to perform a relative calibration of the 45° monitors to the beam current at each energy. Aside from the very narrow energy range at which the resonance is seen by the monitors, the elastic scattering cross section was expected to be nearly Rutherford and thus only change by 10% over the energy range used. Therefore, the plate measurement only leads to a small correction to the shape of the excitation function. For this experiment, the charge-state distribution of ^{25}Al recoils was measured at 2 beam energies; 20.15 MeV and 19.70 MeV (Table. 3.4). The 9^+ charge state fraction changed by only 5% over the energy range. One effect that can be difficult to account for is the non-equilibrium charge-state distribution of recoils emitted from the highest beam energy runs. In those cases, the recoils are made so close to the end of the WGT that they have not reached equilibrium upon exiting the target. This effect is mitigated by the fact that the beam used was already in the 9+ charge state, which is also the largest fraction of the Al recoils. Thus, the charge state of the recoils quickly equilibriates in the gas. Furthermore, when the reaction happens at the downstream end of the gas target, the beam has already reached its own equilibrium charge-state distribution. Thus, since the Mg and Al atoms are close in both energy and Z, the necessary shift in charge-state distribution should occur over a short distance in the WGT. Thus, the difference in recoil charge-state distributions between $E =$ 20.15 MeV and $E = 19.70$ MeV shown in Table. 3.4 is probably due to a combination of the recoil energy difference, and differences in position within the target (non-equilibrium effect).

The beam current normalization for this reaction was obtained by assuming that the elastic scattering at 45° follows the Rutherford formula ($d\sigma_r/d\Omega$). In that case, the thick target yield is given by,

$$Y \;=\; \frac{N_{Al}}{N_{mon}}\,\frac{d\sigma_r}{d\Omega}\,\frac{\Omega\, L_{mon}\,\rho}{\Phi(9^+)}, \tag{3.8}$$

where N_{Al} is the number of $^{25}Al^{9+}$ recoils detected at the focal plane, N_{mon} is the number of elastically scattered protons detected in the 45° monitors, $\mathrm{d}\sigma(\mathrm{r})/\mathrm{d}\Omega$ is the Rutherford differential cross section, ρ is the density of the gas target, Ω is the solid angle of the

q	% at 18.85 MeV	% at 18.40 MeV
6	1.1	0.4
7	4.4	7.9
8	19.0	25.7
9	45.7	43.5
10	28.0	19.4
11	3.0	3.2

Table 3.4: charge-state distribution of ^{25}Al recoils exiting the WGT with mean energy of 18.85 MeV and 18.40 MeV.

45° monitors and L_{mon} is the target length seen by the monitors. Substituting the value for ρ from Sec. 2.3.4 and the values for Ω and L_{mon} from Sec. 2.3.6 (Faraday cup) in Eqn. 3.8 gives,

$$Y \;=\; 7.2 \pm 1.1 \cdot 10^{-10}, \tag{3.9}$$

per target atom, per incident ion. This is consistent with the yield measured at TRIUMF of $(6.71\pm0.29)\cdot10^{-10}$ [Eng03].

The stopping power was determined in the same way as described in Sec. 3.1. The energy loss of the beam through the target of $\Delta E = 567\,\mathrm{keV}$ at $\mathrm{P}_o = 5.00$ Torr leads to

$$\epsilon \;=\; 90 \pm 3.5\, eV\, cm^2/10^{15}\, atoms. \tag{3.10}$$

The resonance strength was extracted from the equation for thick-target (narrow resonance) yield, Eqn. 1.24, to be,

$$\omega_\gamma \;=\; 520 \pm 90\, meV. \tag{3.11}$$

This value is consistent with the accepted literature value in Table 3.3.

The thick-target excitation function shown in Fig. 3.10 was fit using a modified version of Eqn. 3.5. To account for straggling in the target, a second width parameter (Γ_s) was included for the high energy end of the yield curve. The equation used was,

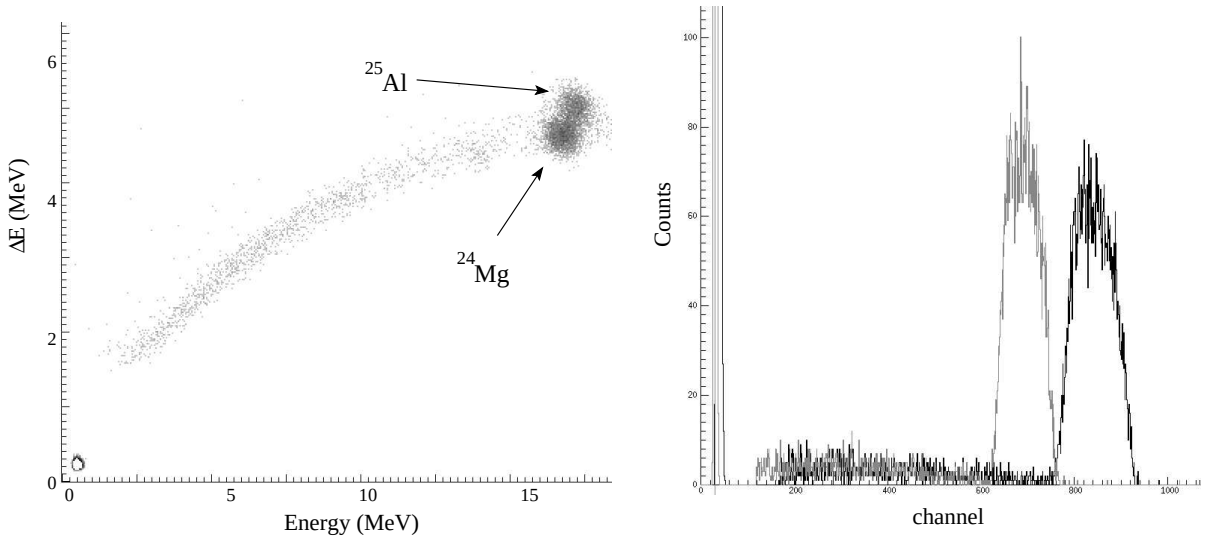

Figure 3.9: Ion counter (left) and monitor detectors (right) spectra from the $^1H(^{24}Mg,^{25}Al)\gamma$ measurement. Spectra result from a single 15 minute run.

$$Y = N\left(tan^{-1}\left(\frac{E_B - E_r}{\Gamma/2}\right) - tan^{-1}\left(\frac{E_B - E_r - \Delta}{\Gamma_s/2}\right)\right), \tag{3.12}$$

where N is a free normalization factor. The best fit parameters are $E_{r,cm} = 790$ keV, $\Gamma_{cm} = 1.57$ keV, $\Gamma_{s,cm} = 2.82$ keV, and $\Delta_{lab} = 553$ keV, in agreement with the literature values shown in Table 3.3. The energy loss is in agreement with the stopping power measurement using the Si detector. The sharp rise of the front edge of the excitation function along with the proper resonance energy and width for that edge suggests that the recoils made in the upstream portion of the target are being transmitted through the system with the same efficiency as those created in the downstream half. This is a further indication that the WGT + DRS transmission of a selected charge state is 100%.

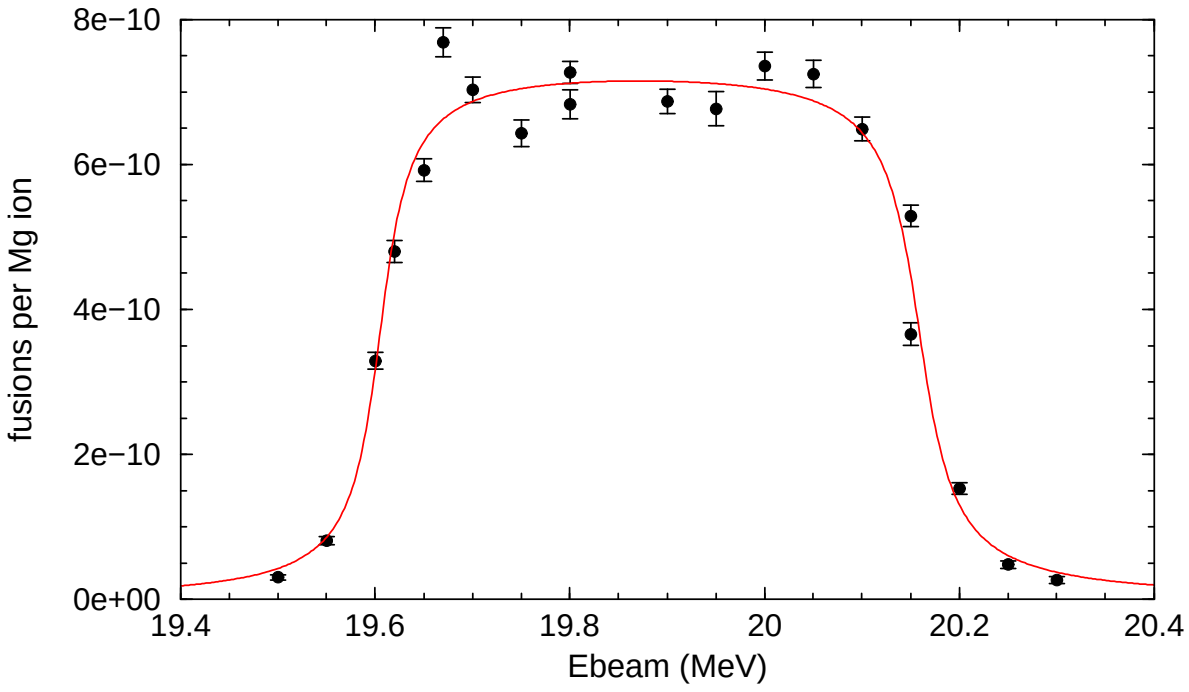

Figure 3.10: Excitation function for the $E_{r,cm} = 790$ keV resonance in $^{1}H(^{24}Mg,^{25}Al)\gamma$. Data were taken at $P_o = 5.00$ Torr. See text for fit parameters.

Chapter 4

The $^1H(^7Be,^8B)\gamma$ measurement

As stated in Sec. 1.4.2, the goal of this research program is to establish the overall normalization of the ^{1}H(^{7}Be,γ)^{8}B S factor. A secondary goal is to constrain the higher energy region of the S factor (1 <E$_{cm}$ < 2 MeV). To that end, an initial proof-of-principle, low-precision data point was taken with a ^{7}Be beam at E$_{lab}$ = 12.0 MeV (E$_{cm}$ = 1.5 MeV). To maximize the beam current on target, the beam post-stripping step was removed and the ^{7}Be^{1+} beam was tuned to the target. That adjustment to the method increased the beam current on target by a factor of 2. Because the beam was not fully stripped, the ratio of ^{7}Li to ^{7}Be in the beam was about 7-to-1. The effects of the mixed beam are discussed below in Sec. 4.3.

The ^{1}H(^{7}Be,γ)^{8}B cross section (in cm^2) was determined using the equation,

$$\sigma(E) \;=\; \frac{N_B\ R}{N_{mon}\ \Phi_{5+}\ n\ \epsilon_{DRS}}, \tag{4.1}$$

where N$_B$ was the number of ^{8}B detected in the IC at the focal plane and N$_{mon}$ was the number of counts in the 45° monitor detectors, during the same time period. Φ_{5+} was the fraction of recoils exiting the WGT in the 5+ charge state (Sec. 4.3) and n was the areal density of the WGT (Sec. 2.3.4). R was the calibration factor for the monitor detectors as described in Sec. 4.4, and ϵ_{DRS} was the DRS transmission, which was taken to be unity, as discussed in Sec. 4.7.

4.1 Ion source and beam transport

The ^{7}Be was produced at TUNL as described in Sec. 2.2. A 10-uA beam of 10 MeV protons bombarded a series of 4, 3 mm-thick Li metal targets for 7.6 days, over a 12 day period. A total of 244 mCi of ^{7}Be were produced. The first 36 mCi were processed and used for off-line source tests. The other 208 mCi were processed into a 7.5 mCi cathode and a 126 mCi cathode. The total chemistry efficiency was 63%.

The 120 mCi ^{7}Be cathode was loaded into the multi-sample sputter source along with the 10 mCi ^{7}Be cathode and a Li metal cathode. (By the start of the experiment, the strongest cathode had decayed to 100 mCi of ^{7}Be .) The pure Li cathode was used for setting up the ion source and tuning the beamlines. The ion source ^{7}Be beam output was typically $\approx$ 20 pA ^{7}Be during the 5-day ^{1}H(^{7}Be, γ)^{8}B experiment. The current tended to drop off by a factor of 2 over a 24-hour period. At that time the ion source Cs oven temperature was either raised or lowered, in opposition to its previous state. That way, the Cs vapor density and surface density were kept in an acceptable range, and the beam current recovered. The best ion source parameters and beam currents throughout the tandem system are shown in Table 4.1. The ion source ^{7}Be output was monitored every couple days with movable tape + HPGe detector system. During the 5-day period of the measurement, the total ^{7}Be output (measured at the tape system) was $\approx 5.2{\cdot}10^{13}$ $^7BeO^-$ ions, which was 0.21% of the total cathode activity. Also, during that period the transmission between the low-energy tape system and the target was 12%.

The 12.0 MeV mixed ^{7}Be /^{7}Li beam was tuned through the WGT, the DRS was set for ^{7}Be^{4+} and the fast triggers from the IC were used for tuning. The final transmission through the WGT was 50-60%. The rest of the beam was deposited on the upstream apertures. The ^{7}Be rate in the IC was about the same (within 10%) with and without the tuning aperture inserted (see Sec. 2.3.5), which indicated that the beam tune was adequate. About 15%, or $1.5{\cdot}10^7$ pps of the mixed beam on target was ^{7}Be .

Acceleration	40.0 kV, 0.30 mA	Total beam from source (RI-1)	26 μA
Extraction	13.6 kV, 0.02 mA	Mass-23 from source (RI-2)	435 pA
Ionizer	7.7 kV, 27.1 A	^{7}Be from source(tape)	32 pA
Cathode wheel	4.68 kV, 0.38 mA	Mass-23 into tandem (13-1)	200 pA
Cs oven	170°C	Mass-7 at target beamline (17-2)	28 pA
———	———	^{7}Be on target	3.2 pA

Table 4.1: Best ion source parameters (left) and beam currents throughout tandem system (right) during the ^{1}H(^{7}Be, γ)^{8}B measurement. Faraday cups are labeled in parentheses. The ^{7}Be beam source output was measured using a Ge detector and movable tape system. The beam currents at RI-2 and 13-1 are approximate, as the beam was not expected to be focused at those locations.

4.2 Energetics

The energy loss of the 12.0 MeV ^{7}Be beam in the $P_o = 5.00$ Torr gas target was measured with a Si detector to be 73±1 keV, which made the beam energy at the center of the target $E_{lab} = 11.96$ MeV. The energy loss of the ^{8}B recoils was determined using a ^{10}B beam of the same E/A (ie. velocity). The ^{8}B energy loss through the whole target was thus determined to be 126±5 keV. Considering the linear and nearly constant (to 0.6%) ^{1}H(^{7}Be, γ)^{8}B cross section throughout the target and the ^{7}Be and ^{8}B energy losses, the average energy of the ^{7}Be beam in the target and of the ^{8}B recoils exiting the target were $\bar{E}_{^{7}Be} = (11.96 \pm 0.02)$ MeV and $\bar{E}_{^{8}B} = 10.47$ MeV. The ^{8}B had a 1.5% kinematic range due to the kinematic variations from reactions throughout the target and from straggling effects.

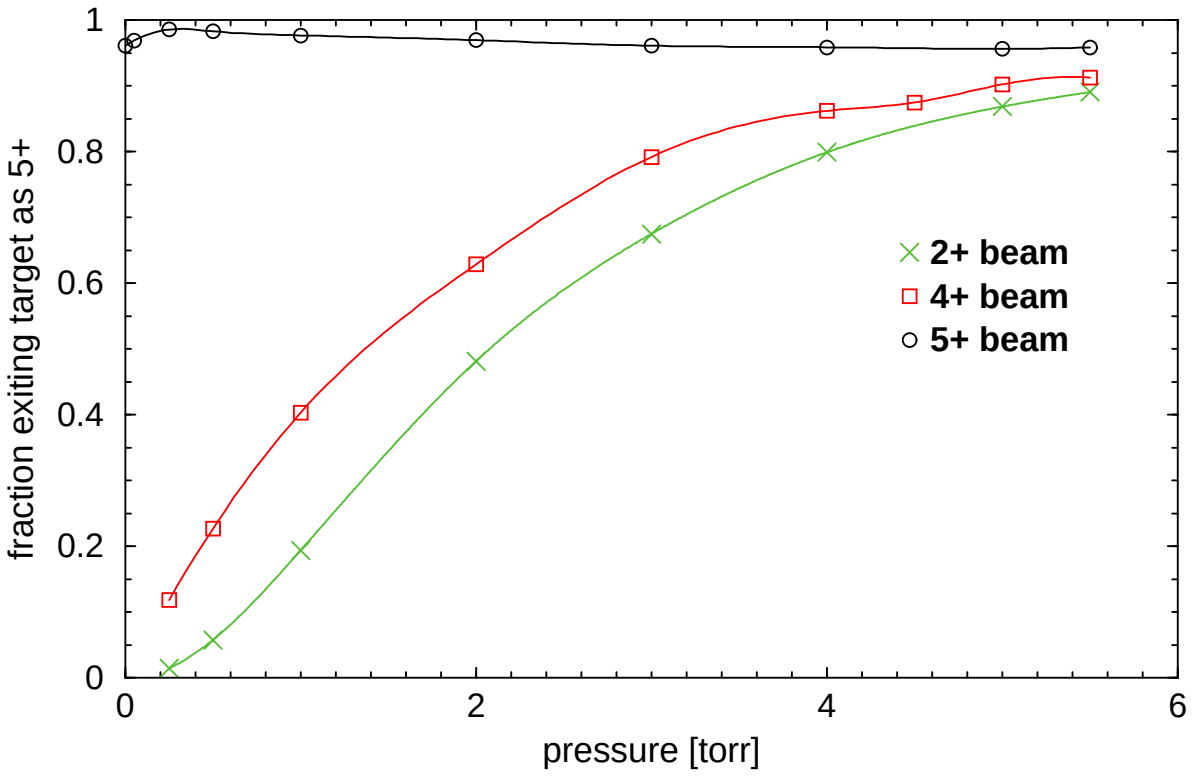

Figure 4.1: Non-equilibrium 5+ charge-state fraction for 12.9 MeV $^{10}B^{2+,4+,5+}$ on the WGT. Statistical uncertainties are 1%. The values are tabulated in Table A.3. The velocity of the ^{10}B was equivalent to that of the ^{8}B recoils. Lines are to guide the eye. The downturn near 0 Torr is likely due to charge exchange in residual gas between the beam analyzing magnet and the WGT. Its effect on the charge-state distribution, averaged over the length of the target was <0.2% (see text).

4.3 Charge states

The experimentally determined value for the reaction cross section, Eqn. 4.1 is inversely proportional to the charge-state fraction selected by the DRS (Φ_{5+}). Therefore, the recoil charge-state distribution was determined for both a fully stripped $^{7}Be^{4+}$ beam (needed for fully stripped ^{7}Be beams) and for a $^{7}Be^{1+}$ beam (needed for the present measurement). The method for determining these non-equilibrium charge states is described in more detail in Sec. A.2.

When a $^{7}Be^{4+}$ beam particle captured a proton in the WGT, it naturally formed $^{8}B^{5+}$. Those ^{8}B ions moving through the target quickly equilibriated to a beam of 95.8% $^{8}B^{5+}$ (circles in Fig. 4.1). The equilibrium charge-state distribution for $^{8}B^{5+}$ ions created at various points within the target was determined by measuring the distribution of a

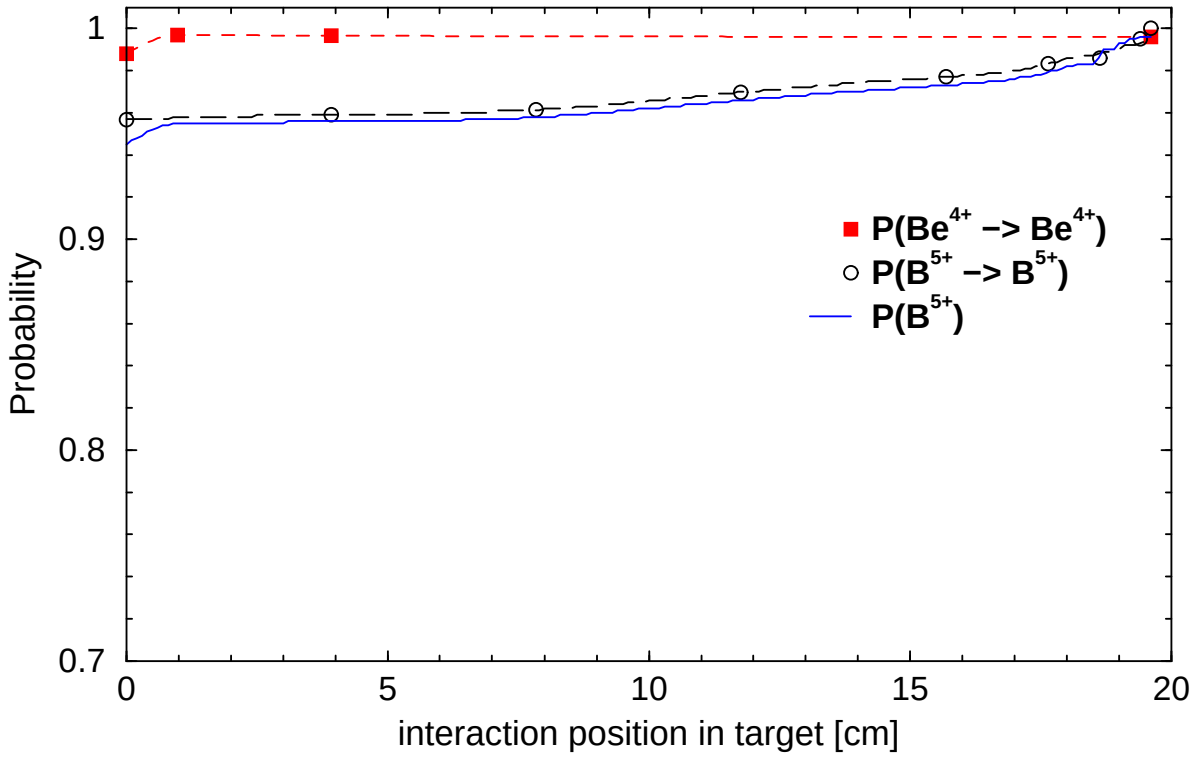

Figure 4.2: Probability for a $^{7}Be^{4+}$ initial beam to produce $^{8}B^{5+}$ ions exiting the WGT (solid blue line). The average value for probability is 0.964 (96.4%).

$^{10}B^{5+}$ beam passing through the WGT at various pressures (densities). The result is shown in Fig. 4.1. The $^{7}Be^{4+}$ beam also quickly equilibriates to its 99.6% 4+ charge-state distribution. The resultant 5+ fraction of the ^{8}B recoils exiting the WGT (at $P_o = 5.00$ Torr) was then given by averaging the formula,

$$\begin{aligned} P(B^{5+}) &= P(Be^{4+} \rightarrow Be^{4+})\, P(B^{5+} \rightarrow B^{5+}) \\ &+ P(Be^{4+} \rightarrow Be^{3+})\, P(B^{4+} \rightarrow B^{5+}), \end{aligned} \tag{4.2}$$

over the length of the target, where the probability for a $^{7}Be^{4+}$ to remain 4+ ($P(Be^{4+} \rightarrow Be^{4+})$ was 0.996 or higher throughout the target. The constituent probability functions in Eqn. 4.2 were determined by the non-equilibrium charge-state distributions described above. The first term in Eqn. 4.2 is shown graphically in Fig. 4.2. The second term contributes $< 0.1\%$ to the distribution and thus averaging Eqn. 4.2 over the length of the target, $\Phi_{5+} = (0.964 \pm 0.010)$ or 96.4%.

The B^{5+} beam shows a low-pressure down-turn in the 5+ charge state in Fig. 4.1.

That effect was likely caused by residual gas (other than H_2) between the analyzing magnet and the target. The effect of that down-turn is less than 0.2% on the charge-state of the beam, averaged over the length of the target. In Fig. 4.2, Eqn. 4.2 and Eqn. 4.3, that downturn was removed, since in those cases the "low-pressure" ^{8}B charge-changing probabilities describe recoils made at the downstream end of the WGT (thus passing through a small amount of gas), where that residual-gas effect is not present.

Since a $^7Be^{1+}$ beam was used in the present work, Eqn 4.2 had to be expanded to include contributions to Φ_{5+} from beam charge states other than $^7Be^{4+}$ present within the target. Φ_{5+} was then determined by averaging the probability function,

$$\begin{aligned} P(B^{5+}) = \; & P(Be^{1+} \rightarrow Be^{4+})\, P(B^{5+} \rightarrow B^{5+}) \\ + \; & P(Be^{1+} \rightarrow Be^{3+})\, P(B^{4+} \rightarrow B^{5+}) \\ + \; & P(Be^{1+} \rightarrow Be^{2+})\, P(B^{3+} \rightarrow B^{5+}) \\ + \; & P(Be^{1+} \rightarrow Be^{1+})\, P(B^{2+} \rightarrow B^{5+}), \end{aligned} \tag{4.3}$$

over the length of the target. The non-equilibrium charge-state distributions were measured for the most important terms in Eqn. 4.3, using beams of $^7Be^{1+}$ (Fig. 4.3), $^{10}B^{2+}$, $^{10}B^{4+}$ and $^{10}B^{5+}$ (Fig. 4.1 and Table A.3). The terms $P(B^{3+} \rightarrow B^{5+})$, $(Be^{1+} \rightarrow Be^{3+})$, $(Be^{1+} \rightarrow Be^{2+})$, and $(Be^{1+} \rightarrow Be^{1+})$ were extrapolated based on those same measurements and the trends from the B charge-state measurements. The sum and constituent terms of Eqn. 4.3 are shown in Fig. 4.4. Averaging Eqn. 4.3 over the length of the target gave

$$\Phi_{5+} = (0.944 \pm 0.020), \tag{4.4}$$

which was used in Eqn. 4.1 to determine the cross section.

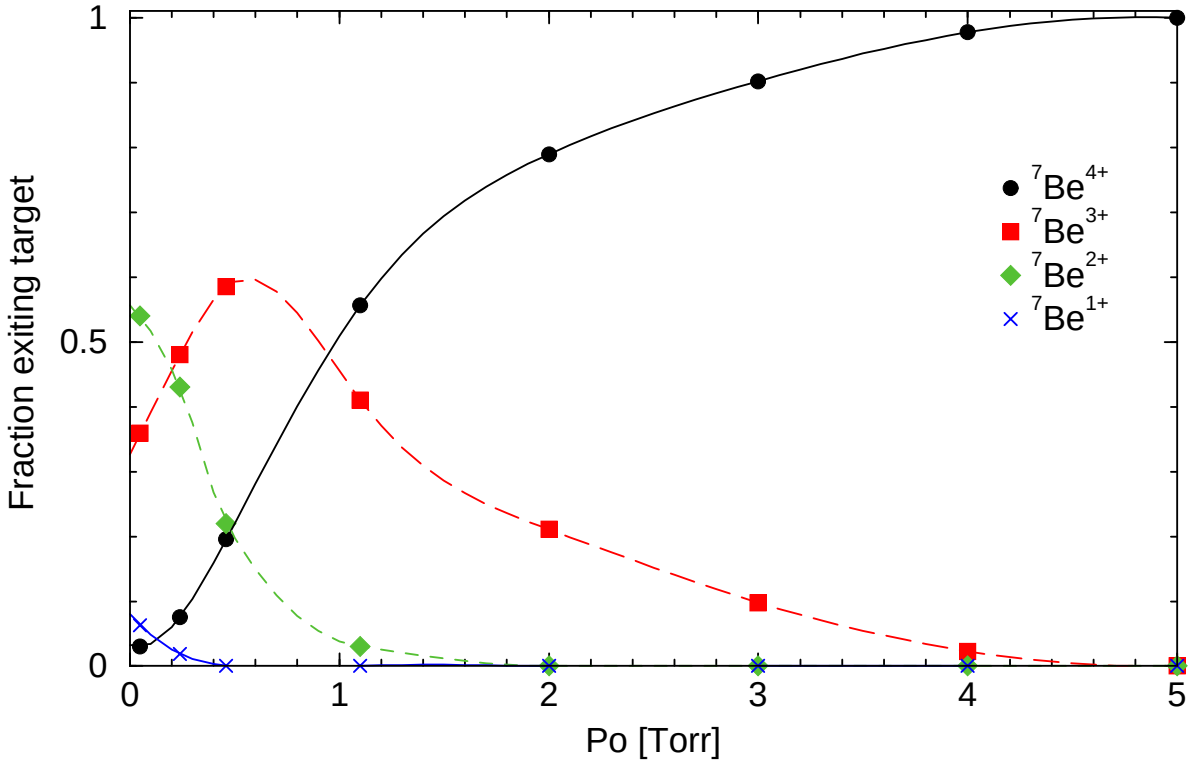

Figure 4.3: Non-equilibrium charge-state distribution for $^{7}Be^{1+}$ beam on WGT. Only the 4+ exiting beam was measured at the DRS focal plane. The other, less significant, charge states were extrapolated using the 4+ data and the scaled trends from the B charge-state measurements.

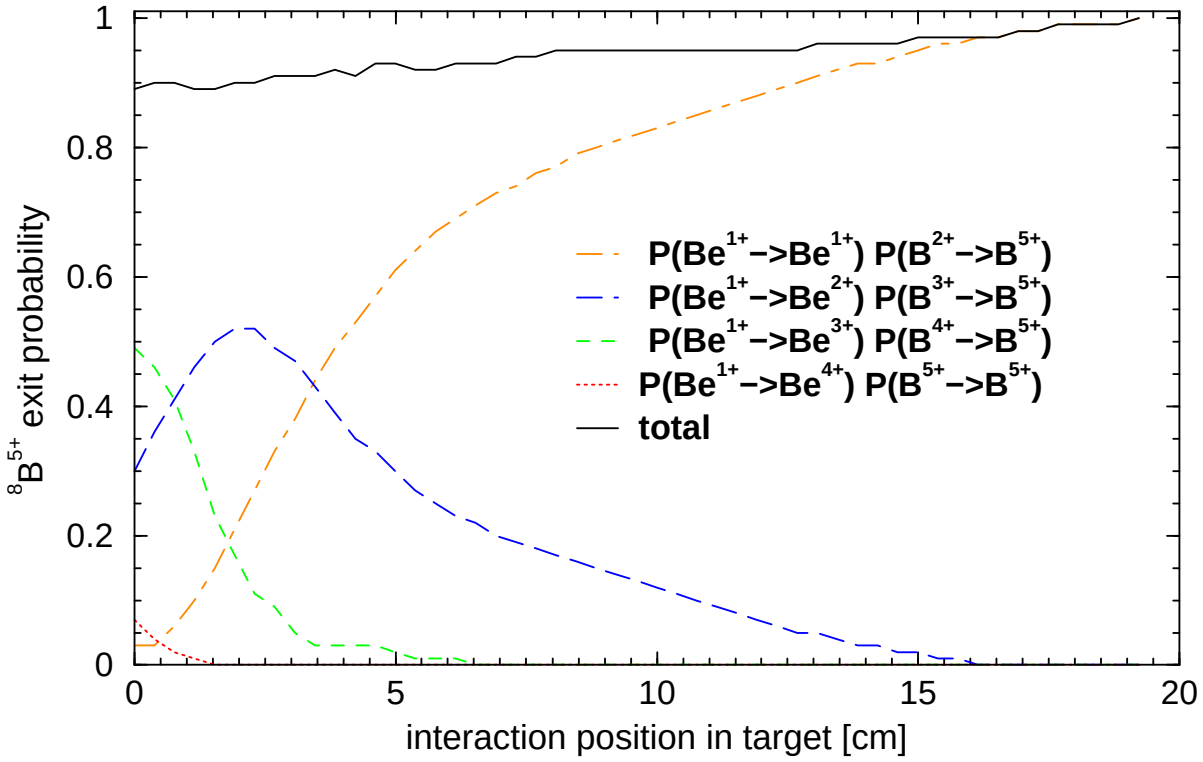

Figure 4.4: Probability for a $^7Be^{1+}$ initial beam to produce $^8B^{5+}$ ions exiting the WGT (solid blue line). The average value for probability is 0.94 (94%).

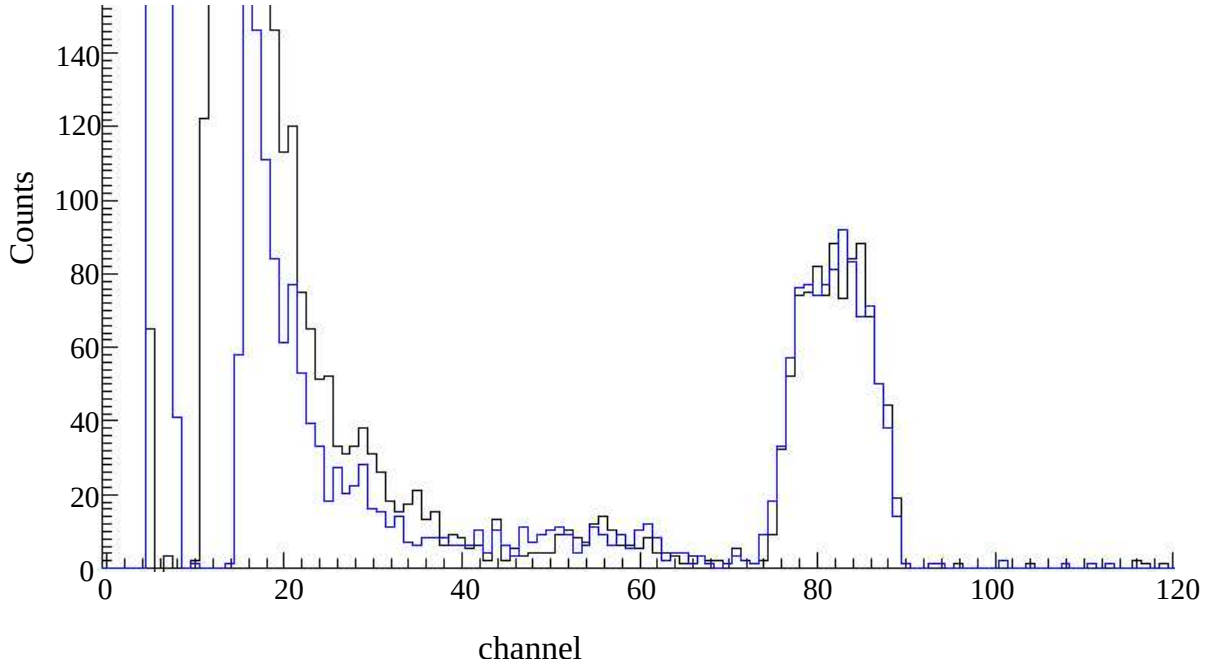

Figure 4.5: Sample 45° monitor spectra. The data have been gain matched and compressed by a factor of 5 from the original 2048 channel ADC output, and the proton peak is at 2.6 MeV. This sample represents 60% of the total data.

4.4 Beam current normalization

The cross section formula used, Eqn. 4.1, is proportional to the beam current normalization factor, R. Where R was defined as the ratio of the total peak counts in the sum of the +45° and -45° monitors to the number of beam ions that had passed through the target during the same period of time. Since protons scattered from ^{7}Be and ^{7}Li were not separated in the monitor detector spectra (Fig. 4.5), R was sensitive to both the ^{7}Be beam current, and the ratio of ^{7}Be to ^{7}Li in the beam. Therefore, R was measured every hour, to account for any change in the ^{7}Be to ^{7}Li ratio in the beam. To determine R, an Al plate was inserted at $\theta_{lab} = 0°$ downstream of the last pumping stage of the WGT. The monitor detector spectra were stored, while the beam deposited in the plate. Sample monitor detector spectra are shown in Fig. 4.5. This procedure was repeated for 10 minutes every hour, during the ^{1}H(^{7}Be, γ)^{8}B experiment. A total of 3 different plates were used over the 4-day experimental period to check for temporal changes in the ^{7}Li-to-^{7}Be ratio. After the experiment had ended the plates were removed, and the ^{7}Be activity was measured using a Ge detector. The resulting plate activities, and mon-

plate	^{7}Be ions implanted	monitor counts	R
1	$2.32{\cdot}10^{11}$	223	$(0.96{\pm}0.08){\cdot}10^{-9}$
2	$9.52{\cdot}10^{10}$	95	$(1.0{\pm}0.1){\cdot}10^{-9}$
3	$2.28{\cdot}10^{11}$	249	$(1.1{\pm}0.1){\cdot}10^{-9}$

Table 4.2: Monitor detector calibration data. R is the ratio of monitor detector counts to the number of ^{7}Be ions implanted in the Al plate during the same time period. THe combined statistical uncertainty from the monitor counts and HPGe detector counts are shown.

itor counts during plate bombardment are listed in Table. 4.2. The reproducibility of R indicated that the ^{7}Li-to-^{7}Be ratio was constant over the duration of the experiment.

The value of R used in the cross section determination was an effective value taken as the mean value from all three plates weighted by the number of ^{8}B recoils detected during the time period around which each plate was used. The weighted mean value of R used in the cross section determination was,

$$R \;=\; (9.96 \pm 0.10) \cdot 10^{-10} \;\frac{\text{monitor counts}}{^7\text{Be beam on target}}. \tag{4.5}$$

Since the beam intensity was constantly monitored with the 45° detectors, total beam current fluctuations on any time scale were accounted for. Also, the hourly sampling of the beam with the plate, accounted for any net change in the ^{7}Li-to-^{7}Be ratio on the order of an hour or longer. Since the ^{7}Be and ^{7}Li were dissolved in HCL and deposited in the cathode together, there was no reason to suspect significant short-term spikes in that ratio. No fluctuations in R were evident in the data (Table 4.2).

4.5 DRS

It was shown during the $^{12}C(p,\gamma)^{13}N$ tests presented in Sec. 3.1 that a DRS beam rejection of $4 \cdot 10^{-11}$ could be achieved without losing recoils. Considering the large cross section for ^{1}H(^{7}Be, γ)^{8}B , such rejection was not necessary. The DRS was run with 80 kV potential difference on the velocity filter plates, and with the slits after each velocity filter all the way open (±2.5 cm). The beam rejection was then $4 \cdot 10^{-9}$ for ^{7}Be and $5 \cdot 10^{-9}$ for

^{7}Li. A 100 kV potential difference was tried, but the amount of scattered being incident on the IC increased. This effect was likely due to beam scattering off the velocity filter high-voltage plates, as the beam was highly diverted off-axis due to the large relative velocity difference between ^{7}Be and ^{8}B (see Eqn 2.25). The suppression was adequate to eliminate background in the IC spectra region of interest, and could have been enhanced by moving in the VF slits. As can be seen in Fig. 4.6, only low energy scattered ^{7}Be and ^{7}Li made it into the IC.

The DRS was tuned for charge state $q = 5.03$ and E =10.43. All the other DRS parameters were identical to those reported in Sec. 2.4.3.

4.6 Focal plane events

At the DRS focal plane, the IC was fitted with a 600 μg/cm^2 polypropylene window and filled with 22 Torr isobutane gas. The three anode signals were gain-matched and the signals from each were stored separately in the data stream. The gas pressure was chosen so that the ^{8}B recoils would stop in the middle of the third anode. The ^{7}Be and ^{7}Li beams continued into the back wall of the IC. The system was set up such that the plot of the energy loss in the first two anodes versus the total energy loss in the IC would give the best signature of ^{8}B recoils. Thus the signals from the first two anodes were summed in software and considered ΔE and the sum of all three anodes was used for the full energy, E. Example spectra are shown in Fig. 4.6.

The possibility of background events in the ^{8}B region of interest due to ^{7}Li was studied by running an intense (1 nA) ^{7}Li beam through the WGT and acquiring data for 45 minutes, which lead to an equivalent amount of ^{7}Li beam through the target as occurred during the ^{1}H(^{7}Be, γ)^{8}B measurement. As can be seen in Fig. 4.7, no background events were present in the region of interest. Also, the E = 12.0 MeV ^{7}Be beam energy was above the E = 9.4 MeV threshold for $^2H(^7Be, n)^8B$, which was expected to occur due to the 0.012% ^2H abundance in natural hydrogen [Lid90]. That background was tested for by running the experiment for 5 minutes with $P_o = 5.00$ Torr D_2 gas instead of H_2 in the WGT. As expected, a small ^{8}B group containing 35 counts was present in the ΔE vs. E

spectrum, but zero counts fell inside the ^{1}H(^{7}Be, γ)^{8}B region of interest (Fig. 4.7). Those 5 minutes of running with pure D_2 were equivalent to 50 days of running with the natural abundance hydrogen. Therefore, ≈ 3 ^{8}B counts were expected from $^{2}H(^{7}Be, n)^{8}B$ during the ^{1}H(^{7}Be, γ)^{8}B experiment, and <0.07 counts were expected to fall in the region of interest. Finally, 15 hours of background IC data were recorded, without beam on target. Again, no counts were present in the region of interest (Fig. 4.8).

Because the bulk of the ^{7}Li and ^{7}Be beams was blocked by the DRS, only low-energy scattered beam particles were detected in the IC. Since the velocity filter slits were all the way out, the beam could scatter from many positions in the DRS, and thus cause various patterns of low energy background in the IC spectra. That effect is evident in Fig. 4.6 (top) which shows 2 groups of scattered ^{7}Be beam from two different days of the experiment. Between those days, the DRS settings were changed slightly (small change in q), leading to a different low-energy group of scattered beam at the focal plane. Fig. 4.6 (bottom) shows only the data taken before the change in DRS settings. In either case, the ^{8}B group was separated from the scattered ^{7}Be and ^{7}Li . The total number of ^{8}B counts from ^{1}H(^{7}Be, γ)^{8}B was determined by analyzing the data set corresponding to each background group separately.

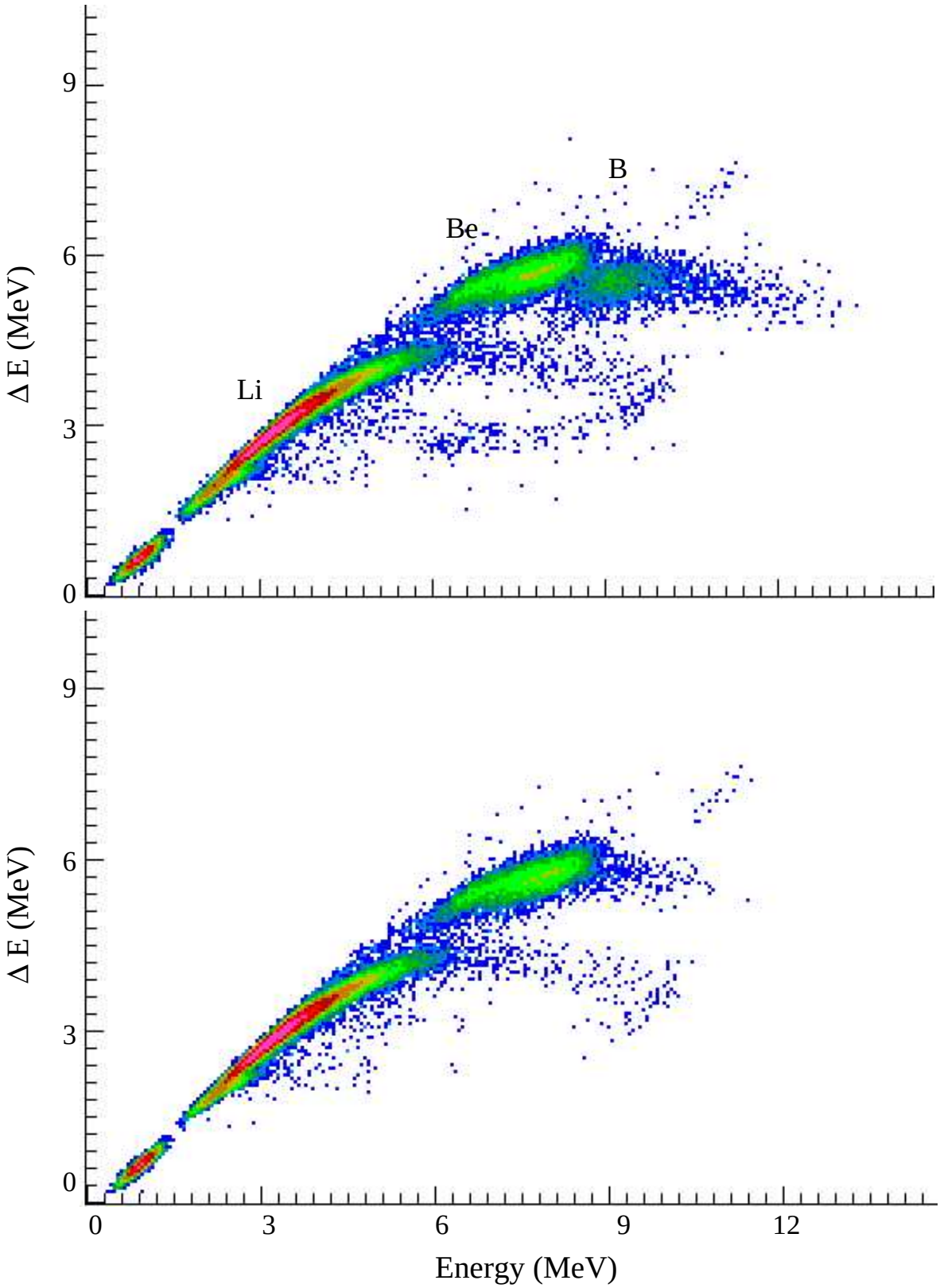

Figure 4.6: Ion counter ΔE vs. E data for ^{1}H(^{7}Be, γ)^{8}B . The top plot shows all the data (22 ^{8}B counts circled), and the bottom plot shows the first 85% of the data (see text)

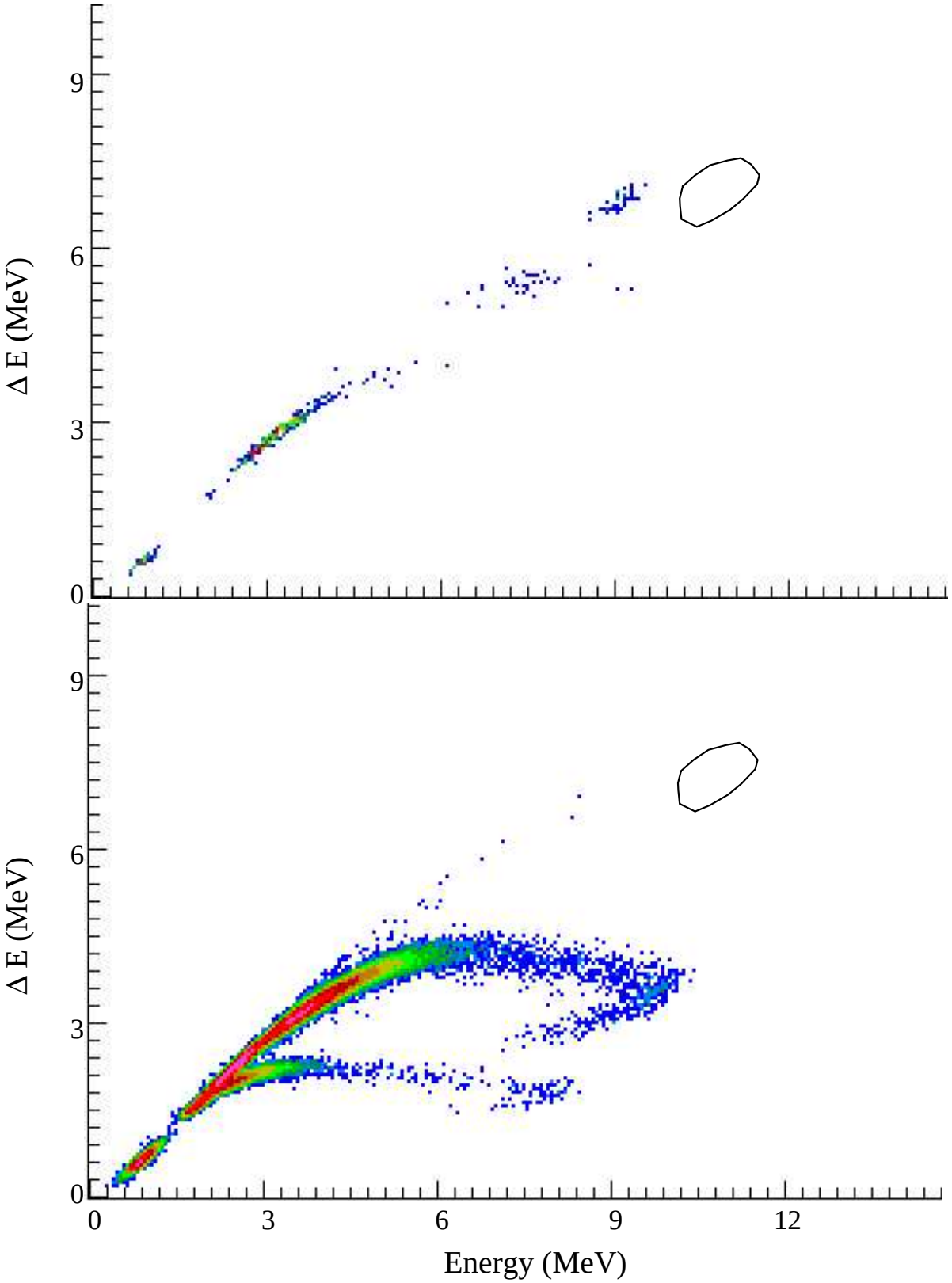

Figure 4.7: IC beam-induced background tests. Top spectrum is from running with D_2 gas and top group is ^{8}B from $^2H(^7Be, n)^8B$. The bottom spectrum is from running with 1 nA ^{7}Li beam. The lower ΔE band is ^4He from $^1H(^7Li, \gamma)^8Be \rightarrow 2\,^4He$. A black oval marks the ^{1}H(^{7}Be, γ)^{8}B recoil region of interest.

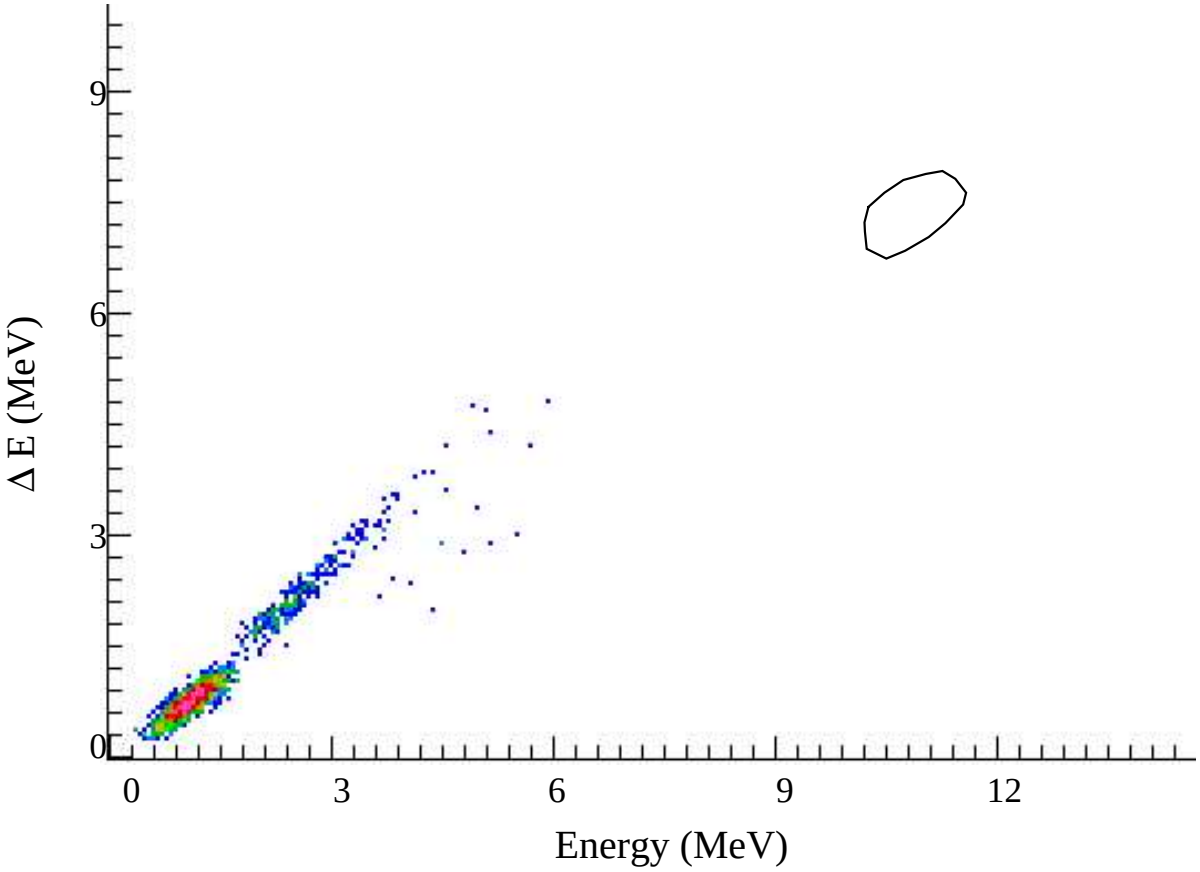

Figure 4.8: IC spectra for a 15-hour background run, with no beam present.

4.7 Cross section result and error budget

The total ^{7}Be on target during the capture measurement (63.1 h live time) was given by $N_{mon}/R = (3.46 \pm 0.36) \cdot 10^{12}$ ^{7}Be particles, the areal target density was $n = (6.27 \pm 0.18) \cdot 10^{18}$atoms/cm^2 and the total number of $^8B^{5+}$ recoils detected was 22. Using Eqn. 4.1, the cross section was determined to be,

$$\sigma(E_{cm} = 1.502) = (1.12 \pm 0.27)\,\mu b, \tag{4.6}$$

where the error was mostly due to the low counting statistics (22 counts). That value for the cross section agrees with the literature value of $0.91 \pm 0.03\,\mu$b. The literature value was interpolated from the 1.4< E_{cm} <1.6 MeV data points reported by [Jun03]. The S factor for the present work, defined by Eqn. 1.18, was determined to be $S(\mathrm{E}_{cm}{=}1.502) = (34.9 \pm 8.4)$ eV·b. Using the extrapolation to E = 0 from [Jun03] gives $S(0) = (26.8{\pm}6.5)$ eV·b for our measurement.

Table 4.3 lists the sources of error considered in this result. All errors reported are $1\,\sigma$ or 68% confidence limits. The total systematic uncertainty was 8% and the total statistical uncertainty was 23%. The 9% statistical uncertainty in R was from the number of monitor counts during the plate bombardments (318 counts) and the number of counts during the HPGe activity measurement. The 5% systematic uncertainty in R was from the Ge detector efficiency. The DRS and WGT were designed to have 100% transmission (ϵ_{DRS}), for a given charge state. However, due to the $\approx$ 10% experimental limit on the transmission from both the $^{12}C(p,\gamma)^{13}N$ and $^{24}Mg(p,\gamma)^{25}Al$ cross section measurements (Chapter 3), and the fact that $^{12}C(p,\gamma)^{13}N$ reaction was a kinematically worse case than ^{1}H(^{7}Be,γ)^{8}B , a transmission value of $0.96^{+.04}_{-.06}$ was accepted.

quantity	value	stat. (%)	sys. (%)
N_B (counts)	22	21	—
N_{mon} (counts)	3446	1.7	—
R (monitors/ 10^{10} ^{7}Be)	9.96	9	5
n (10^{18} atoms/cm^2)	6.27	—	3
Φ_{5+} (fraction)	0.944	—	2.3
ϵ_{DRS} (fraction)	0.96	—	$+4/-6$
σ (μb)	1.12	23	$+8.7/-7.4$

Table 4.3: Cross section error budget showing statistical and systematic contributions to the total uncertainty. ϵ_{DRS} is the DRS transmission for the chosen charge state. See text for further explanation.

Chapter 5

Conclusions

An experimental program has been established to study proton-fusion experiments in inverse kinematics at the HRIBF at ORNL using a windowless gas target (WGT) and the Daresbury Recoil Separator (DRS). The perforance of the target and separator have been well characterized using a variety of experiments with stable beams including ^{12}C, ^{19}F and ^{24}Mg. For example, the areal density of hydrogen in the target was determined to 3% accuracy. This well-characterized system was used to measure accurate stopping powers for many elements in H_2 gas for the first time.

The first cross-section measurement for a proton-fusion reaction with a radioactive-ion beam at ORNL, ^{1}H(^{7}Be, γ)^{8}B, was performed using the WGT and the DRS. The ^{7}Be was produced at TUNL, chemically separated at ORNL, and accelerated by the HRIBF tandem accelerator to an energy of 12 MeV. An average ^{7}Be beam current of 2.5 ppA bombarded the windowless gas target for a period of 3 days. Recoiling ^{8}B nuclei were efficiently collected using the DRS and were clearly identified in the IC. The cross section was determined to be $\sigma(E_{cm} = 1.502) = (1.12 \pm 0.27)\,\mu$b, leading to $S(0) = (26.8 \pm 6.7)$ eV·b, where a 5% uncertainty due to the extrapolation to zero has been added in quadrature to the cross-section uncertainty. This value is shown with other literature values for the S-factor in Fig. 5.1.

To measure the ^{1}H(^{7}Be, γ)^{8}B cross section to 5% accuracy, both the statistical and systematic uncertainties will have to be reduced. The most significant systematic uncertainties are from the Ge detector efficiency for the beam-current normalization (R),

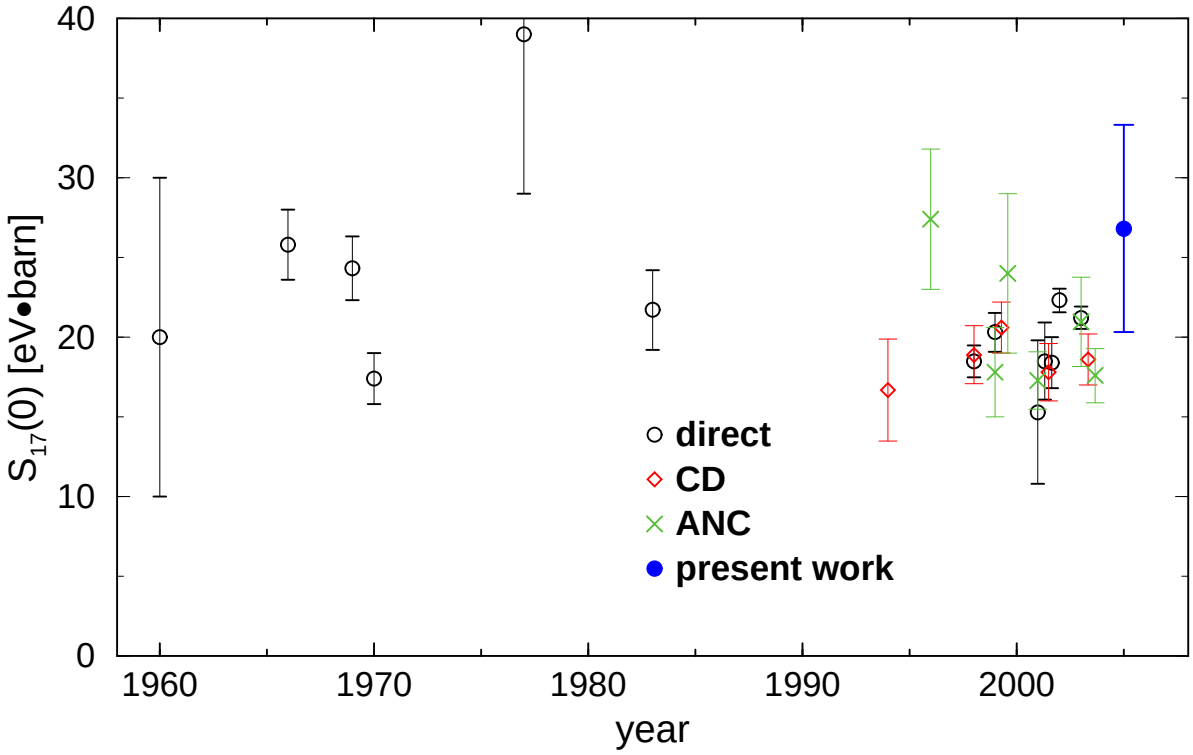

Figure 5.1: Plot of $S(0)$ showing direct and indirect measurements. The blue diamond represents the present work.

and the DRS efficiency. Arangements have been made to analyze the ^{7}Be implanted Al plates off-site to an accuracy of 1%, and thus reduce the contribution of R to the overall systematic error in σ(E) to 1%. The DRS and WGT were designed to ensure a 100% efficiency ($\epsilon_{DRS} = 1.0$) for the low energy ^{1}H(^{7}Be, γ)^{8}B reaction. However, this has only been confirmed to be >0.9 using stable beams. To decrease the uncertainty in ϵ_{DRS}, more precise stable measurements should be made using reactions with precisely known cross sections. One candidate is the $E_{r,cm} = 0.790$ keV resonance strength in $^{24}Mg(p,\gamma)^{25}Al$, which was described in Sec. 3.2. That resonance strength is known to 5% accuracy. Applying the Faraday cup technique described in Sec. 2.3.6, a 5%-accurate measurement of the resonance strength could be made. The 2.3% systematic uncertainty in Φ_{5+} could also be reduced by measuring all of the ^{7}Be charge state contributions (instead of extrapolating the lower charge states), using a fully stripped (^{7}Be^{4+}) beam, or measuring both ^{8}B^{5+} and ^{8}B^{4+} recoils, in turn, at the focal plane.

The most significant sources of statistical uncertainty are from the number of ^{8}B re-

coils detected at the focal plane (N_B), and the number of monitor counts (N_{mon}) detected during the monitor detector calibration (R) measurements. If the beam current is increased to reduce the uncertainty in N_B to 5%, then the statistical uncertainty in R will scale to 1.2% and the total uncertainty of a cross section measurement will be 9%. The ^{8}B statistics have already been maximized by running at a high energy and using a mixed ^{7}Li + ^{7}Be beam. To further increase the statistics, either the ^{7}Be production (150 mCi/week), chemistry efficiency (60%), or the source efficiency (0.3%) will have to be increased. The ^{7}Be production at TUNL does not have much more room for improvement, other than by increasing the bombardment time. However, once the High Power Target Laboratory (HPTL) comes on-line at HRIBF, hotter cathodes might be made at ORNL. Also, the hot chemistry laboratory will probably not be able to handle much more activity at a given time than it did for the present work. So if more activity is to be handled, it would likely be done in batches. The chemistry efficiency might be improved if the causes for the losses were again studied systematically using low activity samples. There is room for improvement in the 0.2% ^{7}Be-sputter source efficiency. For instance, after each ^{7}Be experiment, $\approx$ 50% of the ^{7}Be activity has remained in the cathode, un-sputtered. Therefore, further optimizing the design of the active cathode volume to match the Cs sputter pattern should increase the source efficiency. Also, the Cs-vapor transfer system in the source has proved to be unstable, and should be examined. Also, the transmission between the source and the tandem should be studied. The tight collimation on the 103° isobar separator (between the source and the tandem) is not necessary for the ^{7}Be source operation, and a significant portion of the beam may be depositing on that collimator. Therefore, removal of that collimator, and careful study of the ion optics, could lead to an increase in the beam current on target. These ^{7}Be-beam studies could lead to beam currents of $>1{\cdot}10^8$ pps ^{7}Be on target, and then a 5% statistical uncertainty in σ(E).

The above improvements in the system could decrease the systematic uncertainty in R to 1.6% and the uncertainty in ϵ_{DRS} to 3%. Combined with a 5% statistical uncertainty, this would lead to a 7% accurate ^{1}H(^{7}Be, γ)^{8}B cross section measurement.

Appendix A

Equilibrium charge-state distributions in solids and gasses

A.1 Solid Foils

Measuring proton capture reactions in inverse kinematics requires the knowledge of the charge-state distribution of the recoiling nuclei. If all the reaction products of a given charge state are accepted by the separator + target system, then the charge state fraction is equivalent to the detector efficiency. One way to ensure a constant and well known charge-state distribution is to put a solid foil between the gas target and the separator. Either a plastic or metal foil can be used. If the thickness of the foil is greater than some minimum thickness (n_{min}) then the charge-state distribution of the ions exiting the foil will be independent of the incoming charge-state distribution.

This method was not used in the above work for numerous reasons. First, the addition of a foil would add energy and angular straggle to the recoils and cause scattering of both the recoils and beam particles. These effects could degrade the DRS acceptance and the rejection of beam particles. To minimize these effects a thin foil would have to be used; for example, a 20 μg/cm^2 C foil. However, the foil area would have to be ≈ 2 cm diameter in order to allow the recoils to pass freely. Ensuring that a foil of that size remains in tact and free of pinholes during a long run would be difficult. Finally, in the case of ^{1}H(^{7}Be, γ)^{8}B , the recoils would be roughly 90% 5^+ and 10% 4^+ after

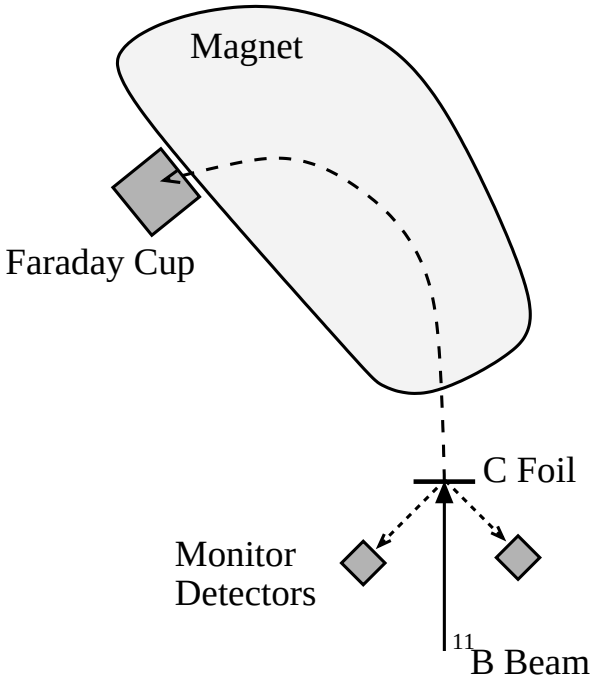

Figure A.1: Experimental setup for measuring charge-state distributions at Yale University.

leaving the gas target and roughly 55% 5^+ and 45% 4^+ after exiting the foil. Thus, since the experiment was limited by statistics, including the C foil would reduce the overall precision of the measurement.

Also for ^{1}H(^{7}Be, γ)^{8}B , the charge-state distribution of ^{7}Be ions leaving the gas target could be useful for normalizing the beam current using a Faraday cup. In the present work, a Faraday cup was not used, because tthe 53 day half-life of ^{7}Be allowed the integrated beam to be deposited on a metal plate and then counted with a Ge detector.

Nonetheless, the equilibrium charge-state distributions for Be and B beams exiting C foils was measured. This data might be useful for future experiments with ^{7}Be beams, or even for ^{1}H(^{7}Be, γ)^{8}B at different energies. Also, a limit on the minimum thickness of C needed to reach equilibrium was measured. The charge-state measurements were carried out at Wright Nuclear Structure Laboratory at Yale University. The experimental

setup is shown in Fig. A.1. C foils were used as the equilibriating substrate. Past experiments have shown that the final distribution is highly insensitive to the solid substrate used [Wol68]. Also, it has been shown that the charge-state distribution is dependent on the atomic number and velocity of the ion, but not its mass [Wol68, Shi89]. Thus, ^{9}Be and ^{10}B beams were used. The beams were produced with a sputter source and accelerated through a tandem Van de Graff accelerator. The beam was then tuned through the C foils and into the focal plane of the Engle split-pole spectrometer. An Al plate was mounted at one end of the spectrometer focal plane, such that the beam current from one charge state at a time could be measured at the focal plane. The plate was connected to a beam current integrator which was carefully zeroed and calibrated. Typical beam currents were a few pnA. The plate was not electron suppressed. Therefore there could be a small difference in beam current integration from differences in secondary electron emission due to differences in initial charge state. However, considering that electrons are emitted while the ions travel a distance $\gg$ the thickness required to achieve an equilibrium charge state (see below), this effect is very small. The charge-state distributions were measured by adjusting the Enge magnet setting to center each charge state on the Al plate for counting. The relative incoming beam current was monitored with collimated Si surface barrier detectors at $\pm$30 deg, which generally contained about 10,000 counts per detector per run.

The charge-state distributions were measured for all states comprising $>$ a few % of the total beam. The other states were extrapolated using a Gaussian fit to the charge-state distribution. For the highest E/A data, a skewed Gaussian was used to compensate for the saturation of maximally ionized nuclei. A typical fit is shown in Fig. A.2.

The minimum foil thickness (n_{nin}) through which a beam must pass to reach charge state equilibrium is determined by the charge exchange cross sections involved. Since charge exchange reactions contribute significantly to stopping power, n_{nin} is small near the maximum in the stopping power curve. This is the case for the beams considered here. To set a limit on n_{nin}, the final charge-state distribution of an 8.75 MeV 3^{+} ^{10}B beam was measured from 10, 20, 30 and 50 μg/cm^2 C foils. The resulting 5^{+} charge state fraction is shown in Fig. A.3. The data was corrected for the predicted change in

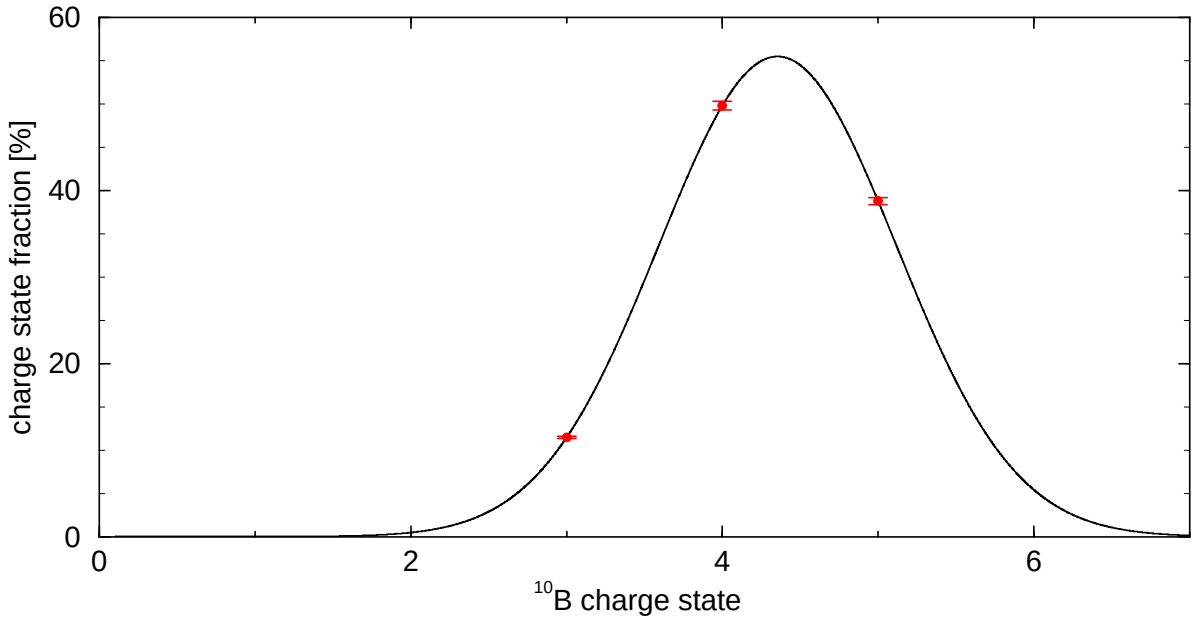

Figure A.2: Gaussian fit to charge-state distribution for a 8.65 MeV ^{10}B beam exiting a C foil. The 2^+ and 1^+ fractions used in this work were extrapolated from these fits (see text).

charge state fraction due to the differing energy loss among the targets. Therefore, the corrected data represents 5^+ the charge state fraction for the beam exiting a 10 μg/cm^2 C foil. Both the raw and corrected data are shown in Fig. A.3. The results imply that the ions are in charge state equilibrium within the 1% error bars as shown.

The equilibrium charge-state distributions were then measured for Be and B using a 20 μg/cm^2 C foil to reset the charge states. The results are shown in Table A.1 and shown for B in Fig. A.4 along with literature data. The average charge, q_o, for for Be and B are also shown in Figs. A.5 and A.6. The data agree well with the trend from data in the neighboring energy region.

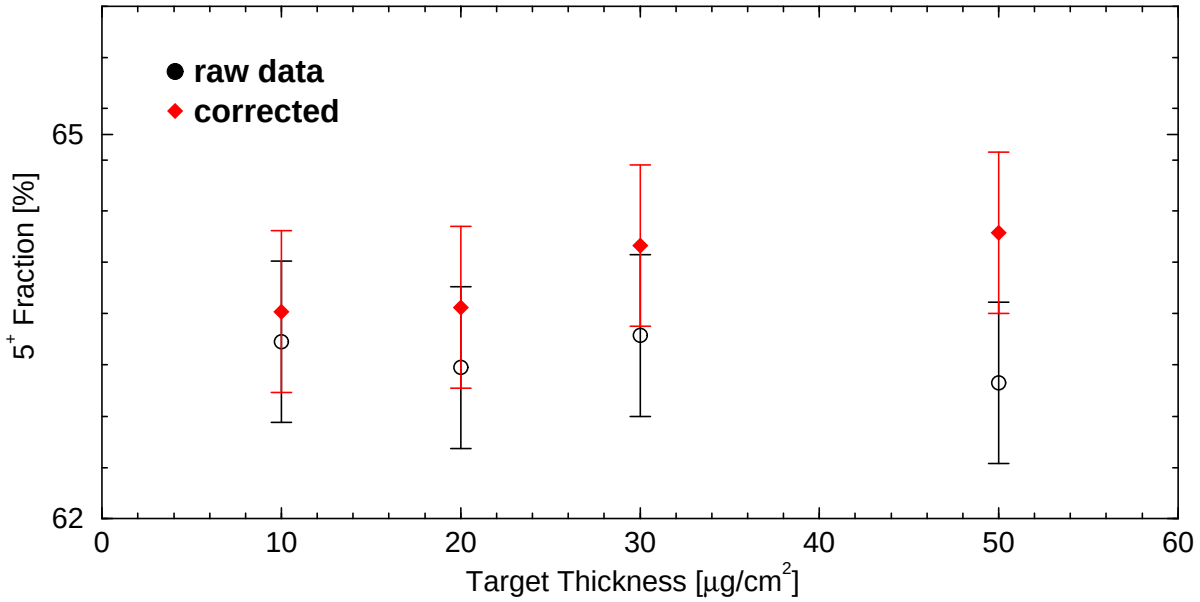

Figure A.3: 5^+ charge state fraction for $E_{beam} = 8.75$ MeV ^{10}Boron ions after passing through C foils of various thickness. 1% error bars represent statistical and estimated systematic uncertainty. Raw and corrected data shown (see text).

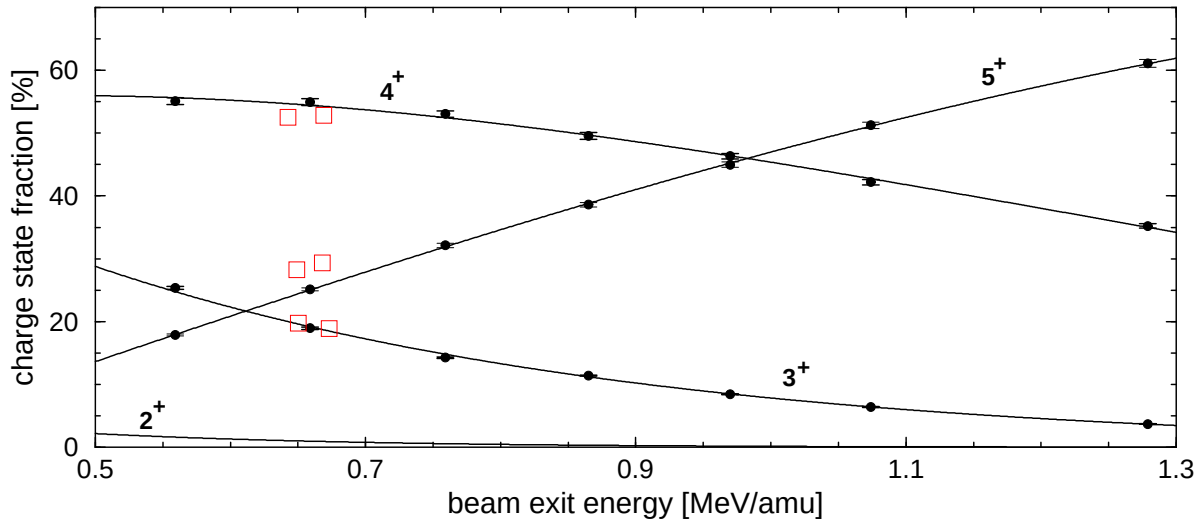

Figure A.4: Boron charge-state distribution. Open squares are data from Ref. [Wol68].

MeV/A \ q	2	3	4	5	q_o
0.557	1.7	25.4	55.1	17.9	3.89
0.657	1.0	18.9	55.0	25.1	4.04
0.758	0.6	14.3	53.0	32.1	4.17
0.864	0.4	11.4	49.6	38.6	4.26
1.666	0.1	3.7	35.2	61.0	4.57

MeV/A \ q	2	3	4	q_o
1.244	0.6	17.0	82.4	3.82
1.252	0.6	17.0	82.4	3.82
1.257	0.5	16.9	82.6	3.82
1.267	0.6	16.6	82.8	3.82
1.277	0.1	9.4	90.4	3.89

Table A.1: Charge state fractions for B and Be beams of various foil exit energies. Values $< 2\%$ are extrapolated from a Gaussian fit (see text). Last column in each table is average charge.

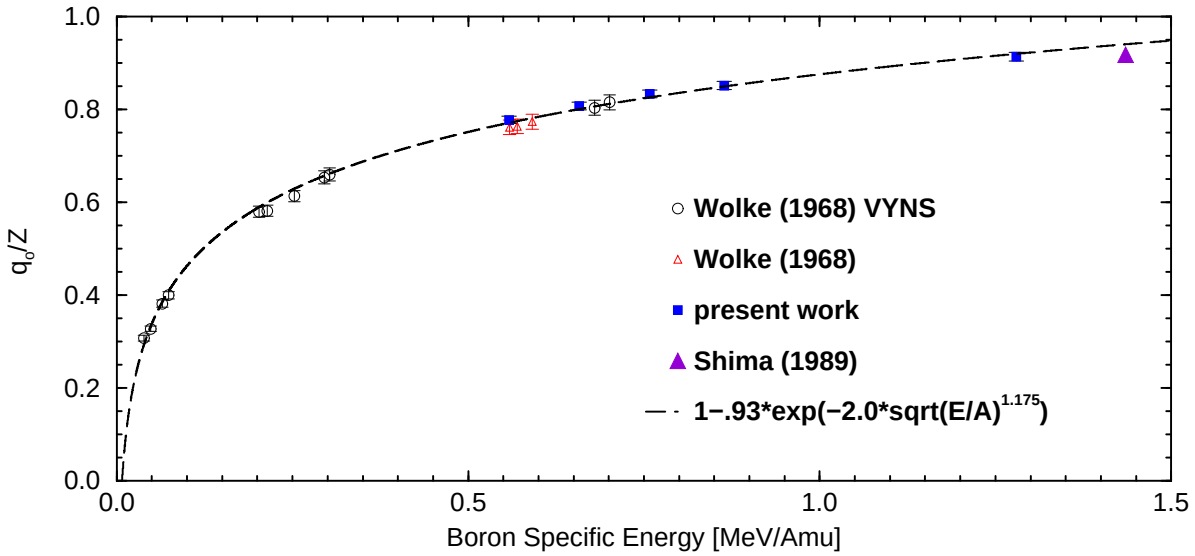

Figure A.5: Average ionization (q_o/Z) of Boron ions after passing through a 20 μg/cm^s C foil. The data fit equation follows the semi-empirical form of Ref. [Say77]. Literature values also shown for Wolke [Wol68] with VYNS and C targets and Shima [Shi89].

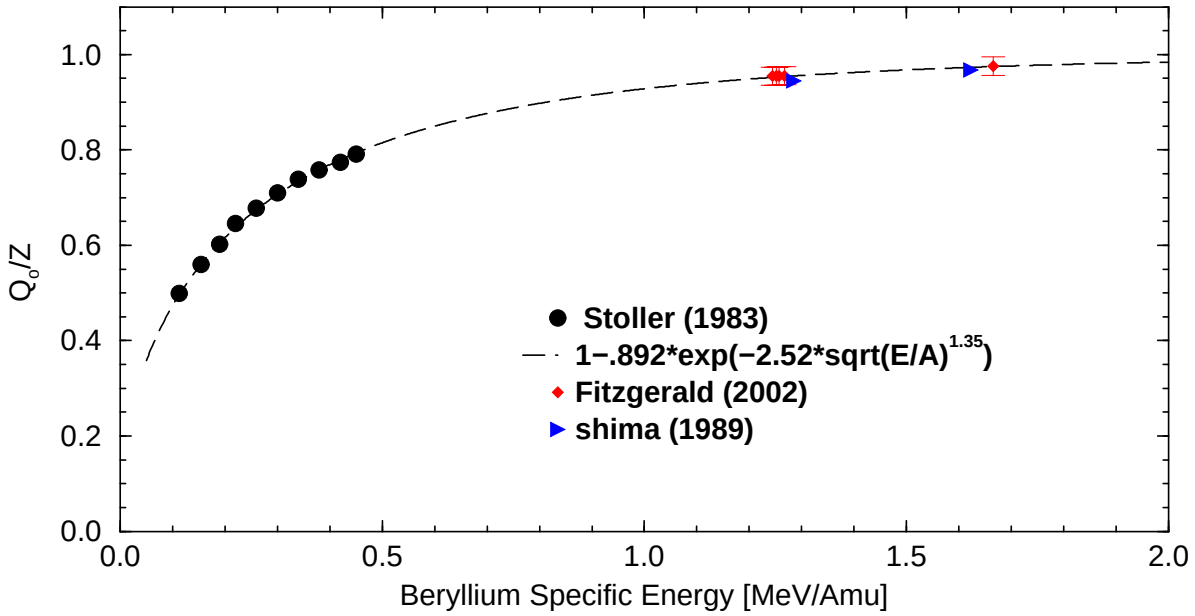

Figure A.6: Average ionization (q_o/Z) of Beryllium ions after passing through a 20 μg/cm^s C foil. Literature values also shown for Stoller [Sto83] and Shima [Shi89].

A.2 gas targets

Non-equilibrium charge-state distributions were measured for Be, B and N beams on the H_2 windowless gas target (WGT). Non-equilibrium data can be used to determine the charge changing cross sections for ions passing through gas. These cross sections are generally poorly constrained, since non-equilibrium data is historically difficult to measure. The cross sections can be used in equilibrium charge state models as well as energy loss models. For reviews of charge-changing cross sections and stopping powers see [All58] and [Bet72] and for experimental considerations, see [Glu53].

The charge-state distributions for a given WGT gas pressure were determined by sending a beam of particles of a given charge state through the WGT and then measuring the count rate of each final charge state at the focal plane of the DRS. An electron suppressed Faraday cup was mounted $\approx 0.5\,\mathrm{m}$. upstream of the focal plane ion counter to count the selected charge state. The various final charge state count rates were normalized, when possible, to elastic scattering in the 45° monitor detectors. At very low pressures however, the monitor count rate was too low to be used, and short data runs were taken and normalized to the integrated Faraday cup current. For each charge state, the Faraday cup readings were re-normalized to particles per second. The data are shown in Fig. A.7, Table A.2, Table A.3, and Table A.4 . The uncertainties are all around 5%, and are due to uncertainties in the relative normalizations.

The boron data was taken at the equivalent velocity of the ^{8}B recoils from the 12.0 MeV ^{7}Be beam. The resulting charge-state distributions from 12.9 MeV $^{10}B^{2+}$ and $^{10}B^{4+}$ beams are listed in Table A.3. The nitrogen charge-state distributions at each pressure were fit with a Gaussian curve as shown in Fig. A.7 and with centroid and width parameters shown in Table A.2. In this way, the charge-state distribution at any pressure can be extrapolated by fitting the trend in these parameters.

n \ q	3	4	5	6	7	q_o	w
0.63	8.0	35.41	49.63	6.77	0.19	4.60	0.71
1.25	0.0	11.74	64.10	22.84	1.32	5.12	0.61
2.51	0.0	0.67	46.00	47.15	6.17	5.52	0.63
3.76	0.0	0.15	28.53	57.93	13.39	5.83	0.68
5.02	0.0	0.09	19.48	58.50	21.94	6.03	0.69
6.27	0.0	0.11	12.36	58.52	29.01	6.19	0.67

n \ q	3	4	5	6	7	q_o	w
1.25	0.05	7.49	62.11	29.54	0.81	5.24	0.70
3.76	0	0.76	27.88	62.75	8.61	5.79	0.72
6.27	0	0.19	9.91	55.67	34.22	6.28	0.90

Table A.2: Non-equilibrium charge-state distributions for 20.1 MeV $^{14}N^{2+}$ (top) and $^{14}N^{3+}$ (bottom) beams on the WGT. n is areal target density in 10^{18} atoms/cm^2, distributions in percent, q_o and w are the centroid and width of Gaussian fits to the distributions.

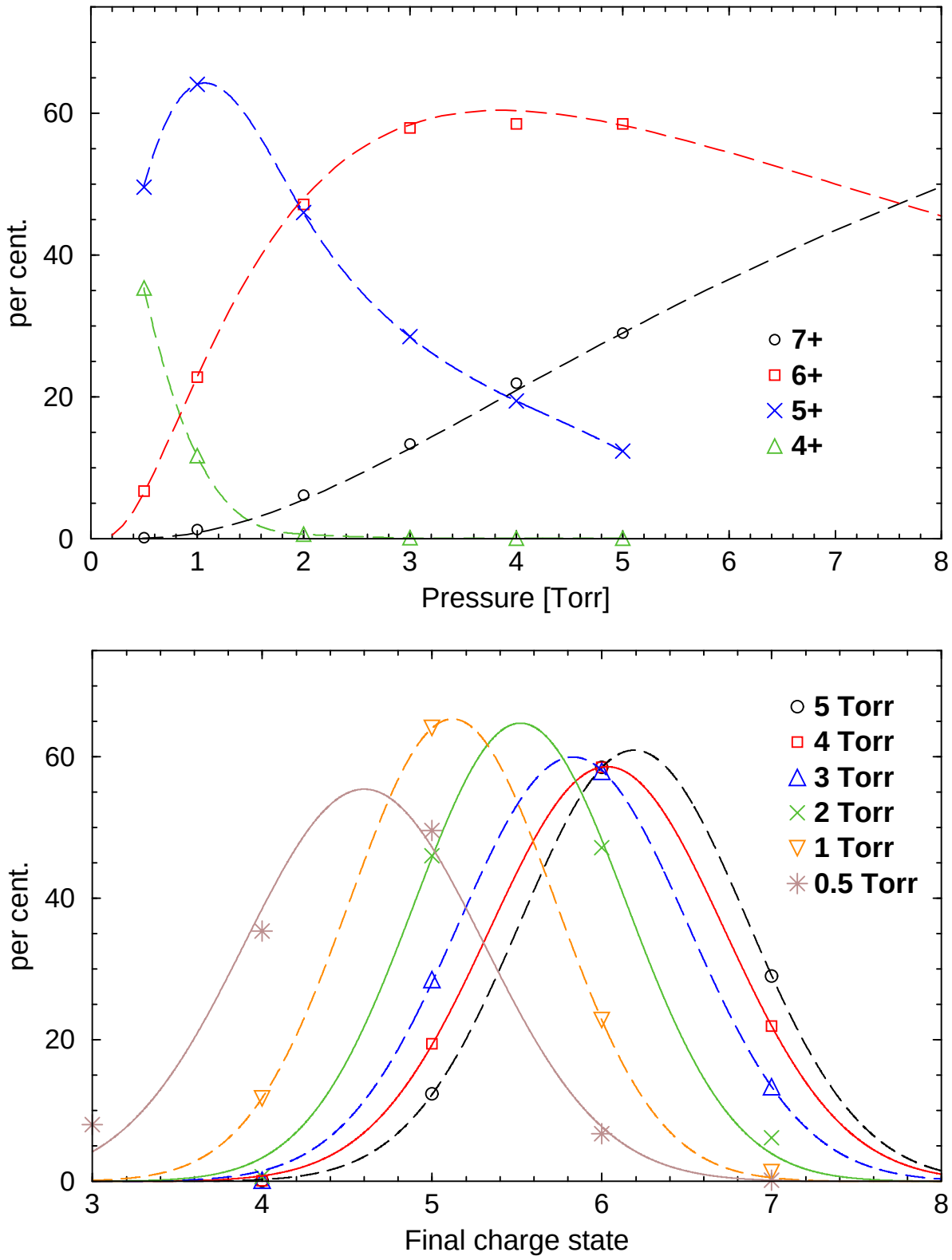

Figure A.7: Non-equilibrium charge-state distributions for 20.1 MeV $^{14}N^{2+}$ initial beam on the WGT. Two views.

n \ q	2	3	4	5
0.31	15.48	61.24	21.81	1.47
0.63	2.27	48.58	43.37	5.77
1.25	0	22.05	58.56	19.39
2.51	0	4.55	47.3	48.15
3.76	0	1.09	31.4	67.51
5.02	0	0	20.08	79.92
6.27	0	0	13.13	86.87
6.9	0	0	10.93	89.07

n \ q	3	4	5
0.31	0.07	8.69	91.24
0.63	0.08	9.74	90.26
1.25	0.1	12.51	87.49
2.51	0.12	13.64	86.24
3.76	0.16	20.61	79.23
5.02	0.26	36.88	62.86
5.64	0.32	59.32	40.3
6.27	0.4	76.94	22.67
6.9	0.53	87.63	11.84

n \ q	4	5
0	3.87	96.13
0.06	3.08	96.92
0.31	1.41	98.59
0.63	1.67	98.33
1.25	2.3	97.7
2.51	3.03	96.97
3.76	3.86	96.14
5.02	4.1	95.9
6.27	4.34	95.66
6.9	4.15	95.85

Table A.3: Non-equilibrium charge-state distributions for 12.9 MeV $^{10}B^{2+}$ (top) and $^{10}B^{4+}$ (bottom left) and $^{10}B^{5+}$ (bottom right) beams on the WGT. n is areal target density in 10^{18} atoms/cm^2 and distributions are in percent.

n \ q	3	4
0.00	1.2	98.8
0.31	0.3	99.7
6.27	0.4	99.6

Table A.4: Non-equilibrium charge-state distributions for 12.0 MeV $^{7}Be^{4+}$ on the WGT. n is areal target density in 10^{18} atoms/cm^2 and distributions are in percent.

Appendix B

Stopping powers of ions in hydrogen gas

During the course of this work various stopping powers (ϵ) of ions in H_2 gas were measured, using the windowless gas target. The system has been calibrated such that the stopping power of any incident ion in H_2 can be measured to 3% accuracy, and is described in Sec. 2.3.4. The stopping powers measured are listed in Table B.1. The energies listed are the beam energies at the center of the target. The stopping powers change by $< 0.5\%$ over the length of the target. Also listed are the corresponding stopping powers calculated using the program MSTAR [Pau02b, Pau02a].

Ion	Energy	ϵ measured	ϵ MSTAR
^{4}He	5.80	3.36	3.32
^{7}Be	12.0	11.6	11.6
^{10}B	12.8	20.0	20.7
^{12}C	20.1	19.1	24.0
^{19}F	7.8	73.0	57.6
^{19}F	16.3	54.5	53.4
^{19}F	23.8	43.0	49.1
^{24}Mg	9.71	93.0	76.9
^{24}Mg	19.4	90.0	78.0
^{24}Mg	41.6	57.0	67.9

Table B.1: Stopping powers of ions in H_2 gas. Energies are beam energies in the center of the target in MeV, stopping powers are in eV·cm^2/10^{15} atoms. Each stopping power has a 3% total uncertainty, due mostly to the 3% uncertainty in the areal target density.

REFERENCES

[Abr84] S. Abramovich, B. Guzhowskij, V. Zherebcov, and A. Zvenigorodskuj, J. YK. **4**, 17 (1984).

[Ahm04] S. N. Ahmed *et al.*, Phys. Rev. Lett. **92**, 181301 (2004).

[All58] S. K. Allison, Rev. Mod. Phys. **30**, 1137 (1958).

[Alt93] G. D. Alton and M. T. Johnson, Nucl. Inst. and Meth. Phys. Res. A **328**, 202 (1993).

[Alt94] G. D. Alton, G. D. Mills, and J. Dellwo, Rev. Sci. Inst. **65**, 2006 (1994).

[Ang99] C. Angulo *et al.*, Nucl. Phys. A **656**, 3 (1999).

[Aud03] G. Audi, H. H. Wapstra, and C. Thibault, Nucl. Phys. A **729**, 337 (2003).

[Azh99a] A. Azhari *et al.*, Phys. Rev. Lett. **82**, 3960 (1999).

[Azh99b] A. Azhari *et al.*, Phys. Rev. C **60**, 055803 (1999).

[Bab03] L. T. Baby *et al.*, Phys. Rev. C **67**, 065805 (2003).

[Bad05] N. R. Badnell *et al.*, arxiv.org:astro-ph/0410744 (2005).

[Bah00] J. Bahcall, J. Roy. Ast. Soc. Can. **94**, 219 (2000).

[Bah01] J. Bahcall, M. Pinsonneault, and S. Basu, Astroph. J. **555**, 990 (2001).

[Bah04] J. Bahcall and M. Pinsonneault, Phys. Rev. Lett. **92**, 121301 (2004).

[Bah05a] J. Bahcall, S. Basu, M. H. Pinsaonneault, and A. M. Serenelli, Astroph. J. **618**, 1049 (2005).

[Bah05b] J. Bahcall, A. M. Serenelli, and S. Basu, Astroph. J. **621**, L85 (2005).

[Bar80] F. C. Barker, Aust. J. Phys. **33**, 177 (1980).

[Bar95] F. C. Barker, Nuc. Phys. A **588**, 693 (19895).

[Bet39] H. Bethe, Phys. Rev. **55**, 436 (1939).

[Bet72] H. D. Betz, Rev. Mod. Phys. **44**, 465 (1972).

[Bie95] J. Biersack and J. Ziegler, 1995, Transport of Ions in Matter, TRIM program Version 95.06, SRIM2003 http://www.srim.org.

[Bil83] B. W. Bilippone, A. J. Elwyn, C. N. Davids, and D. D. Koetke, Phys. Rev. C **28**, 2222 (1983).

[Bla04] J. Blackmon, 2004, private communication.

[Cyb04] R. H. Cyburt, B. Davids, and B. K. Jennings, Phys. Rev. C **70**, 045801 (2004).

[D'A04] J. M. D'Auria *et al.*, Phys. Rev. C **69**, 065803 (2004).

[Dav68] R. Davis, D. Harmer, and K. Hoffman, Phys. Rev. Lett. **20**, 1205 (1968).

[Dav01] B. Davids *et al.*, Phys. Rev. Lett. **86**, 2750 (2001).

[Dav02] B. Davids *et al.*, Eur. Phys. J. A **15**, 65 (2002).

[Dav03] B. Davids and S. Typel, Phys. Rev. C **68**, 045802 (2003).

[Des88] P. Descouvemont and D. Baye, Nuc. Phys. A **487**, 420 (1988).

[Des93] P. Descouvemont and D. Baye, Nuc. Phys. A **567**, 341 (1993).

[Dom04] C. P. Domizioli, 2004, private communication.

[Edd20] A. S. Eddington, Nature **106**, 14 (1920).

[End90] P. M. Endt, Nucl. Phys. A **521**, 1 (1990).

[Eng03] S. Engel, *Ph.D. Thesis*, Ruhr-Universität Bochum, 2003.

[Fab95] T. E. Faber, *Fluid Dnynamics for Physicists*, Cambridge University Press, 1995.

[Fai60] A. Fairhall, *The Radiochemistry of Beryllium*, The U.S. Atomic Energy Comission Office of Technical Information Report, Oak Ridge, TN, 1960.

[Fit05] R. Fitzgerald *et al.*, Nucl. Phys. A **748**, 351 (2005).

[Gia02] L. Gialanella *et al.*, Nucl. Inst. Meth. Phys. Res. B **197**, 150 (2002).

[Glu53] R. L. Gluckstern, Phys. Rev. **98**, 1817 (1953).

[Gor67] S. Gorodetzky *et al.*, Nucl. Phys. A **91**, 133 (1967).

[Gör80] J. Görres, K. Kettner, H. Kräwinkel, and C. Rolfs, Nucl. Inst. Meth. Phys. Res. **177**, 295 (1980).

[Gre05] U. Greife, 2005, private communication.

[Ham98] F. Hammache *et al.*, Phys. Rev. Lett. **80**, 928 (1998).

[Ham01] F. Hammache *et al.*, Phys. Rev. Lett. **86**, 3985 (2001).

[Han78] C. Hanke and J. Laursen, Nucl. Inst. Meth. Phys. Res. **151**, 253 (1978).

[Has99] M. Hass *et al.*, Phys. Lett. B **462**, 237 (1999).

[Hax00] W. C. Haxton and B. R. Holstein, Am. J. Phys. **68**, 15 (2000).

[Hin92] S. Hinds and F. C. Barker, Aust. J. Phys. **45**, 749 (1992).

[Iwa99] N. Iwasa *et al.*, Phys. Rev. Lett. **83**, 2910 (1999).

[Jam88] A. N. James *et al.*, Nucl. Inst. and Meth. Phys. Res. A **267**, 144 (1988).

[Jen98] B. K. Jennings, S. Karataglidis, and T. D. Shoppa, Phys. Rev. C **58**, 3711 (1998).

[Jun03] A. Junghans *et al.*, Phys. Rev. C **68**, 065803 (2003).

[Kav60] R. Kavanagh, Nucl. Phys. **15**, 411 (1960).

[Kav69] R. W. Kavanagh, T. A. Tombrello, J. M. Mosher, and D. R. Goosman, Bull. Am. Phys. Soc. **14**, 1209 (1969).

[Kik98] T. Kikuchi *et al.*, Eur. Phys. J. A **213**, 1998 (1998).

[Kis89] A. Z. Kiss, E. Koltay, and E. Somorji, Acta Phys. Hung. **65**, 277 (1989).

[Lid90] D. R. Lide, *Handbook of Chemistry and Physics*, CRC press, Cleveland, 1990.

[Lis75] H. Liskienk and A. Paulsen, Atom. Data Nucl. Data **15**, 57 (1975).

[Mal03] M. Maltoni, T. Schwetz, A. Tórtola, and J. Valle, Phys. Rev. D **68**, 113010 (2003).

[Mar62] F. W. Martin and L. C. Northcliffe, Phys. Rev. **128**, 1166 (1962).

[Oga03] K. Ogata, M. Yahiro, Y. Iseri, and M. Kamirura, Phys. Rev. C **67**, 011602 (2003).

[Pal66] R. Palmer, Proc. Phys. Soc. **87**, 681 (1966).

[Par66] P. Parker, Phys. Rev. **150**, 851 (1966).

[Pau02a] H. Paul and A. Schinner, Nucl. Inst. Meth. Phys. Res. B **195**, 166 (2002).

[Pau02b] H. Paul and A. Schinner, "MSTAR", 2002.

[Rei90] G. Reiter, N. Kniest, E. Pfaff, and G. Causnitzer, Nucl. Inst. Meth. Phys. Res. B **44**, 399 (1990).

[Roh94] J. W. Rohlf, John Wiley & Sons, Inc., 1994.

[Rol88] C. Rolfs and W. S. Rodney, *Couldrons in the Cosmos*, Univ. of Chicago Press, 1988.

[Say77] R. O. Sayer, Rev. D. Phys. App. **12**, 1543 (1977).

[Sch03] F. Schümann *et al.*, Phys. Rev. Lett. **90**, 232501 (2003).

[Sea51] J. D. Seagrave, Phys. Rev. **84**, 1219 (1951).

[Sha00] D. Shapira, T. A. Lewis, and L. D. Hulett, Nucl. Inst. Meth. Phys. Res. A **454**, 409 (2000).

[Shi89] K. Shima, N. Kuno, and M. Yamanouchi, Phys. Rev. A **40**, 3557 (1989).

[Sno04] K. A. Snover, A. R. Junghans, and E. C. Mohrmann, Phys. Rev. C **70**, 039801 (2004).

[Sob01] H. Sobel, P. Lurie, D. Ortlieb, and S. Wolfe, *Letter to John Henshaw, Assistant Secretary of Labor for Occupational Safety and Health*, Health Research Publication, HRG no. 1589, 2001.

[Spi96] M. Spiegel, *Schaum's Outlines: Mathematical Handbook*, McGraw-Hill, 1996.

[Spy97] K. Spyrou, C. Chronidou, S. Harissopulos, S. Kossionides, and T. Paradellis, Z. Phys. A **357**, 283 (1997).

[Sto83] C. Stoller *et al.*, IEEE Trans. Nucl. Sci. **30**, 1074 (1983).

[Str96] F. Strieder *et al.*, Z. Phys. A **355**, 209 (1996).

[Str01] F. Strieder *et al.*, Nucl. Phys. A **696**, 219 (2001).

[Ter01] F. Terrasi *et al.*, Nucl. Phys. A **688**, 539c (2001).

[Til02] D. Tilley, C. Cheves, J. Godwin, G. Hale, H. Hoffmann, J. Kelley, C. Sheu, and H. Weller, Nucl. Phys. A **708**, 3 (2002).

[Tom65] T. A. Tombrello, Nuc. Phys. **71**, 459 (1965).

[Tra75] H. P. Trautvetter, Nucl. Phys. A **243**, 37 (1975).

[Tra03] L. Trache *et al.*, Phys. Rev. C **67**, 062801 (2003).

[Tul95] J. Tuli, *Nuclear Wallet Cards*, Brookhaven National Laboratory, Upton, New York, 1995.

[Vau70] F. J. Vaughn, R. A. Chalmers, D. Kohler, and L. F. C. Jr., Phys. Rev. C **2**, 1657 (1970).

[Wan99] Y. B. Wang *et al.*, Chin. Phys. Lett. **16**, 873 (1999).

[Wie77] C. Wiezorek, H. Krawinkel, R. Santo, and L. Wallek, Z. Phys. A **282**, 1977 (1977).

[Wil81] R. D. Williams and S. E. Koonin, Phys. Rev. C **6**, 23 (1981).

[Wol68] R. L. Wolke, Phys. Rev. **171**, 301 (1968).